

AD 658 167

ALL INFORMATION CONTAINED
HEREIN IS UNCLASSIFIED
DATE 08-11-2010 BY 60322
UCBAW/STP

100-443888-100
100-443888-100
100-443888-100
100-443888-100

ALL INFORMATION CONTAINED
HEREIN IS UNCLASSIFIED
DATE 08-11-2010 BY 60322
UCBAW/STP

ALL INFORMATION CONTAINED
HEREIN IS UNCLASSIFIED
DATE 08-11-2010 BY 60322
UCBAW/STP

TECHNICAL REPORT

**BRILLOUIN SCATTERING EXPERIMENTS IN THE FERROELECTRIC
CRYSTAL TRIGLYCINE SULFATE**

Robert W. Gammon and Herman Z. Cummins

**Department of Physics
The Johns Hopkins University
Baltimore, Maryland 21218**

Sponsored by

**Advanced Research Project Agency
Project DEFENDER
ARPA Order No. 675**

AROD Contract No. DA-31-124-ARO-D-400

**BEST
AVAILABLE COPY**

ABSTRACT

Brillouin scattering measurements have been made on triglycine sulfate near its Curie temperature. Temperature and field dependent single relaxation time acoustic velocity dispersion was found in confirmation of the predictions of a simple free energy expansion theory of the dynamics of the strain and polarization fluctuations near T_C . This theory is developed in detail following O'Brian and Litovitz who first combined the Devonshire theory of ferroelectrics with the Landau-Khalatnikov theory of the relaxation of the order parameter to treat sound absorption near T_C in triglycine sulfate. This new treatment of the theory was able to account for the anisotropy in the coupling of the strain and polarization fluctuations, the field dependent relaxation rate observed, and the anisotropy in the relaxation rate for directions between the ferroelectric axis and the plane perpendicular to it. We found our observations fit by $\tau (\Delta T, E = 0)^{-1} = (3.4 \pm 10\%) \times 10^{10} (T_C - T) \text{ sec}^{-1}$ and

$\tau (\Delta T = 0, E)^{-1} = (2.0 \pm 10\%) \times 10^{10} E^{2/3} \text{ sec}^{-1}$ with ΔT in $^\circ\text{C}$ and E in kV/cm . From $\tau (\Delta T, E = 0)$ we find the kinetic coefficient for the polarization fluctuations to be $\gamma = (4.1 \pm 10\%) \times 10^{12} \text{ sec}^{-1}$.

Additional experimental results obtained for triglycine sulfate include measurement of the acoustic mode velocities for all three modes for various directions in the (010) plane, measurement of the longitudinal velocity along the ferroelectric axis, a measurement of a reference absolute cross section for Brillouin scattering in triglycine sulfate, and determination of some of the Pockels coefficients from the Brillouin component intensity in various directions.

TABLE OF CONTENTS

<u>INTRODUCTION</u>	<u>PAGE</u>
<u>SECTION</u>	<u>1</u>
I. INTRODUCTION TO LIGHT SCATTERED FROM ACOUSTIC MODES OF CONDENSED MEDIA- BRILLOUIN SCATTERING - - - - -	5
II. THE THEORY OF BRILLOUIN SCATTERING IN CRYSTALS - - - - -	18
III. THE APPARATUS USED TO OBSERVE BRILLOUIN SCATTERING - - - - -	39
IV. EXPERIMENTAL BRILLOUIN SCATTERING IN THE MONOCLINIC CRYSTAL TGS - - - - -	56
V. EXPERIMENTAL BRILLOUIN SCATTERING IN TGS NEAR ITS FERROELECTRIC PHASE TRANSITION- -	100
VI. A THERMODYNAMIC POTENTIAL THEORY FOR THE STRAIN AND POLARIZATION FLUCTUATION DYNAMICS IN TGS NEAR ITS FERROELECTRIC PHASE TRANSITION - - - - -	132
APPENDIX - - - - -	166
FOOTNOTES- - - - -	172

LIST OF TABLES

	<u>PAGE</u>
I 1 Correlation functions	14
II 1 (010) plane acoustic mode velocities in TGS calculated from ultrasonic elastic constants.	27
IV 1 Scattering vectors (010) plane in TGS	59
IV 2 (010) plane observed velocities.	83
IV 3 HV, VH scattering amplitudes.	92
IV 4 Brillouin scattering cross sections.	95
IV 5 TGS Pockels coefficients.	98
V 1 TGS Curie temperature.	106
V 2 Relaxation times in TGS	113
V 3 Summary of parameters for temperature dispersion fit of $(\Delta\nu)^2$ to single relaxation formula.	117
V 4 (010) plane velocity temperature coefficients.	123

LIST OF FIGURESPAGE

I 1	Schematic picture of a light scattering experiment.	7
I 2	Geometry of the wavevectors in quasi-elastic scattering.	10
III 1	Brillouin scattering apparatus .	40
IV 1	Typical Brillouin scattering spectrum in TGS.	61
IV 1	Superimposed traces of Brillouin scattering spectra for scattering angles of 90° and 135° .	64
IV 3	Polarized Brillouin spectra in TGS.	67
IV 4	L and T1 mode Brillouin component intensities.	70
IV 5	Ratio of Brillouin component intensities for the L and T1 modes.	72
IV 6	L mode velocities in the (010) plane of TGS.	74
IV 7	T1 mode velocities in the (010) plane of TGS.	76
IV 8	L mode velocities: observed and calculated.	78
IV 9	T1 mode velocities: observed and calculated.	80
IV 10	T2 mode velocities: observed and calculated.	85
V 1	L and T1 mode Brillouin shift dispersion with temperature.	110
V 2	ΔT versus mode frequency.	112
V 3	Normalized change in v^2 versus temperature.	115
V 4	Brillouin component linewidths versus temperature.	118

<u>LIST OF FIGURES, Cont'd.</u>		<u>PAGE</u>
V 5	Superimposed T1 Brillouin component traces showing broadening.	119
V 6	Normalized change in v^2 versus $\log E^{2/3}$ for the T1 mode.	126
V 7	Total temperature dispersion versus $\theta(q)$.	128
V 8	VV spectrum showing Rayleigh, T1, and L component peaks at T_C .	131
VI 1	Calculated coupling anisotropy in the (010) plane.	155
A 1	TGS lattice directions and coordinate systems.	167

INTRODUCTION

This thesis is a report of a set of light scattering experiments on a ferroelectric crystal in the region of its ferroelectric phase transition. The aim of the experiments was to study the dynamics of a second-order phase transition in a crystal by means of the spectrum of light scattered from it near the phase transition temperature.

The crystal chosen for study was triglycine sulfate. It turned out to be a rather classic case. The effects observed were weak and therefore were easily separated for interpretation. There were no interfering anomalies in optical dielectric properties near the transition temperature. All the observations could be understood on the simple basis of expanding the free energy about equilibrium values of the thermodynamic variables.

The most important sections of this thesis are Sections V and VI. They contain the new observation and interpretations which are believed to be important to the subject of phase transitions.

The experimental data is presented in Section V. Our measurements show that two of the acoustic modes in the plane perpendicular to the ferroelectric axis are coupled to damped fluctuations and therefore show velocity dispersion with a temperature dependent relaxation time. In addition to observing this velocity dispersion from which we obtained the relaxation rate we were able to observe the associated

acoustic absorption by measuring the Brillouin component linewidth as a function of temperature. Such measurements have not been made in crystals using light scattering prior to this. For the same modes that showed velocity dispersion and absorption we found the new effect of a field dependent dispersion and absorption with a single relaxation time. From the velocity dispersion we determined the field dependent relaxation rate. Also for these modes we studied the anisotropy of the velocity dispersion in the plane perpendicular to the ferroelectric axis. We found that the total dispersion was highly anisotropic but that the relaxation rate was the same for all directions in the plane. We studied the third acoustic mode and found it not to show relaxational dispersion with temperature or field.

In Section VI we present the phenomenological theory which accounts very well for our observations. It was previously known that the Devonshire free energy expansion theory gave a good description of the static properties of triglycine sulfate. The present work shows that together with the kinetic assumption of irreversible thermodynamics the same free energy expansion accounts for the dynamics of the strain and polarization fluctuations. Following the lead of O'Brian and Litovitz we have gone on to derive in detail the consequences of the Landau-Khalatnikov theory of relaxation rates for second-order transitions. In addition to the previously derived

velocity dispersion with a relaxation time proportional to $(T_C - T)^{-1}$ our analysis shows how to calculate the coupling anisotropy, that the pure shear mode in the plane perpendicular to the ferroelectric axis should not be coupled to the relaxing fluctuations, and that an electric field applied along the ferroelectric axis with the crystal at T_C produces a velocity dispersion with a relaxation time proportional to $E^{-2/3}$. All of these results are confirmed by our experiments. In addition we derived the anisotropy in the relaxation rate of polarization fluctuations for directions out of the plane perpendicular to the ferroelectric axis by taking account of the electrostatic energy associated with the polarization fluctuations. This accounted for the observation that the longitudinal mode along the ferroelectric axis showed no temperature dependent relaxational dispersion even though these strains are known to be coupled to the polarization. Additional consequences of this last derivation remain to be tested.

The first four sections form an exposition of the method of Brillouin scattering applied to the study of the acoustic modes in crystalline solids. It is these techniques which allowed the rather complete study of the fluctuations in triglycine sulfate near T_C . The purpose of Section I is to present the simplest and most universal case of Brillouin scattering, namely scattering from density waves. This scattering is common to all condensed phases

and usually gives the most intense components in the Brillouin spectrum. In this section we indicate how the approximate scattering cross section for scattering from longitudinal modes in crystalline solids can be computed from the refractive index and the elastic properties of the material. In Section II we discuss Brillouin scattering in crystals. Using the classical theory of elasticity to derive the strain fluctuation dynamics and the Pockels elasto-optic coefficients to relate the dielectric fluctuation tensor and the strain fluctuations we derive scattering selection rules and cross sections for Brillouin scattering with polarized light in birefringent crystals. Specific application of these hitherto untested selection rules and intensity predictions is made for triglycine sulfate in the Brillouin scattering observations presented in Section IV. In that section we show that Brillouin scattering with polarized incident and scattered light can be used to sort out and study all three acoustic modes in the plane perpendicular to the monoclinic axis. From these spectra we were able to determine the acoustic velocities and some of the Pockels coefficients.

In Section III we describe the apparatus for observing Brillouin scattering in crystals with particular emphasis on our high contrast Fabry-Perot interferometer and the photon counting detection system.

SECTION I

INTRODUCTION TO LIGHT SCATTERING FROM ACOUSTIC MODES
OF CONDENSED MEDIA -- BRILLOUIN SCATTERING

All forms of matter scatter light but this scattering is usually masked by the much stronger first order processes of absorption and emission. Scattering is the basic electromagnetic interaction for frequencies to which a medium is transparent. It manifests itself in two ways. The forward scattering which is coherent with the incident light gives the medium its refractive index. The scattering in directions other than the forward directions is in general inelastic and can be detected directly. This non-forward scattering is the phenomenon which we will be concerned with and will refer to simply as light scattering.

We will be interested in those low energy states of condensed media (collective modes) which are coupled to the optical polarizability of the medium. They will scatter light either when driven externally, as in the Debye-Sears effect,⁽¹⁾ or when thermally populated. By examining the spectrum of the scattered light we study the dynamics of the fluctuations in polarizability and hence the dynamics of the collective modes.

Acoustic modes are collective modes found in all condensed media. They correspond to the modes of sound propagation when driven externally and to the low energy states of the medium in equilibrium which are used in the Debeye model of the specific heat. These modes usually are effective in scattering light and so give rise to the basic features of the low frequency portion of light scattering spectra. The process of scattering light from acoustic modes is called Brillouin scattering after L Brillouin who predicted in a fundamental paper in 1922⁽²⁾ that light should be inelastically scattered by the Debye modes of a transparent medium.

First we define the problem operationally in terms of a light scattering experiment. We will not be perfectly general in this but rather choose arrangements which are useful in experiments. The basic arrangement is shown in Fig. 11. A narrow beam of monochromatic light with wave vector \vec{k}_0 and frequency ω_0 is passed through material of dielectric constant ϵ_0 . The volume of the material illuminated by the beam becomes visible due to scattering. We arrange to collect light from a definite length L of the beam in a small solid angle about a direction at an angle θ to the incident beam. θ is called the scattering angle. We describe the scattering direction by the wave vector of the scattered light, \vec{k}_s . The scattering volume is L times the cross-sectional area of the incident beam.

The scattering plane is the plane containing \vec{k}_0 and \vec{k}_s . It is most useful in experiments to have the polarization of the incident light either perpendicular or parallel to the scattering plane. We will denote this choice by V or H, respectively. Similarly, we analyze the scattered light into "vertically" and "horizontally" polarized components. Denoting the incident polarization first and the scattered polarization second we can have the following four possible scattered intensity measurements: VV, VH, HV, or HH.

The scattered light which we have selected is now detected to give the total scattering intensity or is spectrally analyzed and then detected to give spectral intensities. Comparison of the scattered power with the incident power, taking account of the collection geometry, gives cross sections for the various processes giving rise to components of the scattering spectrum.

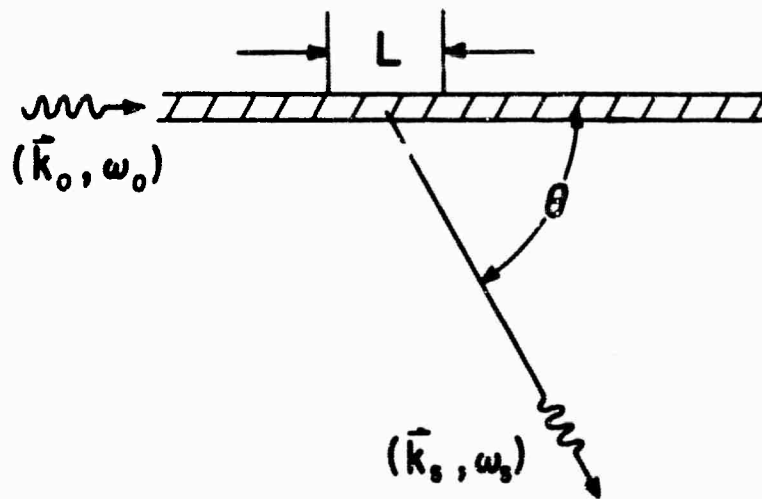


Fig. 11 Schematic picture of a light scattering experiment.

Though light scattering is a universal effect it is not normally a strong effect. Typically 10^{-6} to 10^{-8} of the light incident on a sample is scattered (per cm of the sample) by acoustic modes. Thus the light scattered from a beam of light in a material does not make a very bright source for spectroscopic study. Here lies much of the experimental challenge in light scattering.

With the invention of the laser and in particular the perfection of continuous gas lasers we now have an ideal tool for high resolution light scattering experiments with high resolution in frequency, scattering angle, and polarization.

In order to understand light scattering processes in enough detail to allow predictions of effects and interpretation of experimental results we will review the results of theoretical calculations of the scattering intensity.

Many derivations of the scattering intensity or scattering cross section for Brillouin scattering in isotropic media exist in the literature.⁽²⁻⁹⁾ In particular the modern treatments by Pecora⁽⁸⁾ and Landau and Lifshitz⁽⁹⁾ are recommended. The basic ideas and perturbation technique remain those of Einstein and Brillouin. Rather than repeat the derivation we will give the result in a form useful for experimental work and with which one may guess the result for new situations.

In an isotropic medium with average optical dielectric constant ϵ_0 , the cross section for scattering V (perpendicular to the scattering plane) polarized incident light of frequency ω_0 into V polarized scattered light with wave vector \vec{k}_s at an angle θ to \vec{k}_0 is .

$$\frac{d\sigma_{VV}}{d\Omega} = \left(\frac{1}{4\pi}\right)^2 \left(\frac{\omega_0}{C}\right)^4 \langle |\Delta\epsilon(\vec{q}, t)|^2 \rangle V^2$$

where

$$\Delta\epsilon(\vec{r}, t) = \epsilon(\vec{r}, t) - \epsilon_0$$

$$\Delta\epsilon(\vec{q}, t) = \frac{1}{V} \int_V \Delta\epsilon(\vec{r}, t) e^{-i\vec{q} \cdot \vec{r}} d^3r$$

$$\vec{q} = \vec{k}_0 - \vec{k}_s$$

V = scattering volume

ω_0 = incident light frequency

c = velocity of light in a vacuum .

This expression is appropriate for scattering in simple liquids where density fluctuations give scalar fluctuations in the dielectric properties. For these fluctuations the scattered light is all V polarized. We note that the light scattered at an angle θ is scattered by a definite spacial Fourier component of the dielectric fluctuation. Since the frequency shifts $(\omega_0 - \omega_s)$ involved in the scattering are small, we may take the magnitudes of the incident and scattered wave vectors equal giving

$$q = |\vec{q}| = 2k_0 \sin(\theta/2)$$

and \vec{q} parallel to the bisector of the angle between \vec{k}_0 and \vec{k}_s . This geometry is shown in Fig. 1 2. The scattering is proportional to

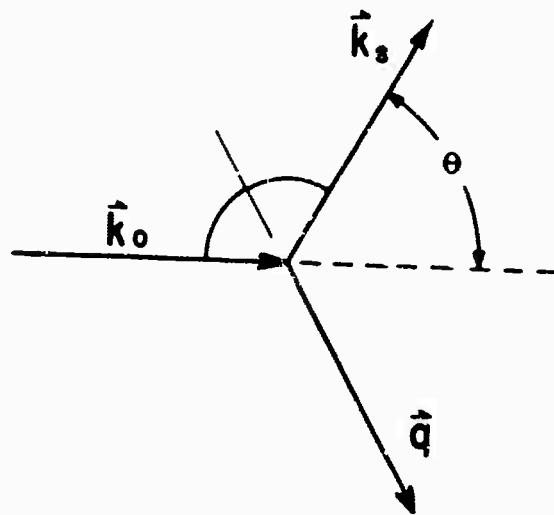


Fig. 1 2 Geometry of the wavevectors in quasi-elastic scattering. k_0 is the incident light wavevector, k_s is the scattered light wave vector and q is the scattering wavevector.

the volume illuminated and proportional to the reciprocal fourth power of the vacuum light wavelength as is characteristic of quasi-elastic scattering from small scattering elements. The $\langle \rangle$ brackets indicate a time average or equivalently an ensemble average. This average is itself independent of time and can easily be computed using the methods of thermodynamic fluctuation theory if we know which variable is fluctuating and the dependence of the dielectric constant on this variable. For simple liquids we have the standard results⁽¹⁰⁾

$$\rho \left(\frac{\partial \epsilon}{\partial \rho} \right)_T = (\epsilon - 1)$$

$$\text{and} \quad \frac{\langle |\rho(q)|^2 \rangle}{\rho^2} = \frac{kT\beta}{V} \quad 1.8 (a)$$

where β_T is the isothermal compressibility. It is an empirical fact that essentially all of the scattering is due to density fluctuations at constant temperature. Hence to a good approximation

$$\frac{d\sigma_{VV}}{d\Omega} = \left(\frac{1}{4\pi} \right)^2 \left(\frac{\omega_0}{C} \right)^4 (\epsilon - 1)^2 kT\beta_T V .$$

We note that this cross section is proportional to the scattering volume V as expected. This is the standard result for scattering from density fluctuations in isotropic media.

So far we have given expressions for the total scattering. The spectral distribution is what we would really like to know about.

The spectrum of the scattered light can be most rigorously defined using the Fourier transform of the autocorrelation of the scattered electric field. This implies that the spectral intensity at the frequency ω_s is proportional to the Fourier transform of the autocorrelation function of $\Delta\epsilon(\mathbf{q}, t)$ evaluated at $\omega = (\omega_o - \omega_s)$. Explicitly the spectral cross section is

$$\left(\frac{d\sigma_{VV}(\omega_s)}{d\Omega} \right)_{\substack{\vec{k}_o \rightarrow \vec{k}_s \\ \omega_o \rightarrow \omega_s}} = \left(\frac{1}{4\pi} \right)^2 \left(\frac{\omega_o}{C} \right)^4 \langle |\Delta\epsilon(\vec{q})|_{\omega}^2 \rangle V^2$$

with $\vec{q} = \vec{k}_o - \vec{k}_s$ and $\omega = \omega_o - \omega_s$

where we define

$$\langle |\Delta\epsilon(\vec{q})|_{\omega}^2 \rangle \triangleq \frac{1}{2\pi} \int_{-\infty}^{\infty} dt' e^{i\omega t'} \langle \Delta\epsilon(\vec{q}, t' + t) \Delta\epsilon^*(\vec{q}, t) \rangle$$

The correlation function and its Fourier transform are assumed independent of time t since thermal fluctuations are random stationary process.

Suppose the correlation function has a time dependence $\cos(\omega(q)t)$ (This would correspond to a modulation of ϵ by some kind of propagating collective mode). Then we find that the spectrum consists of delta functions at

$$\omega = \pm \omega(q) .$$

More realistically the amplitude of the collective modes will have a finite lifetime $\tau = \frac{1}{\Gamma}$. We then get a pair of Lorentzians

$$\langle |\Delta\epsilon(\vec{q})|_{\omega}^2 \rangle = \langle |\Delta\epsilon(\vec{q}, t)|^2 \rangle \sum_{+} \frac{1}{2\pi} \frac{\Gamma}{(\omega \pm \omega(\vec{q}))^2 + \Gamma^2}$$

whose full width at half maximum is 2Γ . (\sum_{+} denotes sum over + and - terms). Thus the spectral intensity will be centered at the frequencies

$$\omega_s = \omega_o \pm \omega(\vec{q})$$

We summarize these relations for three common correlation functions in Table I 1.

These results have a very simple interpretation. The scattering spectra are Fourier transforms of the time dependence of the properties of the "phase grating" (the q th spatial component of $\Delta\epsilon(\vec{r}, t)$) which is "diffracting" a portion of the incident beam. If the amplitude of this grating decays then the scattered beam acquires a correspondingly shorter lifetime i. e. , it is broadened. If the grating is moving with

TABLE I
CORRELATION FUNCTIONS

$$\langle |\Delta \epsilon(\vec{q})|_{\omega}^2 \rangle = \frac{1}{2\pi} \int_{-\infty}^{\infty} dt' e^{i\omega t'} \langle \Delta \epsilon(\vec{q}, t' + t) \Delta \epsilon^*(\vec{q}, t) \rangle$$

TYPE OF FLUCTUATION	$\frac{\langle \Delta \epsilon(\vec{q}, t' + t) \Delta \epsilon^*(\vec{q}, t) \rangle}{\langle \Delta \epsilon(\vec{q}, t) ^2 \rangle}$	$\frac{\langle \Delta \epsilon(\vec{q}) _{\omega}^2 \rangle}{\langle \Delta \epsilon(\vec{q}, t) ^2 \rangle}$
PROPAGATING	$\cos \omega(\vec{q})t'$	$\frac{1}{2} \left[\delta(\omega + \omega(\vec{q})) + \delta(\omega - \omega(\vec{q})) \right]$
DAMPED PROPAGATING	$e^{-\Gamma(\vec{q})t'} \cos \omega(\vec{q})t'$	$\frac{1}{2\pi} \sum_{\vec{k}} \frac{\Gamma(\vec{q})}{(\omega \pm \omega(\vec{q}))^2 + \Gamma(\vec{q})^2}$
NON - PROPAGATING DECAYING	$e^{-\Gamma(\vec{q})t'}$	$\frac{\Gamma(\vec{q})}{(\omega^2 + \Gamma(\vec{q})^2)}$

velocity $v(\vec{q})$ either parallel or anti parallel to \vec{q} then the scattered light is frequency shifted by the Doppler effect either down or up by $\omega(\vec{q}) = qv(\vec{q})$ radians/sec., respectively.

With these results let us now consider Brillouin scattering in simple liquids and isotropic solids. In particular we consider scattering from density waves in these media. (These density waves can also be called compressional waves or longitudinal acoustic modes of the material. They are common to all condensed media.) For the wavelengths of interest these waves are best described as adiabatic density waves in liquids. We then have from the theory of thermodynamic fluctuations of Fourier components of inhomogeneous fluctuations⁽¹¹⁾

$$\langle |\Delta \rho(q)_s|^2 \rangle = \frac{\rho^2 kT \beta_s(q)}{V}$$

$$\text{where } \beta_s(q) = -\frac{1}{\rho} \frac{\partial \Delta \rho(q)}{\partial p(q)_s} = \frac{1}{\rho [v(q)]^2}$$

with $v(q)$ the velocity of sound.

Thus the cross section for scattering from density waves in a simple liquid is

$$\frac{d\sigma_{VV}}{d\Omega} = \left(\frac{1}{4\pi}\right)^2 \left(\frac{\omega_0}{c}\right)^4 (\epsilon-1)^2 kT \beta_s(q) V.$$

This scattered light will appear spectrally as a doublet with frequencies

$$\omega_s = \omega_0 \pm \omega(q)$$

where $\omega(q) = q v(q)$

is the assumed dispersion relation for these density waves. The spectral cross section can then be written completely in terms of experimentally determined parameters as

$$\frac{d\sigma_{VV}}{d\Omega} = \left(\frac{1}{4\pi}\right)^2 \left(\frac{\omega_0}{c}\right)^4 (\epsilon-1)^2 \frac{kT V}{\rho v(q)^2} \times$$

$$\left[\frac{\Gamma(q)}{\omega_s - \omega_0 - \omega(q)^2 + \Gamma(q)^2} + \frac{\Gamma(q)}{\omega_s - \omega_0 + \omega(q)^2 + \Gamma(q)^2} \right]$$

where $\Gamma(q) = \frac{1}{\tau(q)}$ is the relaxation rate of the waves.

This last result is cumbersome so in the remainder of the paper we shall merely calculate the total intensity scattered by a particular mode into some scattering polarization and then recall that this intensity is spread over a doublet with Lorentzian peaks of full width at half maximum of $2\Gamma(q)$ centered at the frequencies $\omega_s = \omega_0 \pm \omega(q)$.

The cross section for scattering from longitudinal modes of an isotropic solid is very much like that for liquids. As a first approximation we suppose that we can estimate the variation of the dielectric constant with compression as being the same as the variation of the dielectric constant with density so that for a compressional strain x

$$\frac{\partial \epsilon}{\partial x} \approx \rho \frac{\partial \epsilon}{\partial \rho} \approx (\epsilon - 1),$$

then we can write the cross section for scattering (VV) from these modes as

$$\frac{d\sigma_{VV}}{d\Omega} = \left(\frac{1}{4\pi}\right)^2 \left(\frac{\omega_0}{c}\right)^4 (\epsilon - 1)^2 \frac{kT}{\rho v_L^2} V$$

where v_L is the velocity of the waves.

We then empirically generalize this last expression and state that one can probably get a reasonable estimate of the scattering intensity from the longitudinal modes of any condensed medium including crystals from the expression given. We have found that the scattering intensities of various media do seem to follow the ratios of intensity one would predict from the quantity

$$\frac{(\epsilon - 1)^2}{\rho v_L^2}$$

calculated from tables of elastic properties and refractive indices. Having an estimate of the scattering intensity for at least one mode a crystal is very useful in designing and setting up experiments. It should also allow estimates of the scattering cross sections for other modes of crystals by comparison of intensities in experimental spectral traces. Of course the above estimate will not be correct for crystals such as MgO which have a negative pressure coefficient of the index of refraction. (12)

SECTION II

THE THEORY OF BRILLOUIN SCATTERING IN CRYSTALS

In this section we wish to give a detailed discussion of Brillouin scattering in crystals. We will begin with a description of the acoustic modes of crystals. We then discuss scattering from these modes including the effect of birefringence of the crystals and the tensor property of the dielectric fluctuations. Our aim is to arrive at an experimentally oriented formulation of the scattering cross sections equivalent to specializations of the very general result given by Born and Huang.⁽¹³⁾ In particular we wish to give some "rule of thumb" selection rules for telling which phonon polarizations (displacement directions) can cause scattering in the different light polarization spectra.

Acoustic Modes

We take as our model of acoustic modes in crystals the results of the classical theory of elasticity.⁽¹⁴⁾ Thus we consider small (symmetrized) strains

$$x_{ij} = \frac{1}{2} \left(\frac{\partial u_i}{\partial r_j} + \frac{\partial u_j}{\partial r_i} \right) .$$

The internal energy per unit volume is written as

$$U(S, x_{ij}) = \frac{1}{2} c_{ij,kl} x_{ij} x_{kl} + U_0(S),$$

giving internal stresses proportional to the strain

$$X_{ij} = \frac{\partial U}{\partial x_{ij}} = c_{ij,kl} x_{kl},$$

where $\vec{u} = \vec{u}(\vec{r})$ is the displacement of the point at \vec{r} in the body, S is the entropy per unit volume of the body X_{ij} is the stress due to isentropic strains, and $c_{ij,kl}$ are the elastic stiffness constants.

The great amount of symmetry in the fourth rank tensor components $c_{ij,kl}$ reduce the number of parameters in this description to a manageable size. Due to the symmetries of x_{ij} and the product $x_{ij} x_{kl}$, we have

$$c_{ij,kl} = c_{ji,kl} = c_{ij,lk} = c_{kl,ij}.$$

Thus there are only 21 independent constants in the most general case.

The equation of motion is

$$\rho \ddot{u}_i = \frac{\partial X_{ij}}{\partial r_j}$$

with ρ the density of the medium. Using the symmetries given the equation of motion can be written as

$$\rho \ddot{u}_i = c_{ij,kl} \frac{\partial^2 u_k}{\partial r_l \partial r_j}.$$

We look for plane wave solutions of the form

$$\hat{u}(\hat{r}) = \hat{u} e^{i(\hat{q} \cdot \hat{r} - \omega t)}.$$

Substituting into the equation of motion gives the equations

$$(c_{ij,kl} q_l q_j - \rho \omega^2 \delta_{ik}) u_k = 0$$

The problem is then seen to be a 3×3 eigenvalue problem with secular equation

$$\left| c_{ij,kl} \hat{q}_l \hat{q}_j - \rho \left(\frac{\omega}{q} \right)^2 \delta_{ik} \right| = 0$$

where \hat{q}_k are the direction cosines of \hat{q} . This secular equation is a cubic equation in the quantity

$$C = \rho \left(\frac{\omega}{q} \right)^2$$

whose three real, positive roots $C_j = \rho v_j^2(\hat{q})$ determine the phase velocities $v_j(\hat{q})$ for the three, orthogonal displacement plane waves propagating in the direction \hat{q} . Thus for each direction \hat{q} we get three dispersion relations of the form

$$\omega_j^2(\vec{q}) = v_j^2(\hat{q}) q^2.$$

With $v_j^2(\hat{q}) = \frac{c_j(\hat{q})}{\rho}$ $j = 1, 2, 3$.

It is this form of dispersion relation with $\omega(\vec{q}) \rightarrow 0$ as $q \rightarrow 0$ that marks an acoustic mode. This form of dispersion relation gives the frequency shifts observed in Brillouin scattering their characteristic scattering angle dependence for fixed \hat{q} direction

$$\Delta\omega = \pm v(\hat{q})q(\theta) = \pm v(\hat{q})2k_0 \sin \frac{\theta}{2}$$

or

$$\Delta\omega \propto \sin \frac{\theta}{2}.$$

This dependence is to be contrasted to that for scattering from the optical modes of vibration of a crystal where $\Delta\omega$ is usually independent of the scattering angle.

As a consequence of the angular dependence of the Brillouin

scattering frequency shifts, measurement of the scattering angle becomes an essential part of an experiment for which the spectrum is to be related to the elastic properties of the medium.

Before further discussion we change to the matrix notation⁽¹⁵⁾ in which pairs of subscripts are replaced with a single subscript running from 1 to 6 as follows:

$$\begin{array}{cccccc} 11 & 22 & 33 & 23 & 31 & 12 \\ & & & 32 & 13 & 21 \end{array}$$

goes to

$$\begin{array}{cccccc} 1 & 2 & 3 & 4 & 5 & 6 \end{array}$$

If we apply this subscript transformation directly to the stresses and the elastic stiffness constants and define the six component strain vector by the above transformation and

$$\begin{array}{ll} x_{ij} = x_m & m = 1, 2, \text{ or } 3 \\ 2x_{ij} = x_m & m = 4, 5, \text{ or } 6 \end{array}$$

then

$$U = \frac{1}{2} c_{ij} x_i x_j + U_0(S)$$

and

$$X_i = c_{ij} x_j.$$

c_{ij} is now a symmetric 6×6 matrix relating the six component strain to the six component stress.

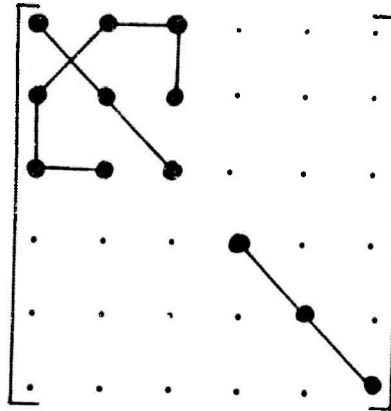
In crystals the symmetry operations of the various point groups greatly reduce the number of non-zero, independent components of the stiffness tensor. These reductions are nicely discussed and summarized in Nye⁽¹⁶⁾ for fourth rank tensors such as the stiffness tensor as well as for tensors of other ranks.

We will be discussing acoustic modes in monoclinic crystals of classes 2 and 2/m. They have the following matrix of independent fourth rank tensor components indicated by heavy dots

$$\begin{bmatrix} \bullet & \bullet & \bullet & \cdot & \bullet & \cdot \\ \bullet & \bullet & \bullet & \cdot & \bullet & \cdot \\ \bullet & \bullet & \bullet & \cdot & \bullet & \cdot \\ \cdot & \cdot & \cdot & \bullet & \cdot & \bullet \\ \bullet & \bullet & \bullet & \cdot & \bullet & \cdot \\ \cdot & \cdot & \cdot & \bullet & \cdot & \bullet \end{bmatrix}$$

For the stiffnesses this matrix is symmetric giving then 13 independent components.

For comparison a cubic crystal has the matrix



or three independent stiffnesses: c_{11} , c_{12} , and c_{44} . (Connected dots represent equal constants.) We note that a cubic crystal will appear isotropic elastically if

$$2 c_{44} = (c_{11} - c_{12}).$$

The three component eigenvalue problem for the phase velocities and mode polarizations is given in a convenient form with the stiffness constants in matrix notation by Mason⁽¹⁷⁾. Using these formulas and known elastic constants, it is a straightforward calculation to find the phase velocities and displacement vector direction cosines.

To quickly see the physical significance of the elastic constant matrix elements we chose a coordinate system with the x' axis along q and tensor components transformed to this coordinate system and then reduced to matrix elements. Then the secular equation for the phase

velocities becomes

$$\begin{vmatrix} (c_{11}' - \rho v^2) & c_{16}' & c_{15}' \\ c_{16}' & (c_{66}' - \rho v^2) & c_{56}' \\ c_{15}' & c_{56}' & (c_{55}' - \rho v^2) \end{vmatrix} = 0 \quad .$$

c_{16}' and c_{15}' give the coupling between compressional strains along x' and shear strains in the $x'y'$ and $x'z'$ planes. If this coupling is negligible then we get a pure longitudinal mode with polarization \hat{u} along x' and $v_L^2 = c_{11}'/\rho$. c_{56}' gives the coupling between shear strains in the $x'y'$ and $x'z'$ planes. If this coupling is also negligible then we get pure shear modes with polarizations and velocities: $\hat{u} \parallel y'$, $v_{T1}^2 = c_{66}'/\rho$ and $\hat{u} \parallel z'$, $v_{T2}^2 = c_{55}'/\rho$. It is very often the case that these off-diagonal elements are small compared to the diagonal elements so that the modes are reasonably described as longitudinal and transverse. Moreover c_{11}' is in practice always larger than c_{66}' or c_{55}' . This simplifies the interpretation of Brillouin spectra because we can always take as a first guess that the spectral component with the largest shift is the (quasi-) longitudinal mode component.

As an example and for later comparison with our experimental results we have calculated the velocities and mode polarizations for

a set of \hat{q} directions in the (010) plane of the crystal triglycine sulfate using the room temperature (monoclinic class C_2 phase) elastic constants determined from ultrasonic velocity measurements. (The elastic stiffness constants are listed in the Appendix.) The results are presented in Table II 1. The only symmetry in these velocities, $v(\hat{q}) = v(-\hat{q})$, shows that we need only calculate the velocities for half the directions in the plane. The \hat{q} direction is given in terms of the angle between \hat{q} and the c axis. (The conventional axes and coordinate systems of triglycine sulfate are given in the Appendix.) For this case the dynamical matrix is

$$\begin{bmatrix} \lambda_{11} & \cdot & \lambda_{13} \\ \cdot & \lambda_{22} & \cdot \\ \lambda_{13} & \cdot & \lambda_{33} \end{bmatrix}$$

with

$$\lambda_{11} = c_{55} + (c_{11} - c_{55}) \sin^2 \theta + c_{15} \sin 2\theta$$

$$\lambda_{33} = c_{55} + (c_{33} - c_{55}) \cos^2 \theta + c_{35} \sin 2\theta$$

$$\lambda_{13} = c_{15} + (c_{35} - c_{15}) \cos^2 \theta + \frac{c_{13} + c_{55}}{2} \sin 2\theta$$

$$\lambda_{22} = c_{55} \sin^2 \theta + c_{44} \cos^2 \theta + c_{46} \sin 2\theta$$

TABLE II 1

(010) PLANE ACOUSTIC MODE VELOCITIES IN TGS CALCULATED
FROM ULTRASONIC ELASTIC CONSTANTS^(a)

$\theta^{(b)}$	$v_L^{(c)}$	$v_{T1}^{(c)}$	$v_{T2}^{(d)}$	$\hat{q} \cdot \hat{U}_L^{(e)}$	$\hat{q} \cdot \hat{U}_{T1}$
($^\circ$)	10^5 cm/sec.	10^5 cm/sec.	10^5 cm/sec		
-90	5.20	2.53	1.92	+ .996	.089
-80	5.30	2.58	1.94	+ .998	.063
-70	5.37	2.53	2.00	+ .999	.044
-60	5.39	2.39	2.07	1.000	.000
-50	5.34	2.22	2.15	- .998	.063
-40	5.22	2.05	2.23	- .992	.126
-30	5.02	1.97	2.30	- .980	.199
-20	4.74	2.00	2.34	- .966	.258
-10	4.41	2.16	2.37	- .954	.300
0	4.06	2.38	2.37	- .958	.287
10	3.78	2.56	2.35	- .985	.172
20	3.75	2.51	2.30	+ .994	.109
30	3.96	2.27	2.24	+ .973	.231
40	4.24	2.05	2.16	+ .970	.243
50	4.50	1.96	2.08	+ .977	.213
60	4.73	2.03	2.01	+ .984	.178
70	4.92	2.21	1.95	+ .990	.141
80	5.08	2.40	1.92	+ .994	.109
90	5.20	2.53	1.92	+ .996	.089

(a) Constants from V. P. Konstantinova, I. M. Sil'Vestrova and K. S. Aleksandrov. *Soviet Phys.-Cryst.* 4, 63 (1960).

(b) $\theta = \theta(q)$ in $xyz = -a-bc$ coordinate system.

(c) L and T1 modes polarized in (010) Plane.

(d) T2 polarized $\parallel b$.

(e) + sign indicates that \hat{U}_L is ahead of \hat{q} and vice versa for - sign.

and θ the angle between \vec{q} and \vec{z} (\vec{c}).

We are aware that the present formalism is not consistent with atomic theories of elasticity and that the application of it to ferroelectric crystals (polar crystal classes) is particularly questionable. This point is critically discussed by Hearmon⁽¹⁸⁾. No serious discrepancies were found in comparisons of our velocity measurements for triglycine sulfate with calculated velocities using this formalism. In this case of a monoclinic crystal a critical test is not possible since the thirteen independent elastic constants of the classical theory probably represent enough parameters to fit any set of experimental velocities.

We have so far been considering a simplified equation of state with only strain and entropy as independent variables. Thermal diffusion of heat being a very slow process over distances of the order of visible light wavelengths we expect the choice of adiabatic strain waves to be an accurate description of the acoustic modes of crystals. We will later consider the acoustic modes in ferroelectric crystals. There as in all piezoelectric class crystals we must distinguish between (adiabatic) fluctuations with electric field E held constant and fluctuations with the electric polarization P (or displacement D) constant.

For those modes from which we can scatter light in crystals we expect Brillouin scattering spectra to yield velocities which accurately represent the limit

$$\left(\frac{\omega}{q}\right)_{q \rightarrow 0} \longrightarrow v(\hat{q}) .$$

That is to say that with the available magnitudes of \hat{q} in light scattering we do not expect to see any curvature in the acoustic mode dispersion relation. Thus the Brillouin scattering velocity measurements should agree very closely with those from ultrasonic measurements.

The advantages of Brillouin scattering measurements of velocities compared to acoustic techniques are that they are now at least as accurate as ultrasonic pulse techniques, they allow very easy direction scans of the anisotropy of the velocities in crystals, and they can be made in the presence of extreme damping of the modes. The most important feature of the Brillouin scattering measurements for the present work is that the larger q (compared to ultrasonics) give higher frequencies which allow fast relaxation processes to be studied.

Brillouin scattering provides much less information about the acoustic mode dispersion relation than the coherent inelastic neutron

scattering experiments. Nevertheless because of the high spectral resolution Brillouin scattering can show very small changes in the $q \rightarrow 0$ part of the dispersion relations, that is in the sound velocity, due to externally controlled changes of temperature, applied fields, stresses, or the like. This is a great advantage in the study of phase transitions.

Brillouin Scattering Cross Sections for Crystals

We turn now to an account of the photoelastic coupling for Brillouin scattering in a crystal.⁽¹⁹⁾ We describe the average optical properties of our crystal by a symmetric second rank tensor. (We assume our crystal not to be optically active.) We chose an orthogonal coordinate system which coincides with the principal axes of this tensor. In this coordinate system the local dielectric tensor is

$$\epsilon(r, t)_{ij} = \epsilon_i \delta_{ij} + \Delta\epsilon(r, t)_{ij} .$$

In experiments we wish to have a single known scattering vector \vec{q} -- known in magnitude and direction. If we send the incident light through the sample in an arbitrary direction with an arbitrary polarization direction with respect to the principal axes then we will in general get two incident beams each giving rise to two scattered beams in the collection direction. This gives a total of up to four \vec{q} . Each \vec{q} can give up to three Brillouin doublets in a spectrum. The

spectrum could show as many as twelve doublets!⁽²⁰⁾ Thus we will usually want to choose somewhat specialized orientations of the crystal in experiments.

The orientation which we used and will discuss here was that of placing one of the principle axes of the average dielectric tensor perpendicular to the scattering plane (the plane containing the incident and scattered light wave vector directions). Call this the z axis for the present discussion. In the notation of Section I with directions parallel to z labeled V and perpendicular to z labeled H we consider spectra obtained with incident and scattered light polarization combinations VV, VH, HV, and HH. For each spectrum there is a definite \hat{q} ,

$$\hat{q} = \hat{k}_o - \hat{k}_s$$

where \hat{k}_o and \hat{k}_s directions are fixed externally and their magnitudes are determined by the crystal refractive index for the corresponding direction and polarization.

Consider first the cross sections for the scattering of a V polarized incident beam. The simplest is

$$\frac{d\sigma_{VV}}{d\Omega} = \left(\frac{1}{4\pi}\right)^2 \left(\frac{\omega_o}{c}\right)^4 \langle |\Delta\epsilon(q, t)_{33}|^2 \rangle V^2 .$$

We see that the scattering is due to a Fourier component of the 33 (zz) component of the dielectric fluctuation tensor. The VH cross section is more complicated. We must project the source polarization, induced in the dielectric fluctuation by the incident field, onto the direction \hat{e}_s of the electric field for plane electromagnetic waves polarized in the scattering plane and traveling in the direction \hat{k}_s . If we denote the angle between the electric displacement in the scattered wave and the electric field as δ_s and the refractive index for this scattered wave as n_s , then the cross section is

$$\frac{d\sigma_{VH}}{d\Omega} = \left(\frac{1}{4\pi}\right)^2 \left(\frac{\omega_o}{c}\right)^4 \left(\frac{n_s \cos \delta_s}{\sqrt{\epsilon_3}}\right) \langle |\Delta\epsilon(q, t)_{13} e_{s1} + \Delta\epsilon(q, t)_{23} e_{s2}|^2 \rangle V^2.$$

Similarly we find that the other cross sections

$$\frac{d\sigma_{HV}}{d\Omega} = \left(\frac{1}{4\pi}\right)^2 \left(\frac{\omega_o}{c}\right)^2 \left(\frac{\sqrt{\epsilon_3}}{n_o \cos \delta_o}\right) \langle |\Delta\epsilon(q, t)_{31} e_{o1} + \Delta\epsilon(q, t)_{32} e_{o2}|^2 \rangle V^2$$

$$\frac{d\sigma_{HH}}{d\Omega} = \left(\frac{1}{4\pi}\right)^2 \left(\frac{\omega_o}{c}\right)^2 \left(\frac{n_s \cos \delta_s}{n_o \cos \delta_o}\right) \langle \left| \sum_{i,j=1}^2 \Delta\epsilon(q, t)_{ij} e_{oi} e_{oj} \right|^2 \rangle V^2$$

with δ_o and n_o defined for the incident wave polarized in the scattering

plane as δ_s and n_s were for the scattered wave. These last three cross sections involve combinations of dielectric tensor fluctuation components. In practice the situation is simplified because δ_s and δ_o are approximately zero. By taking a scattering angle of 90° we can then study (approximately) individual tensor component fluctuations: VV scattering probes $\Delta\epsilon_{33}$, VH probes $\Delta\epsilon_{31}$, HV probes $\Delta\epsilon_{32}$, and HH probes $\Delta\epsilon_{1'2'}$, where $1'$ is parallel to k_o and $2'$ is parallel to k_s .

To complete our description we must compute the coupling between the acoustic mode strains and the changes in the dielectric tensor and we must compute the mean square strain for each mode.

The standard treatment of the coupling is in terms of the Pockels elasto-optical coefficients $p_{ij,kl}$.⁽²¹⁾ They relate strains (second rank tensor) to changes in the dielectric impermeability (second rank tensor) and so form a fourth rank tensor. Like the elastic stiffness constants the Pockels coefficients have the symmetry

$$p_{ij,kl} = p_{ji,kl} = p_{ij,lk}$$

and can be reduced directly to matrix notation giving a 6×6 matrix. In general $p_{mn} \neq p_{nm}$ so there are usually more independent Pockels coefficients than elastic stiffness constants.

The Pockels coefficients are dimensionless and usually fall in

the range 1 to .01 . p_{mn} with $m, n = 1, 2$, or 3 is usually much larger than p_{mn} with $m = 4, 5$, or 6. This corresponds to the fact that electrostriction is a stronger effect than shear strain induced birefringence. These coefficients have not been measured for most crystals. Most of the measured values are for cubic crystals. Tables of measured p_{mn} can be found in Nye⁽²²⁾ and Landolt-Bornstein.⁽²³⁾

Crystal symmetry reduces the number of non-zero, independent coefficients. For each crystal class the allowed coefficients and relations between them are tabulated in references such as Nye. For the monoclinic and cubic ($m3m$) classes the matrices look the same as shown earlier for the elastic stiffness constants, the monoclinic class matrix being nonsymmetric and the cubic matrix symmetric.

We want to compute $\partial \epsilon_{ij} / \partial x_{kl}$. In terms of Pockels coefficients this is

$$\frac{\partial \epsilon_{ij}}{\partial x_{kl}} = - \epsilon_{im} p_{mn, kl} \epsilon_{nj} .$$

If we take orthogonal coordinates coincident with the principal axes of the dielectric tensor this derivative simplifies to

$$\frac{\partial \epsilon_{ij}}{\partial x_{kl}} = - \epsilon_i \epsilon_j p_{ij, kl}$$

with ϵ_i the set of three principal values of the dielectric tensor. For displacement wave

$$\vec{u}(\vec{r}, t) = \vec{u} e^{i(\vec{q} \cdot \vec{r} - \omega t)}$$

the unsymmetrized strain is

$$x_{kl} = \hat{u}_k \hat{q}_l u q e^{i(\vec{q} \cdot \vec{r} - \omega t)}.$$

Using these notations we calculate the appropriate dielectric fluctuations due to this single acoustic mode which is assumed to be a solution of the elastic wave problem discussed earlier. The basic result is that the (real) amplitude of the dielectric fluctuations is

$$\Delta\epsilon_{ij}(\vec{q}) = -\epsilon_i \epsilon_j (p_{ij, kl} \hat{u}_k \hat{q}_l) qu.$$

For example for VV scattering we want $\langle |\Delta\epsilon_{33}|^2 \rangle$. We find

$$\langle |\Delta\epsilon_{33}|^2 \rangle = \epsilon_3^2 (p_{33, kl} \hat{u}_k \hat{q}_l)^2 \langle |qu|^2 \rangle.$$

In this and the more complicated situations the result after projecting squaring and taking the ensemble average is proportional to $\langle |qu|^2 \rangle$.

This mean square Fourier strain component is easily calculated from

thermodynamic fluctuation theory⁽²⁴⁾ once the secular equation for the phase velocities is solved. We find for the j th mode

$$\langle |qu|^2 \rangle_j = \frac{kT}{VC_j} = \frac{kT}{V\rho v_j(q)^2}$$

where C_j is a root of the dynamical equation. This result may be looked upon as an expression of the equipartition of energy or (equivalently) a variance of a diagonalized 3×3 Gaussian distribution.

Since the mean square strain for each mode is non-zero, the basic selection rules for scattering from a particular mode in the polarized spectra come from the symmetry requirements that certain Pockels coefficients be zero or equal. The geometry of the mode and light directions gives the detailed selection rules.

The selection rules are most useful for 90° scattering. The basic features of selection rules for scattering from pure longitudinal and transverse modes are exhibited by cubic crystals and isotropic solids. For these media the VV cross section is proportional to p_{12}^2 and the scattering is from the longitudinal mode only -- (the spectrum would show only a single doublet), the VH and HV cross sections are equal and proportional to p_{44}^2 and the scattering is from the transverse mode with displacement vector perpendicular to the scattering plane only, and finally the HH cross section is proportional to p_{44}^2 and the scattering is from the longitudinal mode only.

In less symmetric crystals the polarized spectra do not generally sort the modes so nicely. Nevertheless it is still quite useful to note that the transverse mode polarized (more or less) perpendicular to the scattering plane will be expected to show up only in HV or VH spectra coupled through p_{ii} with $i = 4, 5$, or 6 . It would be possible to see peaks due to this mode in VV spectra coupled through p_{34} for example but in practice such constants when not forbidden are usually smaller than p_{44} and the like. When a doublet in addition to that due to the longitudinal mode shows up in a VV spectrum and does not appear in the VH spectrum, we can usually assume that it is due to the transverse mode polarized in the scattering plane.

As an example of selection rules we calculate the coupling between strain and dielectric fluctuations for modes with \hat{q} and the scattering plane parallel to the (010) plane of a monoclinic crystal. For VV scattering we want to know $\Delta\epsilon_{22}$. The relevant Pockels coefficients are p_{21} , p_{23} , and p_{25} . With notation for the direction cosines: $q = (l, 0, n)$ for the propagation direction, and $u = (\alpha, \beta, \gamma)$ for the displacement direction, we have

$$\Delta\epsilon_{22} = -\epsilon_2^2 [p_{21} l \alpha + p_{23} n \gamma + p_{25} (l \gamma + n \alpha)] qu.$$

We see that we couple only to modes polarized in the (010) plane. For pure longitudinal and transverse modes polarized in this plane we find the separate couplings to be:

$$\Delta\epsilon_{22}(L) = \epsilon_2^2 (p_{21} l^2 + p_{23} n^2 + 2p_{25} l n) q u$$

$$\Delta\epsilon_{22}(T) = -\epsilon_2^2 [(p_{23} - p_{21}) n l + p_{25} (l^2 - n^2)] q u.$$

Thus we see that longitudinal modes couple in the usual way through terms $\epsilon_2^2 p_{21}$ and $\epsilon_2^2 p_{23}$ which are similar to the electrostriction of isotropic materials. We see that the transverse modes depend on the difference in electrostrictive terms and the coefficient p_{25} . Both of these contributions should be small

Without going as far we can learn that the modes which gave the VV scattering above cannot give components in VH or HV spectra. For this coupling to exist we would need coefficients p_{4m} and/or p_{6m} with $m = 1, 3$, or 5 . These coefficients are rigorously zero so there is no coupling.

On the other hand the transverse waves polarized perpendicular to the scattering plane, which were not coupled into VV scattering, do give VH and HV scattering through the coefficients p_{44} and p_{66} . We will return to the details of these calculations in Section IV.

SECTION III

THE APPARATUS USED TO OBSERVE BRILLOUIN
SCATTERING IN CRYSTALS

In this section we will describe the light scattering apparatus used to observe the Brillouin scattering spectra reported in this thesis. It is essentially the same as that used by Chiao and Stoicheff. ⁽²⁵⁾

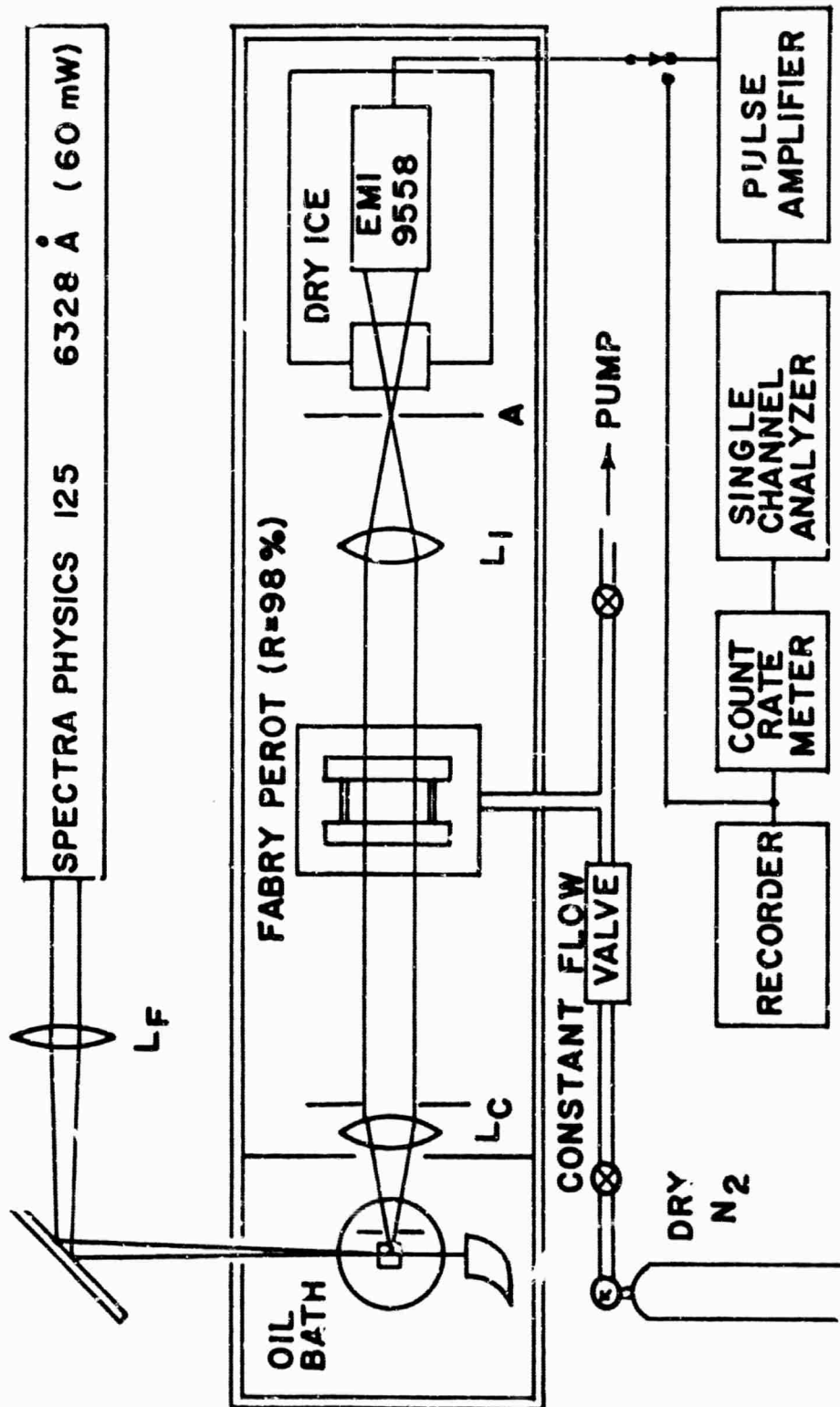
Our apparatus has been described in the literature in connection with Brillouin scattering in liquids. ⁽²⁶⁾

We first describe the layout of the apparatus. Then we will discuss the components of the system with emphasis on the Fabry-Perot interferometer. Next we describe the alignment of the system. Finally we describe the raw data reduction from the spectral traces.

Layout of the System

The layout of the apparatus is shown in Figure III 1. The optical path is described as follows. Sixty mw of plane polarized, 6328 Å light from a Spectra Physics Model 125 He-Ne laser is focused by a 50 cm focal length lens into the sample. Light scattered at 90° to the incident beam from a short length of the sample volume through which the beam passes is collected by a 17 cm focal length lens and focused at infinity. This light then passes through a variable stop (the system aperture stop), which determines the collection solid angle and the diameter of the Fabry-Perot etalon plates used. Next the selected scattered light goes to the pressure scanned Fabry-Perot interferometer. The normal to the plates of this interferometer is aligned with the

Fig. III Brillouin scattering apparatus. L_F has a 50 cm FL. Lens L_C has a 17 cm FL. Lens L_I has a 36 cm FL. Pinhole aperture A is 1.3 mm in diameter.



ray from the selected scattering volume in the sample. The light from this volume element which is in the pass band of the Fabry -Perot is transmitted. It is focused by a 36 cm focal length lens onto a pinhole of 1.3 mm diameter. Behind the pinhole is a dry ice cooled EMI 9558 photomultiplier which detects the light coming through the pinhole.

The photocurrent from the photomultiplier can be processed in one of two ways. For intense scatterers the photosignal across a load resistor was recorded directly on a potentiometric recorder. Alternately, for weak scatterers we use a photon counting system which selects the pulses from the photomultiplier by height and gives a dc output proportional to the selected pulse rate which is recorded.

Running a spectrum is straightforward. With the apparatus aligned and operating and with the box containing the Fabry-Perot etalon evacuated, we allow a constant flow of nitrogen to enter the evacuated box while recording the photosignal. A constant gas flow rate gives a constant frequency scan rate of the Fabry-Perot pass bands so that the time axis of the strip chart recording is directly proportional to frequency.

The Fabry-Perot Interferometer

The heart of the spectrometer for Brillouin scattering is the pressure scanned Fabry-Perot interferometer. It offers high transmission with high resolution, smooth precise scanning of the pass bands, and easy calibration.

In essence the interferometer consists of a Fabry-Perot etalon mounted in a sealed box allowing the pressure (density) of the gas surrounding the etalon and filling the cavity space between the etalon plates to be slowly changed at a controlled rate. The etalon consists of a pair of flat, parallel, semi-reflecting mirrors which face each

other at a fixed separation to form a cavity in which light can be multipli-reflected.

The traditional theory and practice of Fabry-Perot etalons is well presented in Born and Wolf.⁽²⁷⁾ Modern application in particular pressure scanned interferometers for use with photo-electric recording of spectra are reviewed by Jacquinet.⁽²⁸⁾

We will not discuss Fabry-Perot interferometers in full detail. We will simply give a quick review of the etalon characteristics of scanned transmission fringes, maximum transmission, finesse, and contrast. Then we will point out some design features of our interferometer and give the specific parameters of our etalon.

The Fabry-Perot etalon has an m th order interference transmission peak (pass band) when the condition

$$m\lambda = 2nd \cos i$$

is satisfied, where λ is the wavelength of the light, n is the refractive index of the medium in the cavity, d is the spacing between the etalon plates, and i is the angle of incidence of the light on the etalon. With monochromatic light incident this interference condition yields a set of bright transmission fringes in the form of concentric rings. For a given fringe labeled m the interference condition shows that as nd is increased, $\cos i$ must decrease. Therefore the fringe expands (i increases).

In the pressure scanning system that we used d was constant and n was varied linearly in time by changing the density of the gas in the etalon cavity. Light incident on the etalon at $i \approx 0$ was transmitted

whenever $m\lambda = 2nd$ and focused to pass through a pinhole before being detected. Light at other angles formed ring fringes which were blocked by the pinhole plate.

With this pinhole arrangement the etalon acts as a filter for the light incident normal to the etalon plates. For a gas medium between the plates [$(n-1) \ll 1$] and $\lambda \ll d$ the pass bands of this filter are spaced $\Delta\sigma = (1/2d) \text{ cm}^{-1}$ apart in frequency. ($1 \text{ cm}^{-1} = 30 \text{ GHz}$.) This separation is called the free spectral range. As the density of the gas changes the refractive index changes in proportion causing the frequency of the pass bands to scan. The simultaneous frequency changes of the pass bands is given by

$$\frac{\delta\sigma}{\sigma} = -(1/\lambda) \delta n$$

Therefore a linear refractive index change will give a linear frequency scan of the pass bands. For $\lambda = 6328 \text{ \AA}$ light and nitrogen gas having $(n - 1) = .0003$ at one atmosphere pressure, we can scan the pass bands over a frequency range of $4.7 \text{ cm}^{-1}/\text{atm}$. A 3 mm etalon gives a free spectral range of $\Delta\sigma = 1.67 \text{ cm}^{-1} = 50 \text{ GHz}$ so that we can scan through 2.8 orders with one atmosphere of nitrogen.

As each pass band crosses the spectrum the intensity of the light passing through the pinhole is proportional to the spectral intensity. Detecting the light and recording the signal gives a series of spectral traces spaced $\Delta\sigma$ apart. $\Delta\sigma$ is determined by measuring the etalon spacer length. Thus the frequency scale on the trace of consecutive spectra is known so that frequency shifts may be determined by interpolation.

The maximum transmission of the etalon is determined by the losses at the cavity surfaces. For perfectly flat plates having coatings with reflectivity R and transmission T the maximum transmission is $[T/(1 - R)]^2$. If there are no losses (scattering or absorption in the mirror coatings) then $T = 1 - R$ and the maximum transmission is 1. In practice R is often greater than .95 so that small amounts of absorption or scattering greatly reduce the maximum transmission. Also, the lack of plate flatness causes different parts of the cavity to transmit at different times so that the peak transmission of the whole working aperture of the plates appears reduced.

The finesse of the instrument is the ratio of the full width at half maximum of a transmission peak to the free spectral range. For perfectly aligned and perfectly flat plates it would be determined only by the reflectivity R of the individual (identical) plates and given by

$$F_R = \pi\sqrt{R}/(1 - R) .$$

We see that for R close to one, F_R is very large.

In practice the etalon finesse is limited by plate flatness. For plates having rms deviations of λ/m , the limiting finesse would be about $m/4$. If the plates have a smooth deviation from perfect flatness and/or parallel alignment then the effective finesse can be improved by using a smaller diameter of the plates thereby limiting the maximum difference in plate separation.

So far our discussion has indicated that trying to increase the finesse of an etalon by increasing the plate reflectivity can be useless

and even detrimental to overall performance through reduced transmission. With this in mind the present flatness limit for available plates of $\lambda/200$ would indicate that the plate reflectivity should be kept $\leq .94$ to approach a limiting finesse $F_F = 50$.

This limitation on the plate reflectivity would be correct were it not for the importance of the contrast of the etalon in looking at Brillouin scattering from real (dirty) crystals.

If one is trying to detect a weak Brillouin component which is next to a strong Rayleigh component then the instrumental contrast (discrimination) can be more important than the maxin transmission.

The contrast is the ratio of the maximum to the minimum transmission. If we take the transmission integrated over a peak between half maximum points and compare this to the transmission integrated over the same band width centered at the minimum transmission we find the effective contrast ratio. It is approximately the same as the contrast, $4(F_R/\pi)^2$, for an etalon with perfectly flat plates. Thus we see that increasing the reflectivity R to increase the finesse F_R can strongly increase the effective contrast even when the finesse is limited by the flatness finesse F_F .

In our etalon we have used $R = .98$ ($F_R = 156$) coatings on $\lambda/100$ plates ($F_F = 25$) giving a contrast of 10^4 in order to be able to suppress the instrumental wings of strong Rayleigh components in the region of the Brillouin components.

Successful exploitation of the choice of a high contrast etalon requires that the light detection system be very effective otherwise

signal-to-noise limitations will make weak components impossible to detect even with no Rayleigh wing present.

As an example of the usefulness of a high contrast etalon, the first successful thermal Brillouin scattering in glass other than fused quartz was done with our interferometer.⁽²⁹⁾ Previous attempts by other investigators were unsuccessful due to the very strong Rayleigh component in the light scattering spectra of glass.

Our interferometer was of special design. The tuning adjustments (plate alignment) were made with a gear and feedthrough arrangement which allowed tuning while the box surrounding the etalon was evacuated. These adjustments remained independent of the pressure at all times. The vacuum box had rotation and height adjustment screws. With the cavity tuned to give sharp fringes we could precisely locate the center of the fringe pattern (viewed in a telescope) on the intended scattering volume.

The pressure scan was linearized with a constant differential flow controller made by Moore Products (Spring House, Pa., Model 63 BU-L). The high pressure side of this valve was kept at 2 atm pressure by the nitrogen cylinder regulator valve. With this back pressure the flow rate was constant within 1%/order for a 3 mm etalon spacer.

Perkin-Elmer fused quartz, 2 inch diameter, $\lambda/100$ interferometer flats were used in the etalon. They were coated for $R = .98$ at 6328 \AA . We used 1.7 to 2.5 cm diameter areas of the center of the plates. The overall working finesse shown by the recorder traces was 25 to 35 with the 3.005 mm spacer. Peak

transmission for small areas of the plates was 10% as measured with a direct laser beam, but this includes the effect of the band pass of a small area of the plates ($F = F_R$) being less than the laser linewidth (1 GHz).

The Photomultiplier

We used an EMI 9558 B (S-20) photomultiplier. The tube was cooled to the temperature of dry ice by surrounding the tube with a cylindrical metal chamber containing a dry ice-methanol slurry. This chamber with the tube facing along the cylinder axis was encased in plastic foam for insulation. The signal light coming to the photomultiplier passed through an evacuated double window which prevented condensation of water vapor on the tube face. The voltage divider resistor chain was outside the cooling chamber. It was covered by a sealed box but was otherwise unpotted. Leakage currents caused by condensation were never found to be a problem because the resistors stayed cold enough to be frost covered rather than wet.

The tube had a $112 \mu\text{A/L}$ cathode sensitivity, a gain of 10^6 at 1250 V and a room temperature dark current of approximately 4 nA at this voltage. On cooling the dark dropped to less than 0.4 nA. Later in the work the cathode dark current of the cooled tube was measured with the counting equipment to be 95 ± 10 counts/sec.

Direct recording of weak photosignals (the voltage on a 1 meg ohm load resistor developed by the photocurrent) was limited by large spikes which occurred with our particular tube. The single channel analyzer of the counting system to be described below took

care of this nicely and allowed us to go to much longer integration times.

For direct recording we used 1250 V on the tube and for photon counting we used 1550 V.

Signal Processing

The data of Section V was taken by directly recording the voltage developed across a 1 Meg ohm load resistance by the photomultiplier anode current. Because of extraneous spikes in the photomultiplier output this system was limited to integration times of less than 1/2 sec. (set by the recorder).

Later work presented in Section IV was done with a photon counting system. The signal is processed in the following sequence of components. (1) An emitter follower matches the high impedance of the photomultiplier to the pulse amplifier impedance. (2) A Sturup Model 101 linear pulse amplifier amplifies the pulses to a convenient size for the analyzer. (3) A Sturup Model 701 single channel analyzer selects only those pulses which are of the height to have been initiated from photoemission at the photomultiplier cathode. The output of the analyzer was uniform pulses, one-for-one with the selected input pulses. With the EMI 9558 photomultiplier that we used the predominant noise consisted of large spikes which were much larger than the pulses produced by photocathode events. These were removed by the analyzer. The baseline was set low because there was a distribution of cathode pulse heights. There was very little noise consisting of short pulses. (4) A Sturup Model 2201 count ratemeter gives a dc signal proportional to the average pulse rate from the analyzer. The final signal filtering was chosen with

1, 5, or 10 sec time constants. (5) The count ratemeter output is recorded with a Honeywell Elektronik 19 recorder.

This system worked very well. It was limited to signals of less than 100 k count/sec and required slow scanning rates in order to prevent the ratemeter output from being distorted by the final stage time constant. We used scan rates set so that it took 10 x (time constant) seconds to cross the full width at half maximum of the components in the spectrum.

In the work on TGS typical count rates were 3×10^3 counts/sec at the maximum of a longitudinal mode Brillouin component.

The Fabry-Perot Aperture Stop

An iris diaphragm was placed between the collecting lens (L_C) and the Fabry-Perot. It had two important functions. First it limited the diameter of the Fabry-Perot plates used. This was important in achieving reasonably good finesse. Second it defined the collection solid angle for the scattering. It was usually used with a 1.7 cm diameter opening. With a 17 cm focal length lens this gave an f/10 system.

The choice of collection solid angle has a special importance in Brillouin scattering because of the angular dependence of the frequency shifts. With an f/10 system the angular aperture is 0.1 radians so the range of frequencies collected at a scattering angle of 90° is roughly $(1/20) \Delta\nu_{90^\circ}$. $\Delta\nu_{90^\circ}$ was ≤ 18 GHz in TGS. Therefore the broadening due to the collection solid angle is less than 0.9 GHz. The linewidth data on TGS given in Section V was taken with a 1 cm diameter aperture. In this case the broadening due to the collection solid angle was less than 0.5 GHz.

The Pinhole Aperture

The pinhole aperture (field stop) was mounted on a worm gear, x-y adjustment microscope stage. This allowed very precise centering of the pinhole on the image of the fringes formed by the imaging lens (F_I).

The choice of pinhole diameter is crucial to the actual operation of the system. Clearly in order to trace out the central fringe intensity profile as the Fabry-Perot is scanned the hole diameter should be small compared to the diameter of the central fringe. On the other hand, since the light intensity is low, signal-to-noise considerations require that the pinhole diameter be as large as possible.

We found the choice of an angular diameter of 3.6×10^{-3} radians to be a reasonable compromise for operation with a He-Ne laser (1 GHz linewidth) and a 3 mm etalon ($F \approx 30$).

The pinhole limits the length of the beam from which light is detected. The 1.3 mm diameter pinhole selected a 0.6 mm length ($=L$) of the laser beam in the sample.

The Oil Bath

The samples were placed in a 16 cm diameter cylindrical oil bath. This bath provided index matching and temperature control. The oil was light paraffin oil which had been filtered through a 1 micron Millipore filter to remove dust. The temperature of the stirred oil was regulated with a silicon control rectifier proportional control using a thermistor sensor and driving a 100 W heating coil. Further discussion of the temperature control and measurement can be found in Section V.

An additional mask was placed in the bath close to the sample to keep extraneous light from being collected.

Polarizers

The incident beam polarization direction was controlled with a Spectra-Physics Model 310 polarization rotator. The analyzing polarizer in the scattered beam was a HN38 polaroid filter.

Initial Alignment Procedure

The initial alignment consisted of positioning the cylindrical bath and setting the scattering angle. The angle at which \hat{k}_0 the incident beam direction crossed the spectrometer axis (optical rail) was set close to 90° by autocollimation with a $45^\circ - 90^\circ - 45^\circ$ prism. The angle was checked by running a Brillouin spectrum of water for which the 90° scattering Brillouin shift is known.

Then the bath was set on a flat bed optical rail rider. It was centered so the the \hat{k}_0 and \hat{k}_s directions were parallel to diameters of the cylinder by autocollimation simultaneously with two laser beams. One beam was the incident beam to be used in the experiment. The second was a beam sent along the spectrometer axis. With the oil bath positioned a water spectrum was taken to check the scattering angle.

In the present work the initial angle was found to be 90.0° in the oil bath. We had hoped to monitor the angle from time to time by running water spectra and so keep track of the scattering angle. It turned out that our water sample got dirty with time. The resulting large extraneous central component of the spectrum perturbed the

Brillouin component positions on the trace making accurate measurement of the shift impossible. Nevertheless the TGS measurements were consistent so that the angle remained $\theta = 90 \pm 1^\circ$.

The $\theta = 135$ scattering angle was set and checked in a similar manner. The accuracy of the angle was lower but because the shift depends less on angle in the backward directions the uncertainty in the velocities reduced from the data was not increased. This angle was known to within $\pm 2^\circ$.

From the relation that the Brillouin shift is proportional to $\sin(\theta/2)$ we can derive that the uncertainty in a velocity determined from a Brillouin shift measurement due to an uncertainty in scattering angle is given by

$$\delta v/v = \cot(\theta/2) (\delta \theta/2) .$$

Therefore for $\theta = 90 \pm 1^\circ$ and for $\theta = 135 \pm 2^\circ$, $\delta v/v = \pm 0.9\%$.

Running Alignment Procedure

At least daily during the Brillouin scattering data runs the following alignment was performed. With the sample out of the laser beam and the beam crossing and scattering from the oil in the bath the position of the image of the beam with respect to the Fabry-Perot fringes was checked with a telescope placed between the Fabry-Perot and the imaging lens. The Fabry-Perot leveling adjustment was changed until the fringes were centered on the image of the scattering from the oil. (The Brillouin components of the oil were visible in the telescope during this adjustment.) Then the interferometer tuning

was checked with laser light scattered from a paper card placed between the collecting lens and the interferometer. With the fringes sharp and brightly illuminated at all azimuthal angles, the fringes formed by the imaging lens on the pinhole plate were observed through a telescope and off axis lens. The fringes were slowly scanned with the pressure scan and the pinhole was carefully centered on the central fringe of the concentric circle fringe pattern. This positioning was very important in achieving a narrow, symmetrical, instrumental lineshape.

Checking the Fabry-Perot tuning and pinhole position could be done at any time by illuminating the Fabry-Perot fringes with the card scatterer. The sample position could be left untouched during these checks. This was important when the tuning and pinhole alignment had to be checked during a temperature run on a TGS sample.

With the spectrometer alignment complete the final step was to select the volume element in the sample from which to collect scattered light. This was done by placing the telescope after the Fabry-Perot and noting the position of the center of the Fabry-Perot fringe pattern on the telescope reticle. The telescope (with fixed orientation with respect to the spectrometer axis) was then moved to a position between the Fabry-Perot and the collecting lens. The sample was placed in the laser beam. The beam traversing the sample was examined through the telescope. The sample was attached by its mounting rod to a x-y adjustment microscope stage. This allowed fine adjustment of the sample position along and across the laser beam. The sample was searched until a "clean" (no inclusions or

strains, et.) volume was found. This part of the crystal was then moved to the position where its image fell on the reticle at the position previously noted to correspond to the center of the fringe pattern. In this way a clean portion of each sample was selected as the scattering volume.

It was interesting to note that during these visual examinations the Brillouin scattering from clean crystal samples was visible by eye giving a uniform delineation of the laser beam traversing the crystal.

Data Reduction

The Brillouin shift frequencies were measured from the recorder charts in the following way. The center of the peaks was determined by graphically dividing in half the width of the peaks near the half power level. The shift in orders (that is fraction of a free spectral range $\Delta\sigma$) was taken as the distance between the Stokes and anti-Stokes components (down-shifted and up-shifted components respectively) of the m th order spectrum divided by the sum of the $m-1$ to m anti-Stokes component separation and the m to $m+1$ Stokes component separation. Measuring in this way averages the component displacements on the trace in such a way that errors due to a uniform change of the scan rate are exactly cancelled. With the constant flow regulator used the flow rate decreased only 1% / order with a 3 mm etalon so that the averaging technique made the errors due to the scan rate negligible compared to other measurement uncertainties.

SECTION IVEXPERIMENTAL BRILLOUIN SCATTERING IN THE MONOCLINICCRYSTAL TGS

In this section we present the experimental observations of Brillouin scattering spectra for the monoclinic biaxial crystal triglycine sulfate (TGS). We will be concerned here with those properties of the scattering spectra which are common to monoclinic crystals and are not specifically related to the ferroelectric phase transition which occurs in this crystal. Thus the purpose of this part of the work is to present evidence in support of the formulation of light scattering in crystals in Section II and to show how well Brillouin scattering can be used to measure the elastic and photo-elastic properties of a low symmetry crystal. The Brillouin scattering observations concerned with the dynamics of the phase transition in TGS will be given later in Section V. Those readers who are mainly interested in the phase transition can omit this section and proceed to Section V.

Outline

A series of measurements were made with the (010) plane as the scattering plane. The spectra exhibit the frequencies of phonons having \vec{q} in the (010) plane. From these spectra through the use of polarization selection rules we have been able to identify all three acoustic modes and determine their velocities as a function of direction in the (010) plane. These velocities are then compared with velocities computed from elastic constants determined from ultrasonic velocity measurements.

From the variation of the intensity of the Brillouin components as the scattering direction is changed we obtained information about Pockels coefficients (elasto-optic).

Spectra were taken for \vec{q} parallel to \vec{b} but these showed only the component due to the longitudinal phonon.

Finally, the intensity of the scattering from the (quasi) longitudinal mode for a particular \vec{q} direction in the (010) plane was compared with the scattered intensity due to the longitudinal modes in fused quartz and water from which a reasonable estimate of the absolute scattering cross section was made.

Properties and Coordinates in TGS

Jona and Shirane⁽³⁰⁾ have collected references to many properties of TGS. From these references and later ones we have collected a data summary of the measured properties of TGS which are relevant to this work. They are collected in the Appendix along with a coordinate system convention.

In this work the convenient set of axes for describing directions was that of the reciprocal lattice. By convention the C_2 axis of a monoclinic crystal is taken as the b axis. The a and c axes are perpendicular to \hat{b} so that \hat{b} and \hat{b}^* are parallel. We follow Wood and Holden⁽³¹⁾ in the choice of a and c and we approximate $\beta = 105^\circ$ for later comparison with ultrasonic measurements. Our crystals had large c faces which allowed us to determine the direction of \hat{c}^* in the samples with respect to the incident direction \hat{k}_0 by autocollimation of the incident laser beam. Our notation for directions in the (010) plane will be to give the angle ϕ between the direction and the \hat{c}^* axis with ϕ taken as positive when on the \hat{a}^* side of \hat{c}^* . (See Fig. A1 in the Appendix)

The optical parameters of TGS have been carefully measured by Dion⁽³²⁾. As in all monoclinic crystals the b axis is one of the principle axes of the dielectric ellipsoid. In TGS it is the acute bisectrix having the lowest index of refraction $n_b = 1.484$. The two principle axes lying in the (010) plane are roughly (within 3°) parallel to the a^* and c^* directions and have the same index within 1%, $n_{ac} = 1.57$. Thus we make the convenient approximation of treating TGS as optically a uniaxial crystal. This greatly simplifies the reduction of the observed frequency shifts to acoustic mode velocities.

Paraffin oil was used as the medium for the oil bath surrounding the crystal. The crystal is inert in this oil, the oil shows negligible evaporation at the highest temperatures reached in this experiment (55°C) and it very nicely matches the index of refraction, n_b , of the crystal⁽³³⁾. The index match cut down the extraneous scattering at the surface of the crystal and allowed light polarized parallel to b to pass through the faces of the sample undeflected. This was very convenient because the phonons of greatest interest give components in VV scattering when the scattering plane is parallel to (010) and so involve just those polarizations of light which are index matched.

The slight mismatch in the oil index and n_b could give at most 1% changes in the Brillouin shifts. Worst cases occur at $\phi(q) = 0^\circ$ and 90° .

Scattering Vectors

Table IV 1 gives the scattering vectors for (010) plane scattering in TGS with a He-Ne laser. The expression there for q_{VV} is rigorously true for all $\phi(q)$. The expression for q_{VH} is true in the approximation

TABLE IV 1

SCATTERING VECTORS (010) PLANE IN TGS

θ	POLARIZATION	$\frac{q}{2\pi}$ (10^4 cm^{-1})
90.0°	VV	3.317
90.0°	VH, HV	3.410
135.0°	VV	4.335

$$q_{VV} = 2\pi \frac{n_b}{\lambda} 2 \sin \theta/2$$

$$q_{HV}^{(90^\circ)} = 2\pi \sqrt{\frac{n_o^2 + n_b^2}{\lambda}} = q_{VH}^{(90^\circ)}$$

$$n_b = 1.484$$

$$n_o = 1.57$$

$$\lambda = 6.328 \times 10^{-5} \text{ cm}$$

of taking TGS as uniaxial about the b axis. With these scattering vectors we can reduce 90° and 135° scattering angle Brillouin frequency shifts to acoustic velocities since

$$\Delta\omega = vq \quad \text{rad./sec. ,}$$

or

$$\Delta\nu = \left(\frac{v}{c}\right) \left(\frac{q}{2\pi}\right) \quad \text{cm}^{-1}$$

with c the velocity of light,

or

$$\Delta\nu = v \left(\frac{q}{2\pi}\right) \quad \text{Hz .}$$

In this work we take $c = 3.000 \times 10^{10}$ cm/sec.

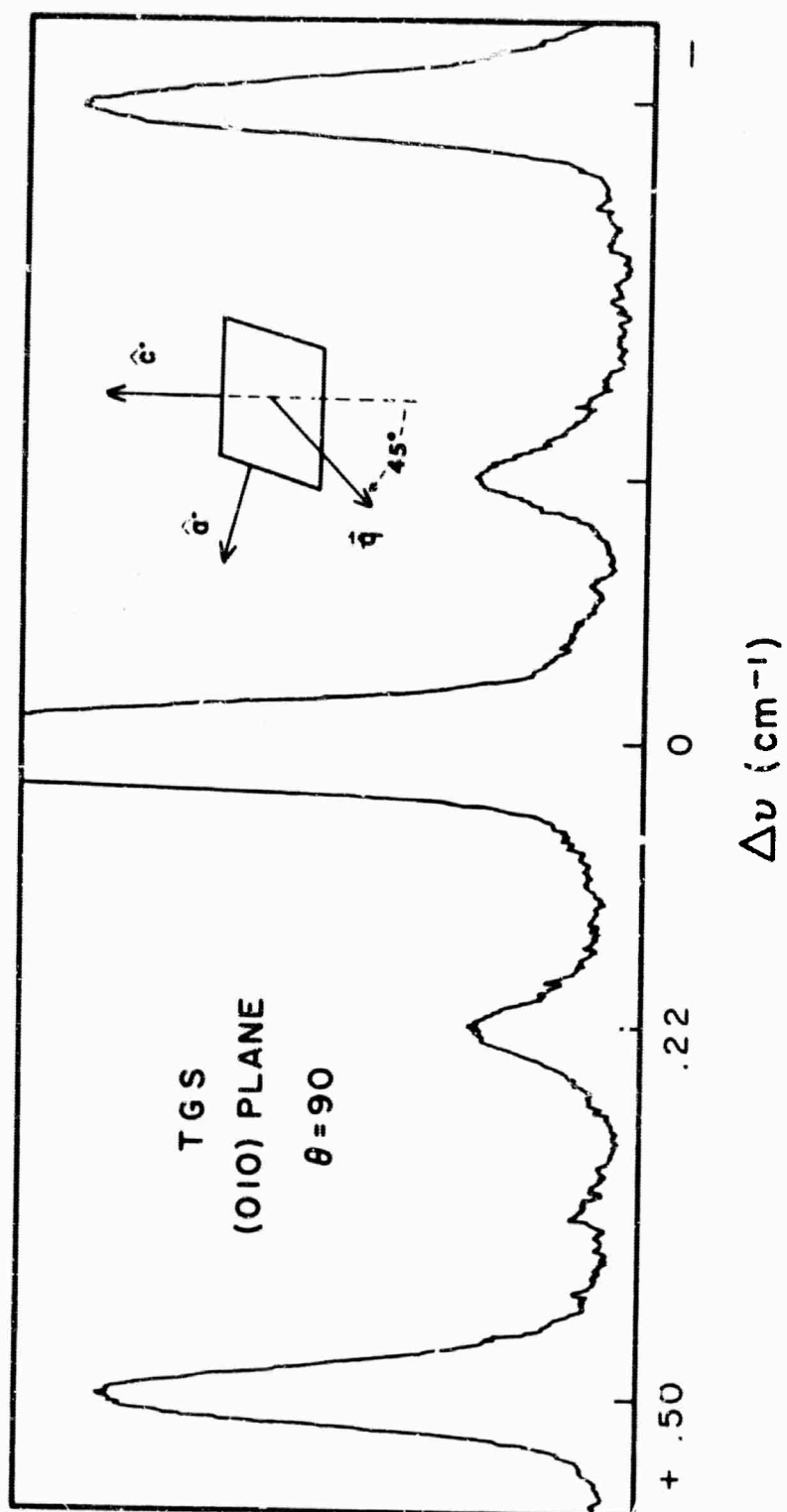
The scattering angles as checked with scattering spectra of water were $(90 \pm 1)^\circ$ and $(135 \pm 2)^\circ$.

The Experimental Spectra

Figure IV 1 shows a typical VV, (010) plane Brillouin scattering spectrum of TGS for a scattering angle of 90° and $\phi(q) = -45^\circ$. We see that at this angle we couple to two acoustic modes. From the selection rule given in Section II we know that $\Delta\epsilon_{22}$ is modulated only by the modes polarized in the (010) plane. We expect the large, high frequency peak to correspond to the (quasi-) longitudinal mode and the other peak to correspond to a (quasi-) transverse mode.

The trace shown in Fig. IV 1 was made with direct recording of the photosignal. It is typical of the spectra used to study the temperature

Fig. IV 1 Typical Brillouin scattering spectrum in TGS at $T = 34^{\circ}\text{C}$ showing transverse ($\Delta\nu = \pm 0.22\text{ cm}^{-1}$) and longitudinal ($\Delta\nu = \pm 0.50\text{ cm}^{-1}$) Brillouin components. Inset shows orientation of scattering vector \hat{q} with respect to the reciprocal lattice vectors in the (010) plane.



dependence of the Brillouin shifts which is reported in Section V. The final data taken for the velocity and intensity results to be given in this section were obtained using a photon counting detection system.

The calculation of the acoustic mode velocities and polarizations from elastic constants in TGS as given in Section II (Table II 1) shows that for each \vec{q} in (010) plane there is a pure shear mode with displacement vector perpendicular to the plane and a pair of mixed modes polarized in the plane with the quasi-longitudinal mode polarization direction within 18° of \hat{q} . From this calculation we can predict the Brillouin shift for the quasi-transverse mode. The shift approximately agrees with the observed shift.

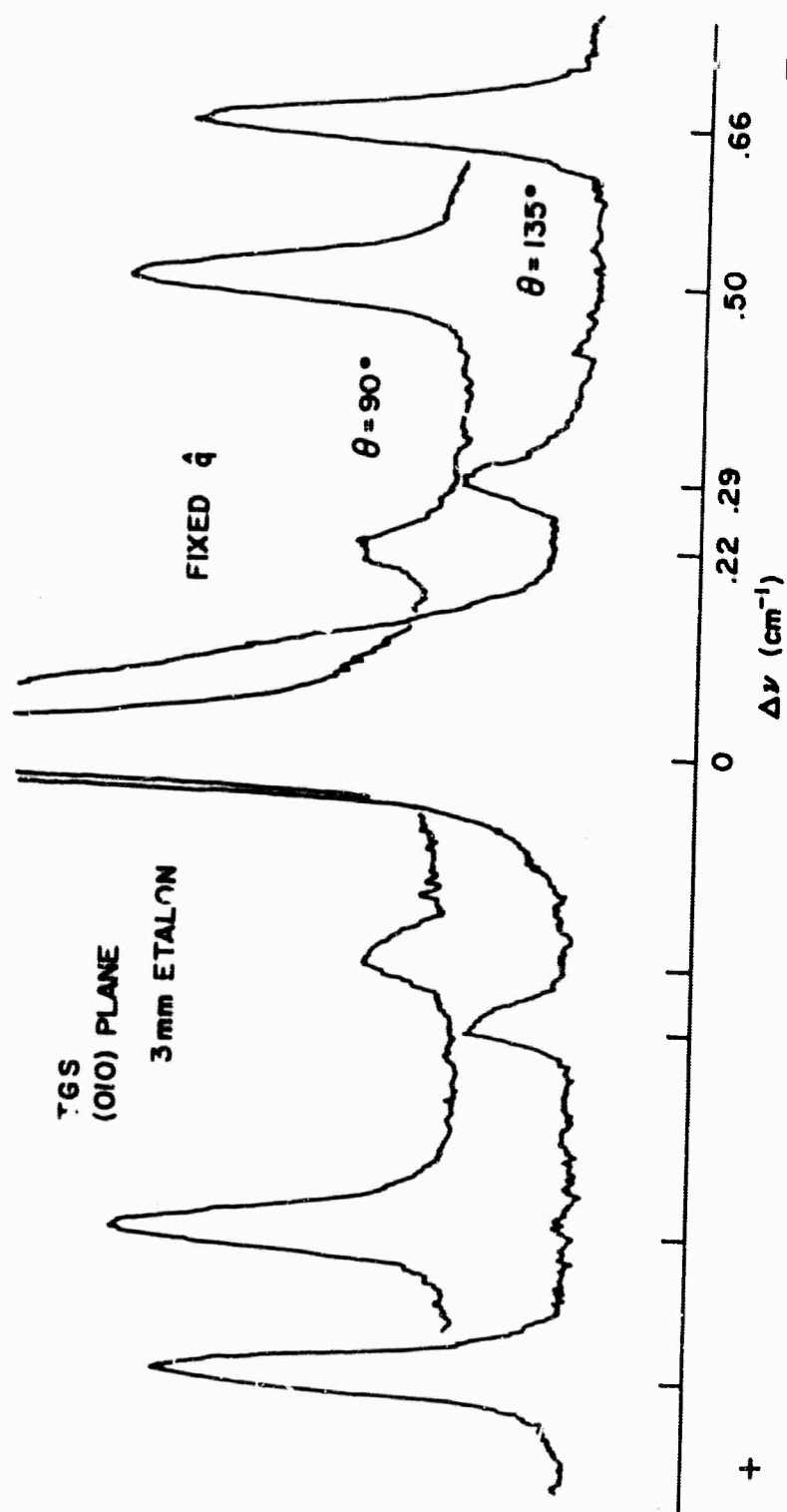
If we change the scattering angle θ but keep the q direction in the crystal fixed the cross section calculation for VV scattering shows that the relative intensity of the components should remain the same. From the expression for the Brillouin frequency shifts

$$\Delta\omega = v \ 2 k_0 \sin(\theta/2)$$

we know that increasing the scattering angle should increase the frequency shift in proportion to $\sin(\theta/2)$. These predictions are verified by the VV scattering spectra shown in Fig. IV 2. $\phi(q)$ was -45° for these spectra. The ratio of transverse to longitudinal component peak heights is .23 for both spectra and the ratio of corresponding Brillouin shifts in the two spectra is 1.32 which agrees with the theoretical ratio of 1.307 within the angular uncertainty in the experiment.

The spectra of Figs. IV 1 and IV 2 were taken at 34.4°C . The temperature dependence of the spectra will be discussed in Section V.

Fig. IV 2 Superimposed traces of Brillouin scattering spectra for scattering angles of 90° and 135° and the direction \hat{q} fixed at -45° to c^* .



The third acoustic mode for the $\phi(q)$ direction which consists of pure shear waves should only appear in VH and/or HV polarized spectra according to the calculations at the end of Section II. Fig. IV 3 shows a complete set of polarization spectra for (010) plane scattering with $\phi(q)$ at -45° . We see that for this \vec{q} direction the pure shear mode appears essentially only in HV scattering. The frequency shift of this component agrees with the predicted shift from the velocity calculation. Thus by taking polarized spectra we are able to very nicely sort out the three acoustic modes for a particular \vec{q} in agreement with the cross section predictions.

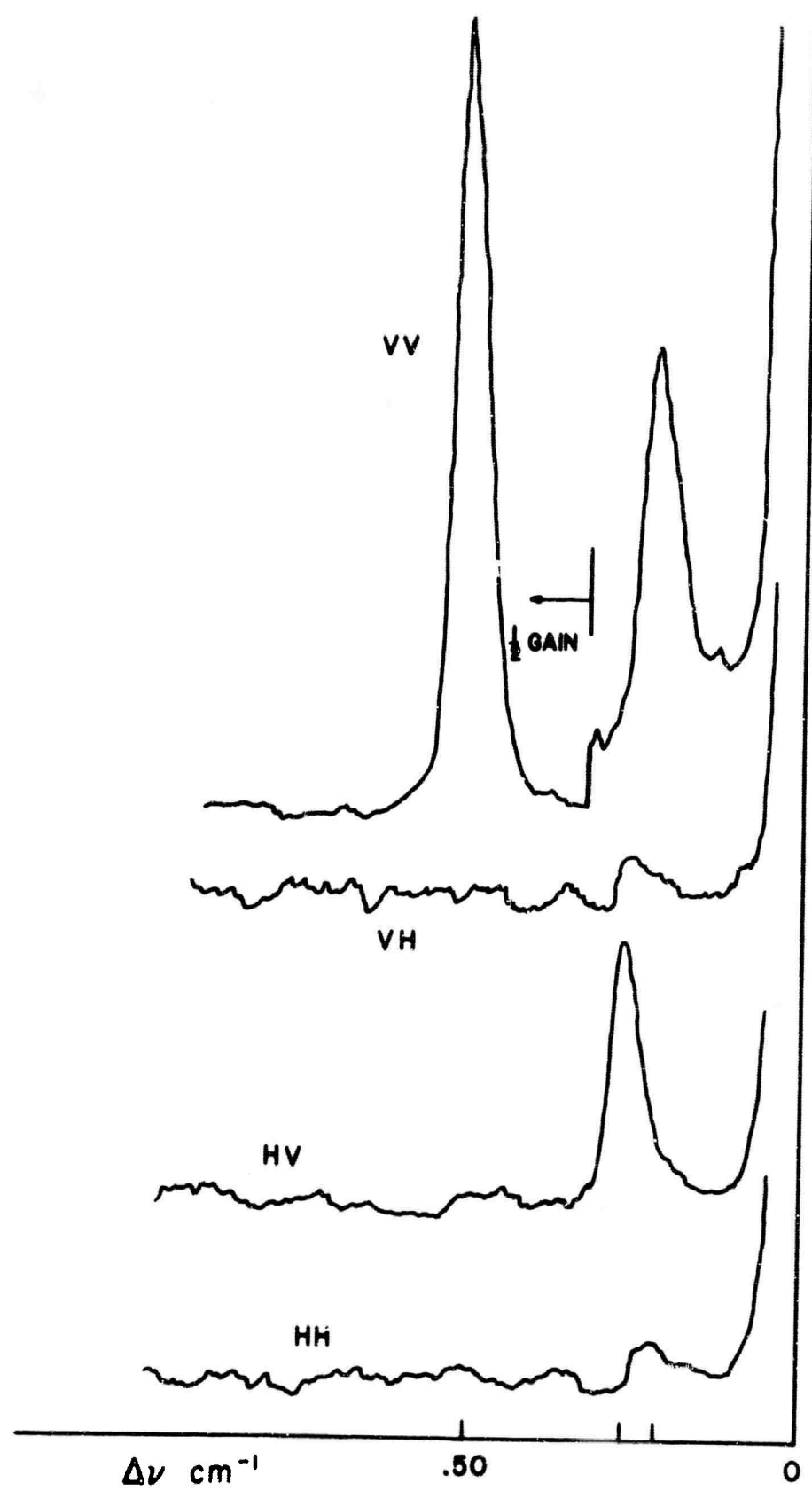
It is interesting to contrast the results shown in Fig. IV 3 with the spectra expected in an isotropic medium. There Krishnan's reciprocity relation $I_{VH} = I_{HV}$ should hold⁽³⁴⁾ and only the longitudinal mode should give a component to the VV spectrum.

Acoustic Mode Velocities

We denote the acoustic modes for \hat{q} in the (010) plane as follows: L and T1 refer to the (mixed) quasi-longitudinal and quasi-transverse modes respectively polarized in the plane and T2 refers to the pure shear mode polarized perpendicular to the plane. In this notation we have that L and T1 gives components in VV spectra and T2 gives a component in HV and/or VH spectra.

We took spectra at various \vec{q} directions in the (010) plane in order to explore the angular dependence of the intensity and frequency shifts. This was easily done for VV scattering because the crystal was index matched to the oil bath so that rotating the crystal was equivalent to rotating the direction of \vec{q} keeping its magnitude fixed.

Fig. IV 3 Polarized Brillouin spectra in TGS. $\theta = 90^\circ$ and $\phi(q) = -45^\circ$.



The spectral data obtained from the direction scans has been reduced to the plots of peak signal intensity, intensity ratio and velocity for the L and T1 modes in Figs. IV 4-7.

The spectra were not actually VV spectra as they should have been. Instead they were made with vertically polarized incident light and no analyzing polarizer in the scattered beam. Thus the intensities represent the sum $VV + VH = VT$ (T for Total). The spectra were taken in this way under the naive impression from the spectra at $\phi(q) = -45^\circ$ that VH spectra had no components so that VT would be equivalent to VV. This is not true so the transverse component intensity and velocity data are somewhat distorted. This distortion is most serious when the intensity of the T1 component gets small and when the T1 and T2 modes are degenerate. The intensity of the VV scattering from the T1 mode is quite low for $\phi(q)$ from -15° to $+5^\circ$ and from 55° to 95° so the velocity curve for this mode isn't completely measurable with our arrangement. In Fig. IV 7 we have only given v_{T1} vs. $\phi(q)$ for angles where the transverse component in the spectrum is believed to be due essentially to the T1 mode.

We will now compare the observed velocity pattern in the (010) plane with the calculated velocities of Table II 1. We have converted the angles giving the \hat{q} direction to $\theta(q)$, where $\theta(q) = 15^\circ - \phi(q)$, to correspond to the coordinates of the elastic constants. $\theta(q)$ gives the angle between \hat{q} and the z axis.

In Fig. IV 8 we have plotted the observed and calculated room temperature velocities for the L mode. The agreement is poor except for the angles $\theta(q) = 0^\circ$ and 90° . Figure IV 9 shows the observed and calculated T1 mode velocities. Here the agreement is even worse but

**Fig. IV 4 L(quasi-longitudinal) and TI (quasi-transverse) mode
Brillouin component intensities versus \hat{q} direction
from VT spectra. (Laser approximately 60 mW).**

(010) PLANE
VT SPECTRA PEAK INTENSITIES

$\theta = 90^\circ$
 $T = 49.2^\circ\text{C}$

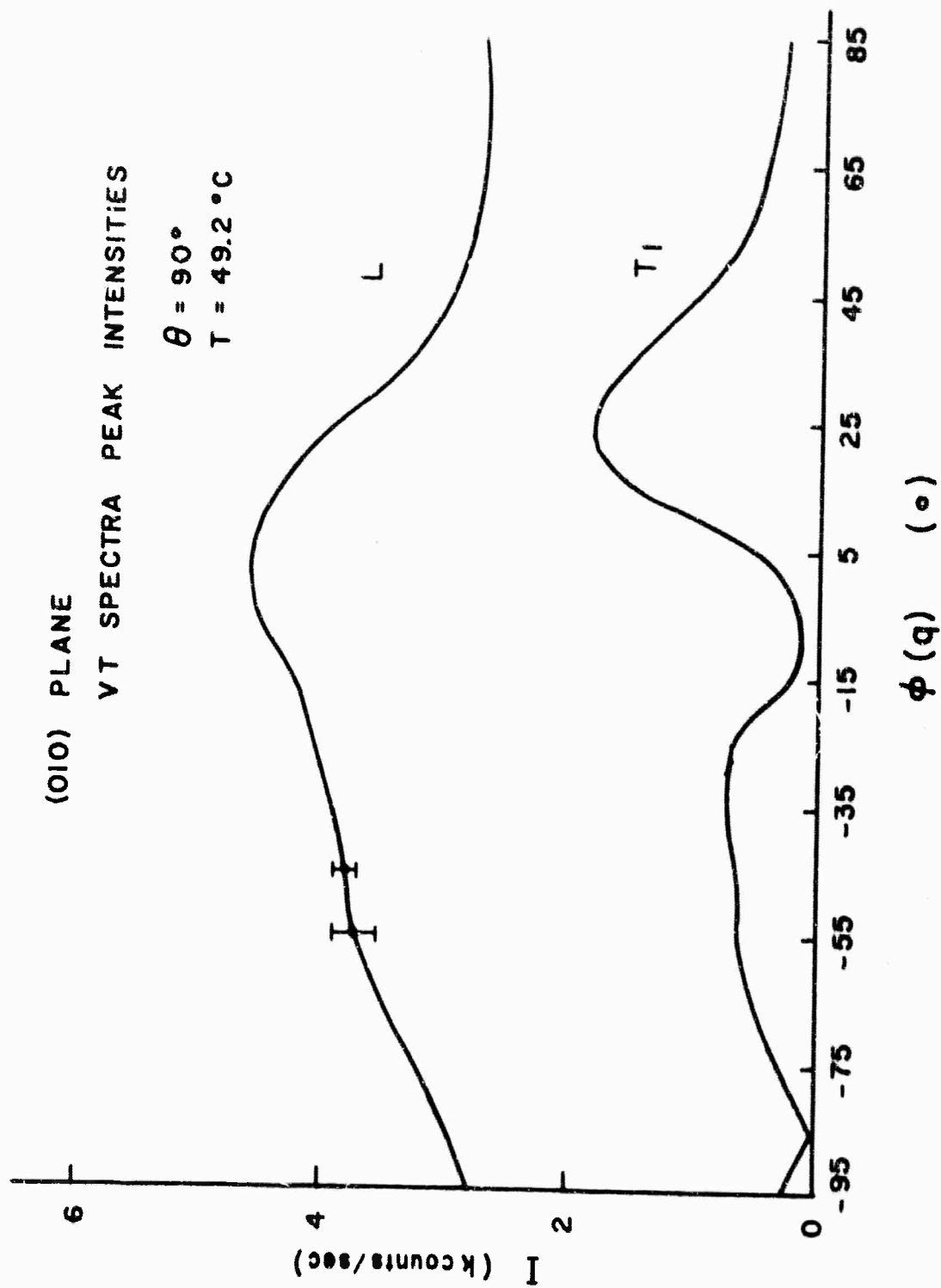


Fig. IV 5 Ratio of Brillouin component (peak) intensities for the L and T1 modes from the data of Fig. IV 4. Points labeled VV were checks to show that no VH scattering from the T2 mode was present at the angles indicated.

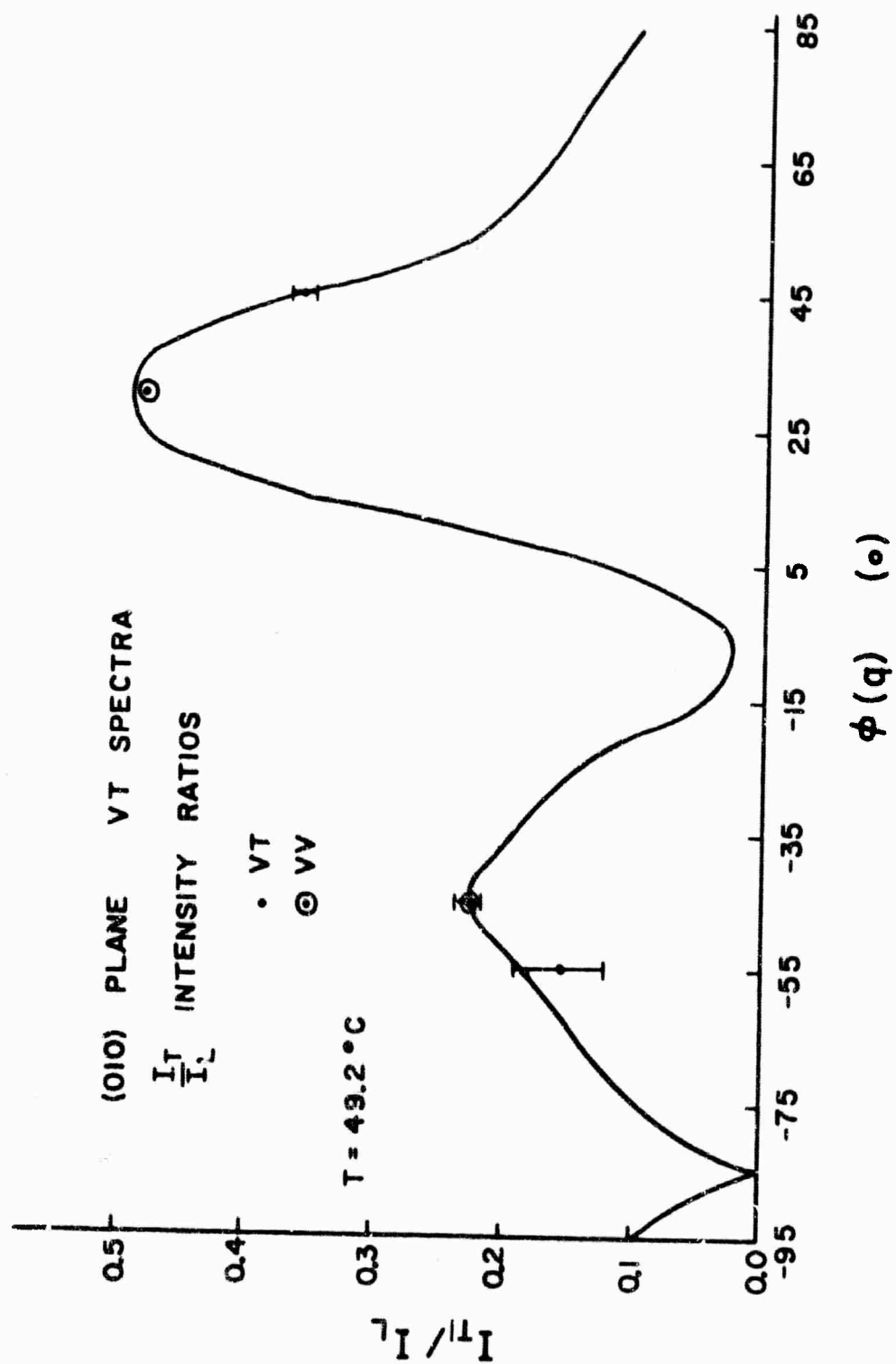


Fig. IV 6 L mode (quasi-longitudinal) velocities in the (010) plane of TGS. \hat{q} direction is given by the angle $\phi(q)$, measured from the c^* axis. Uncertainty is about $\pm 1\%$ in velocity and $\pm 1^\circ$ in $\phi(q)$. For reference a 2% ($\pm 1\%$) error bar is shown.

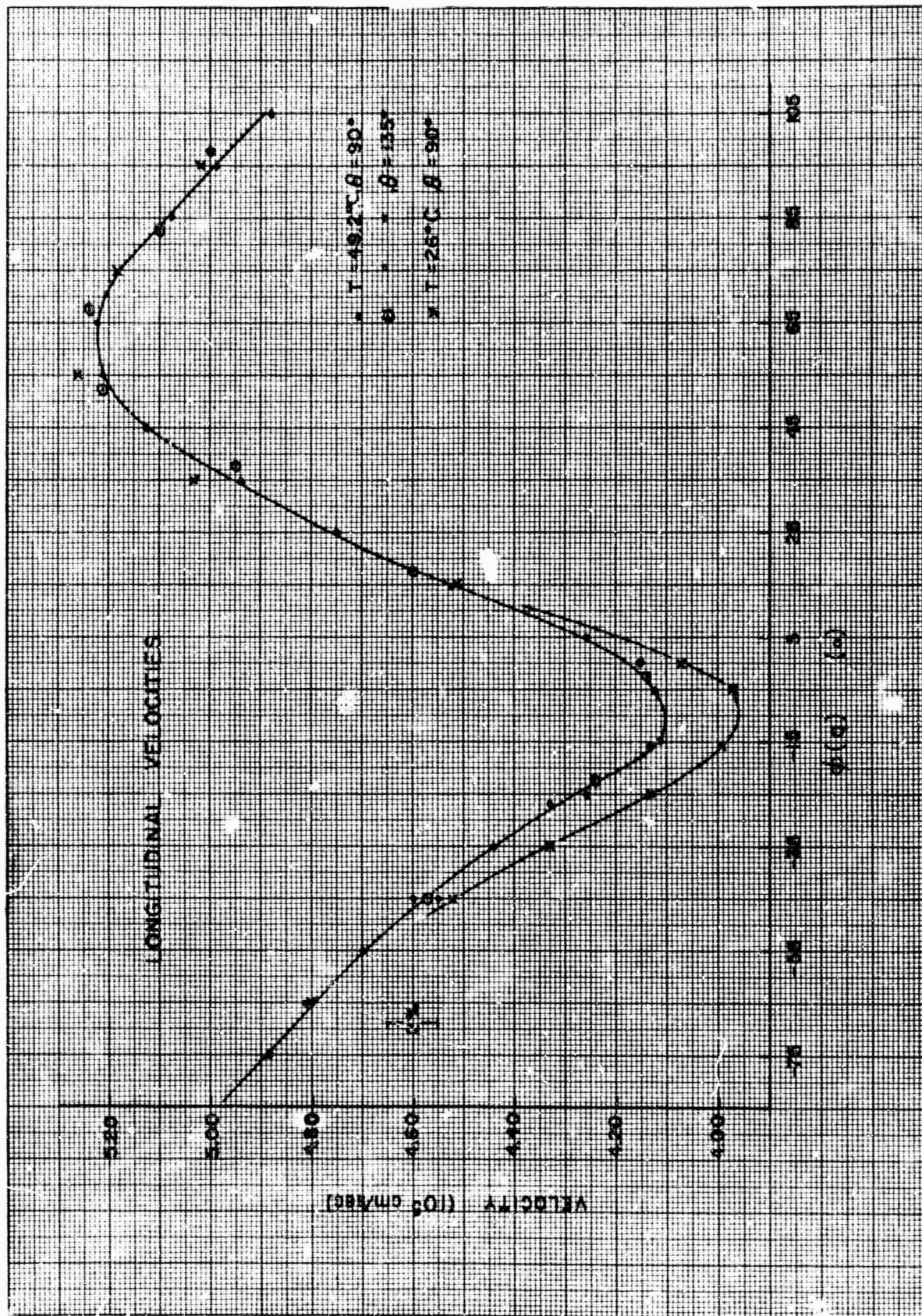


Fig. IV 7 T1 mode (quasi-transverse) velocities in the (010) plane of TGS. \hat{q} direction is given by the angle $\phi(q)$, measured from the c^* axis. Uncertainty is about $\pm 2\%$ in velocity and $\pm 1^\circ$ in $\phi(q)$. For reference a 4% ($\pm 2\%$) error bar is shown.

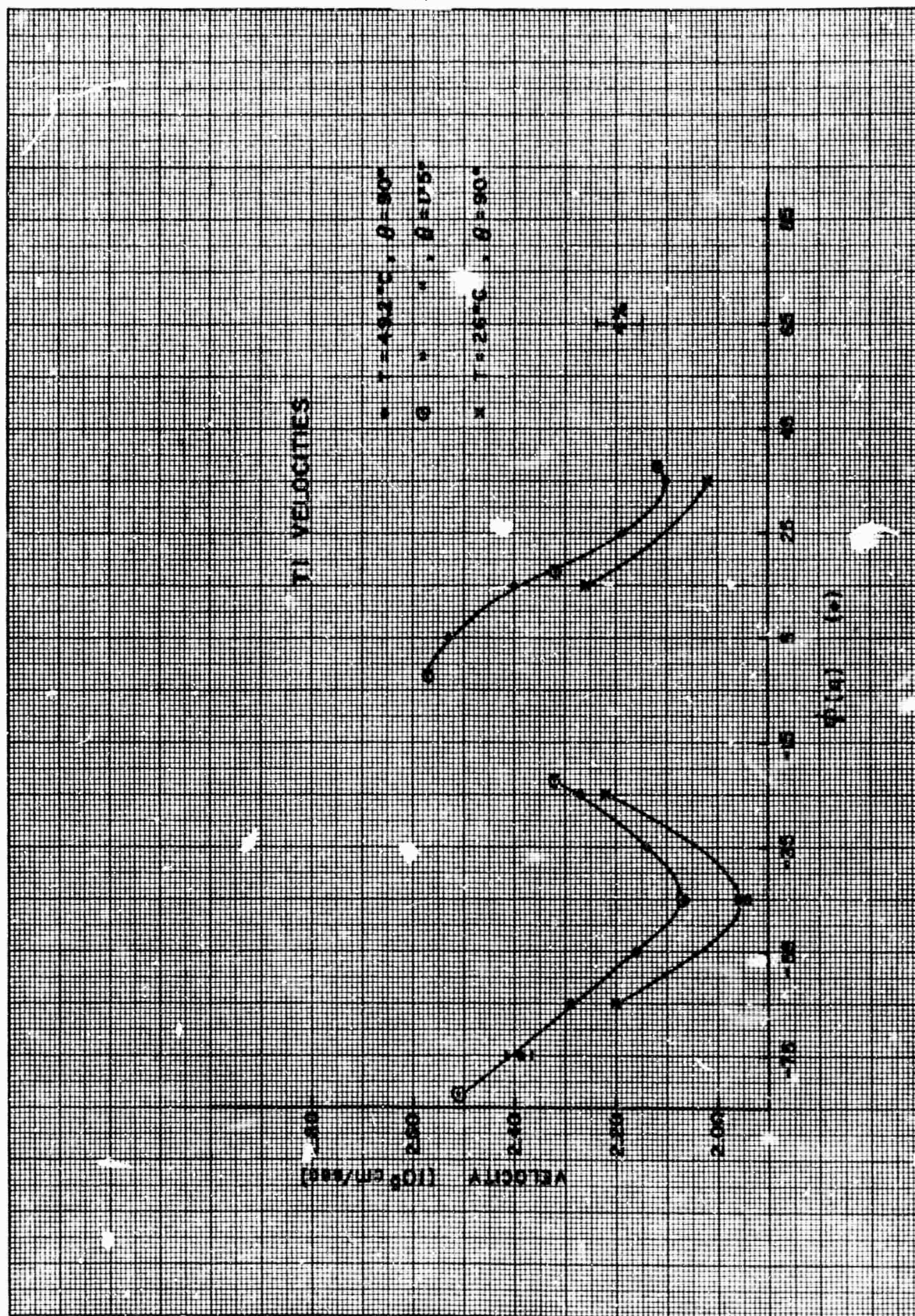


Fig. IV 8 L mode velocities: observed and calculated.

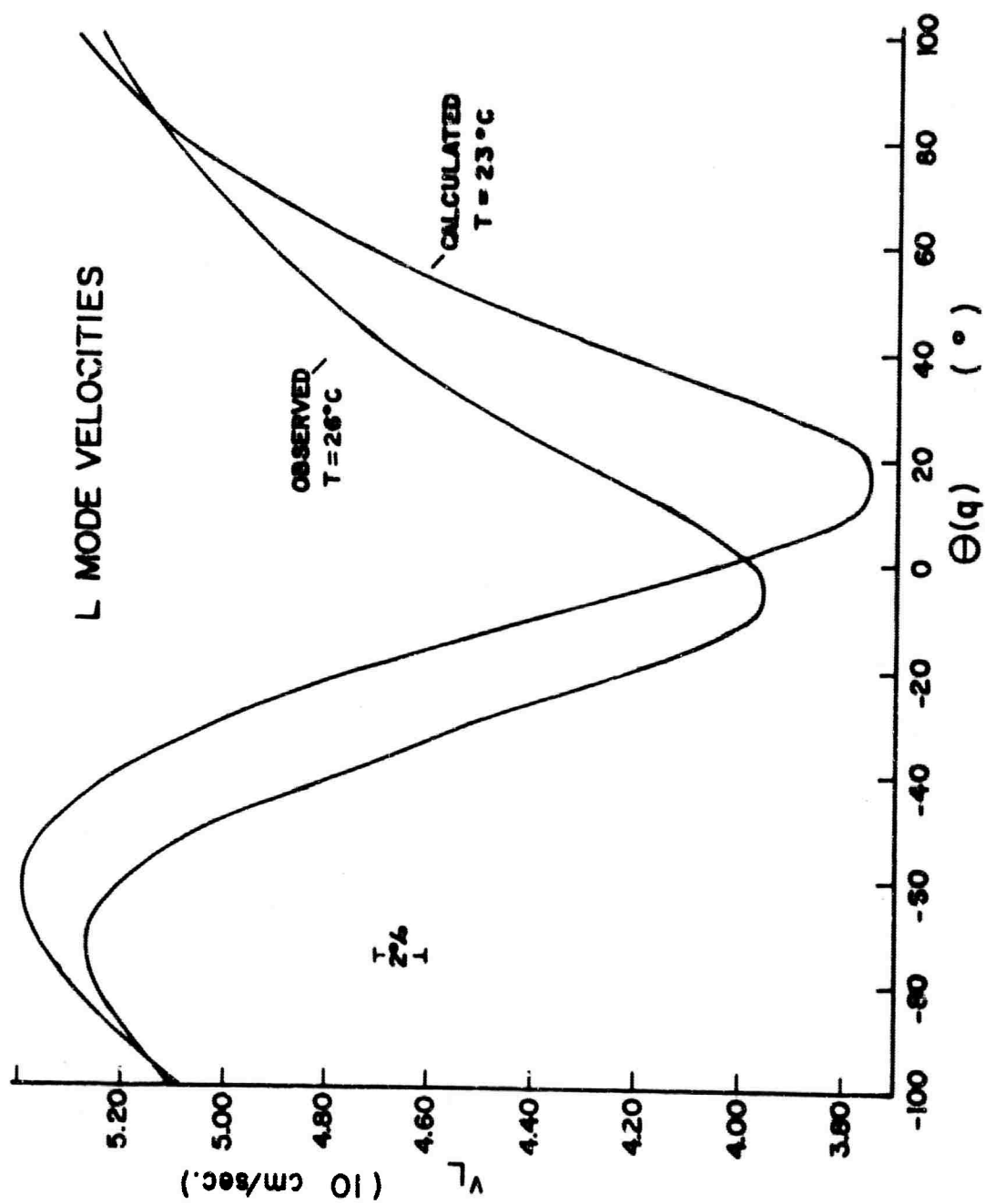
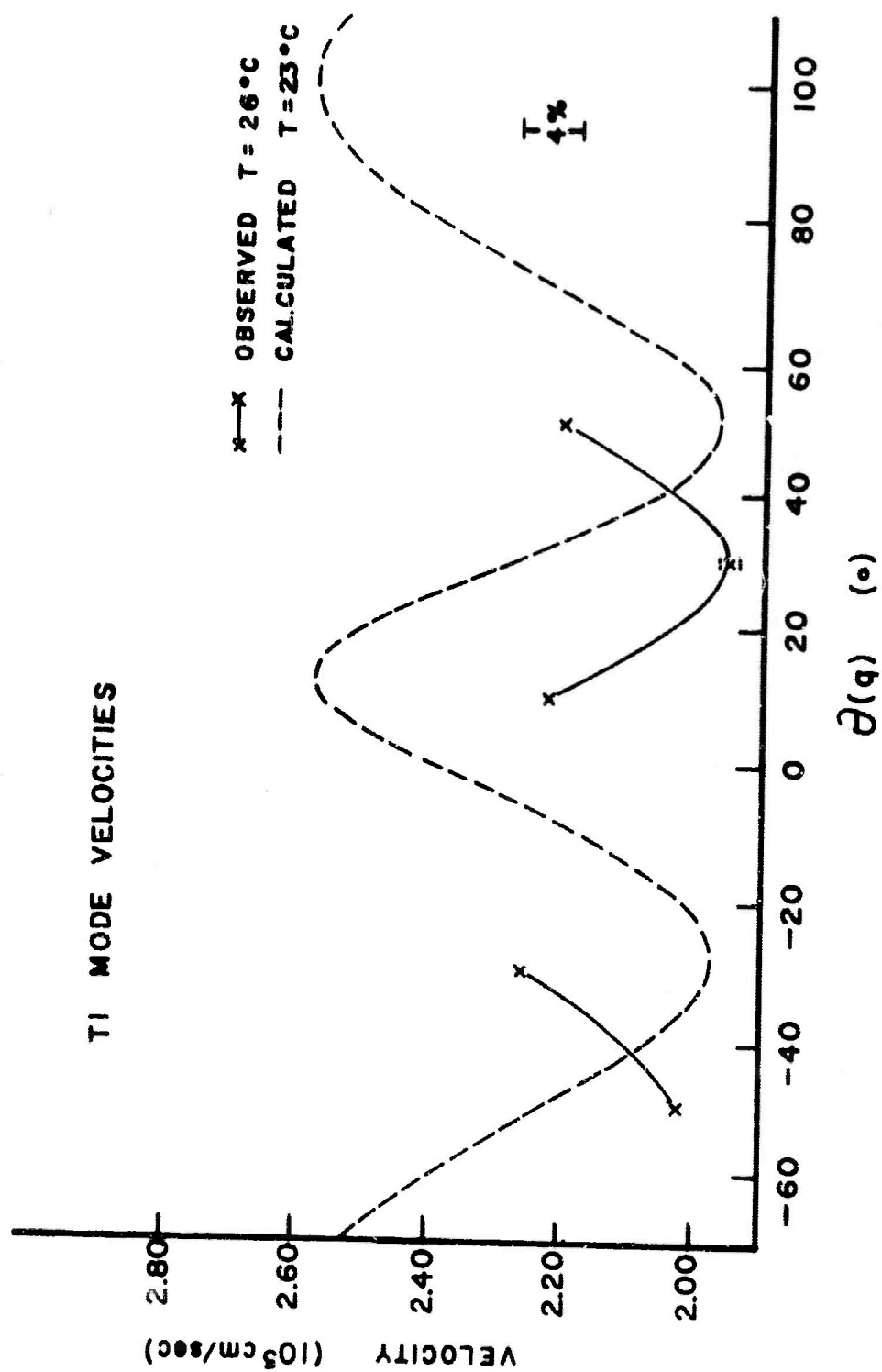


Fig. IV 9 T1 mode velocities: observed and calculated.



we seem to get crossings of the curves at $\theta(q) = 0^\circ$, 90° , and $\pm 45^\circ$. The differences in the observed and calculated velocities are well outside the uncertainties quoted for the elastic constants.

The ultrasonic velocity measurements were made at 0° , 90° , and one other angle ($\pm 45^\circ$?). We find agreement at 0° and 90° as expected assuming that the light scattering and ultrasonic measurements were done correctly. The disagreement at other angles indicates that some of the off-diagonal elastic constants c_{13} , c_{15} , and/or c_{35} were incorrectly measured or reported in the literature.

The L and T1 mode velocity data are tabulated in Table IV 2. We found the velocity data to be completely repeatable from sample to sample (five samples) and with different scattering angles within the uncertainty in setting the angles and extremely repeatable for a given sample when the temperature was cycled. There was no sign of sample dependence of the velocities as was reported in the ultrasonic work.

Several more comparisons of calculation with experiment to be presented in this paper are based on the ultrasonic elastic constants. We must here note that these calculations are probably in error and should be repeated with corrected elastic constants.

Figure IV 10 shows the calculated T2 mode velocities superimposed on the few accurate T2 velocity observations from HV spectra. The agreement at room temperature is fairly good (less than 4% difference at most). These measurements were made with crystals having faces cut normal to the incident and scattering directions so that the index mismatch between the oil in the bath and the index of the crystal for

TABLE IV 2

(010) PLANE OBSERVED VELOCITIES^(a)

$\theta(q)^{(b)}$	VELOCITY		(10^5 cm/sec.)	
	$T = 49.2^\circ\text{C}$		$T = 26^\circ\text{C}$	
	L	Tl	L	Tl
90	5.18			
80	5.08			
70	4.89		5.02	
60	4.88	2.39		
50	4.80	2.29	4.80	2.20
40	4.70	2.16		
30	4.57	2.06	4.52	1.95
20	4.33	2.14		
10	4.26	2.27	4.13	2.22
0	4.11			
- 10	4.12		3.97	
- 20	4.26	2.53		
- 30	4.52	2.40	4.51	2.26
- 40	4.747	2.19		
- 50	4.94	2.10	5.03	2.02
- 60	5.13			
- 70	5.21		5.26	
- 80	5.22			
- 90	5.18		5.17	

(a) $\theta = 90^\circ$, $\frac{q}{2\pi} = 3.317 \times 10^4 \text{ cm}^{-1}$ (b) $\theta = \theta(q)$ in xyz = $-a^*bc$ coordinate system. $-\theta(q) = 15^\circ + \phi(q)$

TABLE IV 2 (Continued)

(010) PLANE OBSERVED VELOCITIES ^(b)

T = 49.3°C

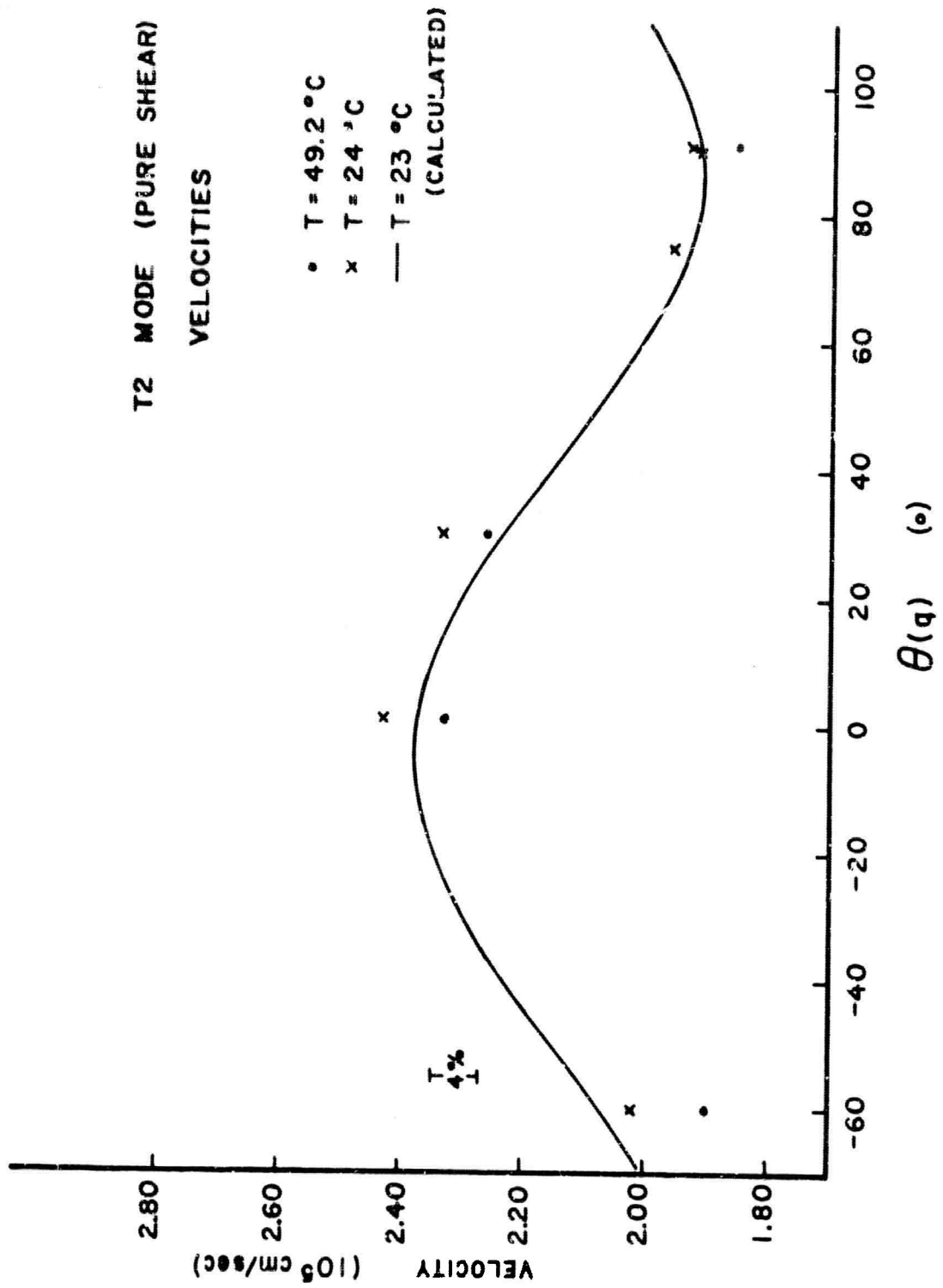
$\theta(q)$	VELOCITY		(10 ⁵ cm/sec.)
	L	Tl	
97.5	5.21		
82.5	5.10		
67.5	5.00	2.51	
30.0	4.57	2.08	
7.5	4.24	2.32	
- 12.5	4.14	2.57	
- 32.5	4.60	2.32	
- 52.5	4.95	2.12	
- 67.5	5.21		
- 82.5	5.24		

(b) $\theta = 135^\circ$

$$\frac{q}{2\pi} = 4.335 \times 10^4 \text{ cm}^{-1}$$

Fig. IV 10 T2 mode (pure shear) velocities: observed and calculated.

T2 MODE (PURE SHEAR) VELOCITIES



light polarized in the (010) plane could not cause the beams to be deflected. To get data points with $\theta(q)$ near 90° required cutting faces at 45° to the c face. Autocollimation off the c face became difficult so the direction of \vec{q} in the crystal is less certain in this data than in the VV scattering.

Spectra were taken for \vec{q} parallel to \vec{b} with a scattering angle of 135° . These spectra showed only a longitudinal component. This mode is a pure longitudinal mode. The observed Brillouin shift indicates that the velocity is 4.39×10^5 cm/sec. at 49.2°C and from the measured temperature coefficient of -1.7×10^2 cm/sec. $^\circ\text{C}$ we calculate an extrapolated velocity at 23°C of 4.43×10^5 cm/sec. Due to the refractive index mismatch for this crystal orientation we expect the scattering angle inside the crystal to be increased causing a 1% increase in q . This correction was applied to the above velocities. Again we are within 2% of the velocity calculated from the ultrasonic elastic constants (4.36×10^5 cm/sec. at 23°C) but from the uncertainties given with the ultrasonic data we should be even closer.

Pockels Coefficients

The spectra giving the intensity data for Figs. IV 4 and IV 5 were taken with the crystal at 49.2°C . Spectra taken at room temperature give essentially the same ratios.

In order to reduce the intensity data to relations among the Pockels coefficients one should reduce the velocity data to a set of elastic constants, then compute the phonon polarizations (eigenvector problem) and finally compute the strain $(qu)_\rho$. This is a second rank tensor or in matrix notation with reduced subscripts a six component vector.

It was hoped that the observed velocities would agree well enough with the velocities computed from the ultrasonic elastic constants that one could use the phonon polarization vectors from that calculation to compute the strains produced by the mixed modes. As we have already seen there is substantial disagreement in the velocities so that to use the calculated phonon polarizations to derive consistent Pockels coefficients is questionable.

We will carry the intensity calculation a little further to make some semi-quantitative statements. We showed in Section II that $\Delta\epsilon_{22}$ which describes VV scattering for the (010) plane is given by

$$\Delta\epsilon_{22} = -\epsilon_2^2 (p_{21}^2 \alpha + p_{23} n\gamma + p_{25} (1\gamma + n\alpha)) qu$$

where $q = (1, 0, n)$ and $u = (\alpha, \beta, \gamma)$

This result is found by computing the strain

$$(\vec{q}\vec{u})_p = [1\alpha, 0, n\gamma, n\alpha, 1\gamma + n\alpha, 1\beta] qu$$

(in matrix notation) and multiplying it into the photoelastic matrix

$$\left(\frac{\partial \epsilon_{ij}}{\partial x_{kl}} \right)_{\rho\sigma} = -(\epsilon_i \epsilon_j p_{ijkl})_{\rho\sigma} .$$

p_{21} , p_{23} and p_{25} are the only allowed coefficients in the present case.

We will discuss our Brillouin component intensity observations in the orthogonal coordinate system $x'yz' = abc^*$ but will omit the primes on the subscripts.

The scattering intensity from the quasi-longitudinal mode does not depend strongly on the mixed character of the mode so we have attempted to fit the intensity data for this with the expression for a pure longitudinal mode

$$\Delta\epsilon_{22} = -\epsilon_2^2 (p_{21} l^2 + p_{23} n^2 + 2p_{25} nl) qu .$$

Then we expect the ratio of scattering intensity for q at 0° and 90° to be

$$\frac{I_L^{(0)}}{I_L^{(90)}} = \left(\frac{p_{21}}{p_{23}} \right)^2 \frac{v_L^{(90)^2}}{v_L^{(0)^2}} .$$

Performing this calculation on our data gives the result

$$\left(\frac{p_{21}}{p_{23}} \right)^2 = 1.1 \pm 10\% .$$

Since the L intensity shows no zeroes or strong minima we expect p_{21} and p_{23} to have the same sign and so we find that p_{21} and p_{23} are approximately equal. The mixed character of the L mode makes only a 4% effect on the ratio of the p 's according to the calculation of Table II 1. Comparing the velocities in Fig. IV 6 to the L intensities in Fig. IV 4 shows that the intensity is approximately proportional to

v^{-2} for all \hat{q} in the plane. From this we conclude that $p_{25} \ll p_{23}$.

If $p_{12} \approx p_{23}$ then we can write

$$\Delta\epsilon_{22}(T1) = -\epsilon_2^2 (p_{23} \vec{q} \cdot \vec{u}_{T1} + p_{25} \cos 2\phi(q)) q u.$$

Thus near $\phi(q) = \pm 45^\circ$, where the second term is very small, the scattering is proportional to $(\vec{q} \cdot \vec{u}_{T1})^2$. This quantity is a measure of the mixed character of the T1 mode. It would be zero for a pure transverse mode.

Comparing the $\vec{q} \cdot \vec{u}_{T1}$ column of Table II 1 with the T1 intensity data of Fig. IV 4 shows poor agreement but since the calculated velocities do not agree with observation this is not surprising.

We expect that the lowest values of the T1 mode velocity correspond to the \hat{q} directions having the greatest mode mixing. We see that these directions also correspond to maximum T1 intensity in agreement with the prediction that $\Delta\epsilon_{22}^2$ is proportional to $(\vec{q} \cdot \vec{u}_{T1})^2$.

This particular comparison to the intensity data is not hindered by the VH scattering in the VT data of Figs. IV 4 and IV 5 as shown by the circled points of Fig. IV 5 which represent intensity ratios taken from VV spectra.

A systematic study of the HV scattering intensity in the (010) plane was not made but we can say something about the Pockels coefficients. The expression for the dielectric fluctuation probed in

HV or VH scattering is much more complicated than that for VV scattering. This is because for a general \hat{q} direction the scattering amplitude comes from a linear combination of $\Delta\epsilon_{21}$ and $\Delta\epsilon_{23}$.

For $q = (l, 0, n)$ we have

$$x = [0, 0, 0, n, 0, l] qu$$

since $u = (0, 1, 0)$ for the T2 mode. To treat the case of a 90° scattering angle we take

$$E_s = \frac{1}{\sqrt{2}} [(l+n), 0, (n-l)] \quad E_o = (0, 1, 0)$$

for VH scattering and

$$E_s = (0, 1, 0) \quad E_o = \frac{1}{\sqrt{2}} [(l-n), 0, (n+l)]$$

for HV scattering. In this case the dielectric fluctuation amplitude is

$$\begin{aligned} \Delta\epsilon_{VH} &= - \frac{\epsilon_o \epsilon_b}{\sqrt{2}} [\Delta\epsilon_{21}(l \pm n) + \Delta\epsilon_{23}(n \mp l)] qu \\ &= - \frac{\epsilon_o \epsilon_b}{\sqrt{2}} [(p_{44} \pm p_{64}) n^2 + (p_{66} \mp p_{46}) l^2 \\ &\quad + \{(p_{64} + p_{46}) \pm p_{66} \mp p_{44}\} nl] qu \end{aligned}$$

with + sign for VH and - sign for HV. Table IV 3 gives $\Delta\epsilon$ for HV and VH for special directions.

TABLE IV 3

HV, VH SCATTERING AMPLITUDES

θ	POLARIZATION	$-\Delta \epsilon$
0	VH HV	$\frac{\epsilon_o \epsilon_b}{\sqrt{2}} (p_{44} \pm p_{65}) q u$
90°	VH HV	$\frac{\epsilon_o \epsilon_b}{\sqrt{2}} (p_{66} \mp p_{46}) q u$
$+45^\circ$	HV	$\frac{\epsilon_o \epsilon_b}{\sqrt{2}} (p_{66} + p_{64}) q u$
$+45^\circ$	HV	$\frac{\epsilon_o \epsilon_b}{\sqrt{2}} (p_{44} - p_{46}) q u$
-45°	VH	$\frac{\epsilon_o \epsilon_b}{\sqrt{2}} (p_{44} + p_{46}) q u$
-45°	HV	$\frac{\epsilon_o \epsilon_b}{\sqrt{2}} (p_{66} - p_{64}) q u$

We found the ratio of the HV intensity at $\phi(q) = -45^\circ$ to the VH intensity at $\phi(q) = +45^\circ$ to be .76 which is just equal to the inverse of the ratio of squared velocities at those angles. Therefore we conclude that p_{66} is much greater than p_{64} . We found VH to be 3.3 stronger than HV at $\phi(q) = +45^\circ$ while there was no detectable VH scattering at $\phi(q) = -45^\circ$. From this we conclude that $p_{44} = -p_{46}$ and $(2p_{44})/p_{66} = .56$.

Finally, from the ratio of an HV component to the VV longitudinal component at $\phi(q) = -45^\circ$ we have

$$\left| \frac{p_{66}}{p_{23}} \right| = .28 .$$

The scattering intensity from the longitudinal mode with \vec{q} parallel to \vec{b} was found to be the same as that for $\theta(q) = -45^\circ$ scattering from the L mode (within 3%) both for yz and for xy plane scattering spectra. Therefore $p_{12} = p_{32}$ and

$$\left| \frac{p_{12}}{p_{23}} \right| = .60 .$$

In order to determine the Brillouin scattering cross sections and Pockels coefficients in TGS we ran consecutive VV spectra on samples of water, fused quartz, and TGS ($\phi(q)$ at -45°). By comparing the signal heights of the longitudinal components in these materials we can determine the cross section in TGS because the cross sections in water and fused quartz are known in the sense that they can be calculated. The cross section per unit volume (denoted s) is

$$\frac{ds_{VV}}{d\Omega} = \pi^2 \left(\frac{1}{\lambda}\right)^4 kT \frac{(\epsilon-1)^2}{\rho v^2}$$

for H_2O and

$$\frac{ds_{VV}}{d\Omega} = \pi^2 \left(\frac{1}{\lambda}\right)^4 kT \frac{(\epsilon^2 p_{12})^2}{\rho v_L^2}$$

for fused quartz. These cross sections give the total scattering intensity for scattering from the longitudinal modes in the doublet with components at $\Delta\omega = \pm\omega(q)$. The cross section for a single Brillouin component would be half as large.

The data is given in Table IV 4 as the maximum signal for the longitudinal components, the signal ratios, and signal ratios corrected for differing collection angles. From these ratios we computed the scattering cross sections from the calculated cross section for water at $23^\circ C$ and $\lambda = 6328 \text{ \AA}$

$$\frac{ds_{VV}}{d\Omega} = .683 \times 10^{-6} \text{ cm}^{-1} \text{ (i. e. cm}^2/\text{cc)}$$

They also are listed in Table IV 4.

For comparison we can calculate the cross section for fused quartz directly from measured values of p_{12} . Vedam⁽³⁵⁾ gives $p_{12} = .285$ and Primak and Post⁽³⁶⁾ give .270. Taking these values to represent the uncertainty

TABLE IV 4

BRILLOUIN SCATTERING CROSS SECTIONS

Sample	Peak Signal (k count/sec.)	Ratio ^(a) to H ₂ O	$\frac{ds_{vv}}{d\Omega}$ (cm ⁻¹)
H ₂ O	32.	1.00	.683 x 10 ⁻⁶
Fused Quartz	1.86	7.5x10 ⁻²	5.3 x 10 ⁻⁸
TGS	3.3	13.0x10 ⁻²	9.2 x 10 ⁻⁸

^a Corrected by ratio of squared refractive indices to account for different collection solid angles.

^b $\frac{ds_{vv}}{d\Omega}$ is the differential cross section per unit volume for VV scattering. The units are cm²/cc = cm⁻¹.

in our knowledge of p_{12} we take a value of $p_{12} = .278 \pm 3\%$. Then for the same temperature and wavelength we find

for fused quartz

$$\frac{ds_{VV}}{d\Omega} = (5.0 \pm 3\%) \times 10^{-8} \text{ cm}^{-1}$$

This is in reasonable agreement with the cross section for quartz calculated from the observed intensity ratios.

Given the densities, longitudinal velocities, and refractive indices of fused quartz and TGS we can extract the ratio p_{23} of TGS to p_{12} of fused quartz. The cross section formulas and the relations among Pockels coefficients found in TGS show that the intensity ratio satisfies

$$\frac{I_{TGS}}{I_{FQ}} = \frac{(\epsilon_b^2 p_{23})_{TGS}^2}{(\epsilon_b^2 p_{12})_{FQ}^2} \frac{(\rho v_L^2)_{FQ}}{(\rho v_L^2)_{TGS}}$$

Taking for fused quartz $\rho v^2 = .78 \times 10^{12} \text{ dyne/cm}^2$ and $n = 1.458$ and for TGS $2v^2 = .357 \times 10^{12} \text{ dyne/cm}^2$ and $n = 1.484$ we find

$$p_{23} (TGS) / p_{12} (FQ) = .95.$$

Taking $p_{12} (FQ) = .278$ gives $p_{23} (TGS) = .26(4)$. We can now evaluate the remaining Pockels coefficients that were involved in the

experiments. They are collected in matrix form in Table IV 5 with their most probable signs. In most cases the signs are not determined by the intensity comparisons.

Finally, with this data we can give two numerical examples which justify the comment made at the end of Section I which said in effect that

$$\epsilon^2 p_{12} \approx \epsilon - 1.$$

This is a very useful relation for predicting approximate scattering intensities.

For fused quartz we find $\epsilon - 1 = 1.27$ and $\epsilon^2 p_{12} = 1.26 \pm 3\%$.

For TGS (010) plane scattering we find $\epsilon_b - 1 = 1.20 \approx \epsilon_b^2 p_{23} \approx 1.28$.

One further observation about TGS as a light scattering sample should be mentioned. In 6328 \AA light the crystal produces a strong background of inelastically "scattered" light. This background can be blocked with an 18 \AA width interference filter, hence must come from $> \pm 22 \text{ cm}^{-1}$ away from the center frequency. It could be a strong Raman effect or more likely it is fluorescence. When a TGS crystal was placed in an Argon laser beam (4880 \AA) we saw a light path in the crystal illuminated by depolarized weak yellow fluorescence.

Sample Preparation

The TGS samples used in this work were grown from solution by slowly lowering the well regulated temperature of the solution at a constant rate. The apparatus and technique were essentially the same

TABLE IV 5

TGS POCKELS COEFFICIENTS^(a)

$$p_{ij} = \begin{bmatrix} \bullet & 16. & \bullet & . & \bullet & . \\ 27. & \bullet & 27. & . & 0. & . \\ \bullet & 16. & \bullet & . & \bullet & . \\ . & . & . & 2.1 & . & -2.1 \\ \bullet & \bullet & \bullet & . & \bullet & . \\ . & . & . & 0. & . & 7.6 \end{bmatrix} \times 10^{-2}$$

- Allowed but not measured
- . Zero by symmetry

(a) $x'y'z' = abc^*$ coordinate system.

as those used at the National Bureau of Standards⁽³⁷⁾ in growing ammonium dihydrogen phosphate crystals. The raw TGS was produced by Eastman Organic Chemicals. We dissolved this in distilled water to form a saturated solution at 44°C. This solution was then passed through a 1.0 micron pore diameter Millipore filter up to three times. In this way we obtained a dust free solution which produced crystals substantially free from inclusions, as shown by direct visual examination using laser illumination and by the low extraneous elastic scattering in the light scattering spectra.

Reference (38) gives two articles on growing TGS.

The samples of TGS used for light scattering were prepared from large (2 x 2 x 4 cm) crystals by cleaving the crystals perpendicular to b making roughly 6 mm thick (010) cut plates. The large natural c faces were left intact to serve as orientation references.

Electrodes were painted on the (010) faces to allow the application of large dc electric fields parallel to the b axis. For the work in this section the application of fields was only to assure that the crystal was single domain in the ferroelectric phase. This will be discussed more fully in Section V.

The sample was mounted on lucite support rod. This rod held the sample suspended in the oil bath used to control the sample temperature and provide the refractive index match. The rod was mounted vertically in a device (a "twiddler") which allowed screw adjusted measured rotation of the rod and sample about the rod axis which was verticle and perpendicular to the scattering plane.

LIGHT SCATTERING IN TGS NEAR ITS FERROELECTRIC PHASE
TRANSITION

The goal in our light scattering experiments in TGS was to study the dynamics of thermodynamic fluctuations in the region of a second order phase transition in a crystal.

After a short description of the relevant properties of TGS we will present the results of Brillouin scattering experiments in TGS near the Curie temperature. These experiments basically consisted of measuring the Brillouin shift and linewidth as a function of temperature and applied field for the various acoustic modes. We found that certain of the modes showed a q dependent velocity dispersion with temperature and field. The data was found to fit single relaxation time predictions of velocity dispersion. The related damping of the modes was seen as a broadening of the Brillouin components in the dispersion region. We were able to extract the temperature and field dependent relaxation rates from the data.

We believe that the observed relaxational effects are due to the large and slow fluctuations near T_C of the electric polarization parallel to the ferroelectric axis. The data is presented in this section without such an interpretation in order to separate the experimental facts from theory. In Section VI we will give the phenomenological theory which ties together the observations of the present section and the ferroelectric phase transition. The reader unfamiliar with ferroelectrics and second order phase transitions may wish to go directly to Section VI before studying the experimental results.

No critical opalescence was observed though it was searched for indicating that the fluctuations in the order parameter near T_C are not strongly coupled to the optical dielectric constant.

Triglycine Sulfate

Triglycine sulfate (TGS) is a colorless monoclinic crystalline solid. The molecular formula is $(\text{NH}_2\text{CH}_2\text{COOH})_3\text{H}_2\text{SO}_4$ and there are two formula units per unit cell. This crystal was found to be ferroelectric at room temperature and undergo a phase change to a non-polar phase at 47°C by Matthias et. al.⁽³⁹⁾ X-ray studies by Wood and Holden⁽⁴⁰⁾ showed that the polar phase had the point symmetry C_2 . Further x-ray studies by Hoshino et. al.⁽⁴¹⁾ showed that non-polar phase had an average symmetry C_2/m . In the polar phase the monoclinic (b) axis is the ferroelectric axis as is required by symmetry.

The phase transition in TGS is marked by Curie law behavior of the dielectric constant, that is ϵ_b is found to be proportional to $|T - T_C|^{-1}$ near T_C .⁽⁴²⁾ The phase transition temperature and the Curie temperature are taken to be the same close to the transition.

We describe a ferroelectric crystal for the present as a polar class crystal exhibiting a pyroelectric polarization (i. e. a temperature dependent electric polarization occurring spontaneously without an external electric field) which can be reversed by an applied electric field. In analogy to a ferromagnet, a ferroelectric crystal shows P vs. E hysteresis loops for electric fields applied along the direction of spontaneous polarization. (\vec{P} is the electric polarization).

The crystal TGS microscopically has a very complex structure⁽⁴³⁾ and macroscopically it has low symmetry. Nevertheless TGS is a reasonable choice for a first Brillouin scattering study because its macroscopic thermodynamic properties show simple behavior, many of its properties have been measured, it has a well established second order (order-disorder) phase transition at an experimentally very convenient temperature, and it is easily grown in large optical quality crystals.

Previous investigations have shown that there are elastic anomalies near T_C in TGS. Gilletta⁽⁴⁴⁾ and Ikeda, et al.⁽⁴⁵⁾ studied the elastic compliances s_{ij} by resonance techniques and found certain of them to show large changes just below T_C . The work of Ikeda, et al. established that there was no change in the elastic properties at constant electric polarization (P) at the phase transition, but that electrostrictive coupling of polarization and elastic vibrations gave an anomaly in elastic properties when measured with constant electric field (E) boundary conditions. O'Brian and Litovitz⁽⁴⁶⁾ found velocity dispersion and frequency dependent attenuation below T_C for pulsed ultrasonic waves traveling perpendicular to the ferroelectric axis. They fit their observations to single relaxation time formulae and attributed the relaxation to the polarization along the ferroelectric axis. Based on these studies we expected to see the Brillouin components for scattering from suitable modes show a 1% to 10% frequency increase as T approached T_C from below.

Temperature Measurement and Control

The temperature of the crystal was controlled by regulating the temperature of the oil bath in which it was placed. The bath was cylindrical, 16 cm in diameter and 15 cm high. The oil was light paraffin oil which had been filtered through a 1μ Millipore filter. The temperature controller was a commercial proportional controller (Fisher Scientific Proportional Temperature Controller Cat. No. 150177-50V2) using a thermistor probe, an ac bridge and phase sensitive triggering of silicon control rectifiers. The heater was a 100 W copper enclosed coil. With a well stirred bath and careful probe placement it was possible to control the temperature to within $\pm .01\text{ }^{\circ}\text{C}$. The temperature was measured with a Brooklyn mercury thermometer (#22236) with a $(.01\text{ }^{\circ}\text{C})/\text{div.}$ scale for temperatures in the range 41°C to 55°C around T_C . This thermometer was calibrated for total immersion but was not used totally immersed so the absolute temperatures are not known to better than $\pm .03\text{ }^{\circ}\text{C}$. On the other hand temperature differences should be good to within the limit set by the control fluctuation of $\pm .02\text{ }^{\circ}\text{C}$.

Determining T_C

The review literature gives only the crude value of 49°C for the Curie temperature of TGS. A literature search shows that T_C has been found to occur over a range of 47°C to 50°C by different investigators studying different samples. Even the recent highly precise dielectric measurements of Craig⁽⁴⁷⁾ and Gonzalo⁽⁴⁸⁾ give T_C differing by $1\text{ }^{\circ}\text{C}$.

We wanted to eliminate the necessity of knowing our absolute

temperature while accurately knowing how far we were from T_C . This made it necessary to perform an independent experiment to find the temperature reading of our thermometer which corresponded to T_C in our samples.

Our test for T_C was to look for the temperature of the oil bath at which an immersed TGS sample stopped showing hysteresis in its P vs. E characteristic. Since P_g , the spontaneous polarization, goes continuously to zero as T approaches T_C from below and then remains constant at zero for T greater than T_C , the temperature at which the hysteresis loop first closes should be T_C .

The probes for this test were small capacitors made from the same batches of TGS to be used in the light scattering experiments. These capacitors were 1 mm thick cleaved b plates with b faces of about $.5 \text{ cm}^2$ area. The b faces were painted with silver conducting paint to form the capacitor electrodes.

These capacitor probes were submerged in the oil bath and connected into a simple version of a Sawyer-Tower⁽⁴⁹⁾ circuit which allowed a 60 Hz ac voltage of 45 V rms to be applied to the crystal electrodes (E up to 640 V/cm) while a signal proportional to the charge on the electrodes was displayed vs. the applied field on an oscilloscope. No special phase compensation was used so it was not possible to get the display on the oscilloscope to show a closed loop at T greater than T_C but by turning up the gain of the scope it was possible to magnify the temperature dependence of the tip of the loop. (The tip is the point of maximum induced polarization and applied field.) It was found that for thermometer readings greater than $49.25 \pm .01^\circ \text{C}$ the tip of the loop was independent of temperature. We found this same temperature for samples given

to us by T. A. Litovitz, for samples grown in our laboratory from pure baths and for a sample grown in our laboratory from an iron contaminated bath.

We defined this temperature reading as our reference TGS Curie temperature. All temperature differences to be given later in presenting the data were computed using this reference temperature reading of 49.25°C .

The absolute temperature of our T_C measurement was $49.23 \pm .03^{\circ}\text{C}$ taking the $-.07^{\circ}\text{C}$ zero correction supplied with the thermometer and an estimated stem correction of $+.05^{\circ}\text{C}$ into account.

Table V 1 gives a list of Curie temperatures observed by other workers along with the present determination. The most illuminating discussion of the variation of Curie temperatures due to holding the crystal at T greater than T_C , applied electric fields and doping is found in Stankowska and Stankowski.⁽⁵⁰⁾ They found T_C to be 49.2°C for multidomain pure crystals, 49.15°C for single domain pure crystals and depressed to 48.2°C for CuSO_4 doped crystals. Our temperature is in agreement with their results since the ac fields required to see the hysteresis loop cause the formation of antiparallel needle domains.⁽⁵¹⁾ It appears that crystal purity, defects, and mechanical and electrical clamping effects have caused different Curie temperatures in the various investigations.

Temperature Dependence of the Brillouin Shifts⁽⁵²⁾

Brillouin spectra were taken with the scattering plane parallel to the crystal (010) plane for q at -45° to c^* (i. e., $\phi(q) = -45^{\circ} = \theta(q) = +30^{\circ}$. See Appendix Fig. A 1.) at temperatures between room temperature and 55°C . A temperature dependent frequency dispersion

TABLE V 1

TGS CURIE TEMPERATURES

T_C (°C)	Reference
47	a
48	b
49.8	c
49.2 - 49.3	d
49.15- 49.2	e
49.2	f
49.1 - 49.6	g
48.3	h
49.09	i
48.478	j
49.42 ±.05	k
49.23±.03	l

- ^a Matthias et al. (1956) ⁽³⁹⁾
- ^b Hoshino, Mitsui, Jona and Pepinsky (1957) ⁽⁸³⁾
- ^c Triebwasser (1958) ⁽⁸⁴⁾
- ^d Konsantinova, Sil'vestrova and Aleksandrov (1960) ⁽⁸⁵⁾
- ^e Stankowska and Stankowski (1960) ⁽⁵⁰⁾
- ^f Shuvalov and Pluzhnikov (1962) ⁽⁸⁶⁾
- ^g Sil'vestrova (1962) ⁽⁸⁷⁾
- ^h Hill and Ichiki (1963) ⁽⁸⁸⁾
- ⁱ O'Brian and Litovitz (1964) ⁽⁴⁶⁾
- ^j Craig (1966) ⁽⁴⁷⁾
- ^k Gonzales (1966) ⁽⁴⁸⁾
- l The present work

for the quasi-longitudinal (L) and quasi-transverse (T1) modes was found to occur for temperatures in the range 46°C to T_C . This dispersion is shown for Brillouin scattering shifts from spectra taken at scattering angles of 90° and 135° in Fig. V 1.

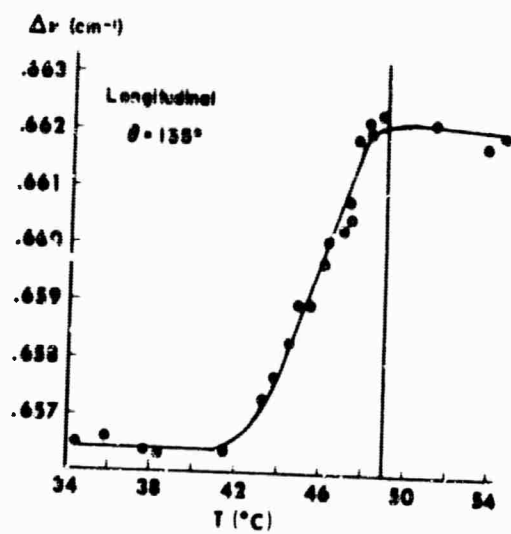
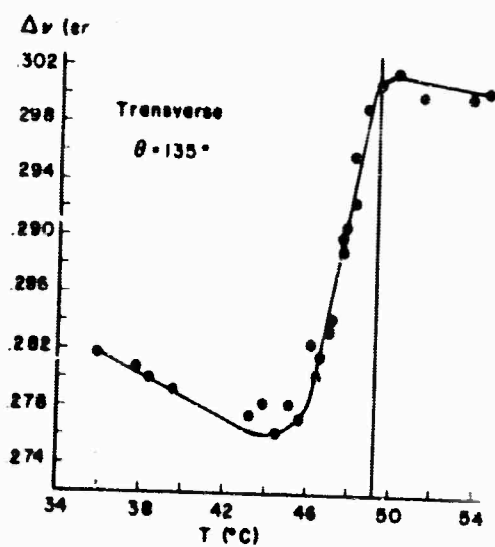
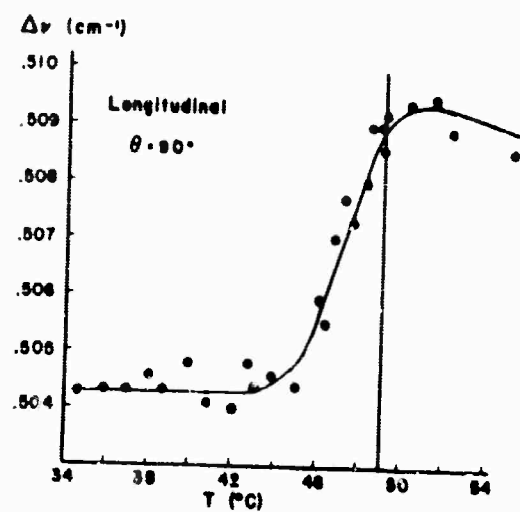
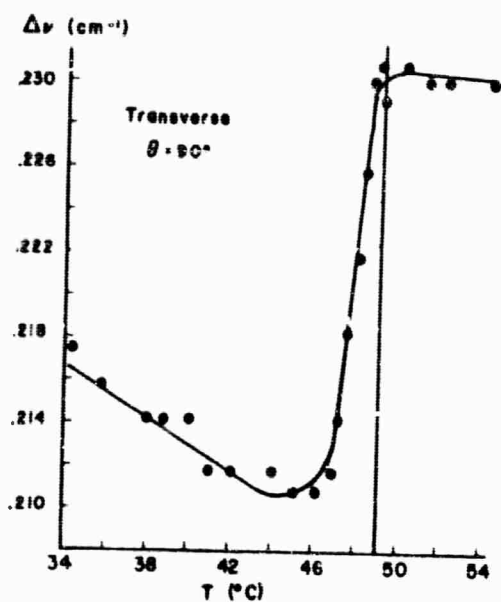
In order to interpret these data we must know the temperature dependence of the scattering vector magnitude q which can depend on T through the refractive index. We measured the refractive indices of TGS, n_o and an index in the (010) plane, with a Bausch and Lomb Abbe' refractometer at temperatures between room temperature and 55°C . We found the indices to be constant within 100 ppm from 34°C to 50°C . We can then conclude that to within our precision of frequency measurement the scattering occurs at constant q as the temperature is varied.

To assure that the direction of \hat{q} couldn't change as T was varied the extra precaution was taken of cutting faces on the sample normal to the incident and scattered light directions, \hat{k}_o and \hat{k}_s .

With \hat{q} constant we can interpret the changes in the frequencies as changes in the acoustic mode velocities. Thus we see that the L and T1 modes show a rapid increase in velocity as T approaches T_C from below, superimposed on a gradual decrease.

The total velocity increase indicated by the data in Fig. V 1 is 1% for the L mode and 9% for the T1 mode with the 90° and 135° scattering angle data showing the same total velocity dispersion. For a given mode the curves for the two scattering angles do not give the same $v(T)$. Instead the scattering with larger q ($\theta = 135^{\circ}$) shows the frequency starting to increase further from T_C than that for the smaller q ($\theta = 90^{\circ}$).

Fig. V 1 L and T1 mode Brillouin shift dispersion with temperature. $\theta = 90^\circ$ and 135° . $\phi(q) = -45^\circ$.



In Fig. V 2 we have plotted the difference from T_C of the temperature at which the frequency (velocity) was half way through the dispersion versus the frequency at that point. These points lie on a line given by $\omega = 3.4 \times 10^{10} (\text{sec. } ^\circ\text{C})^{-1} (T_C - T)$, with the phonon frequency in radians/sec.

These results are consistent with a single relaxation time velocity dispersion of the form

$$v^2 = \frac{\omega^2}{q^2} = v_\infty^2 - (v_\infty^2 - v_0^2) / [1 + (\omega\tau)^2]$$

with the relaxation rate τ^{-1} proportional to the temperature difference $(T_C - T)$ and ω the temperature dependent phonon frequency for fixed q . v_0^2 is the low frequency velocity limit and v_∞^2 the high frequency limit. Since $(v_\infty^2 - v_0^2) \ll v_\infty^2$ it is a reasonable approximation to take the half way point of the velocity dispersion as representing the half way point of the ω^2 dispersion where $\omega\tau = 1$. We then expect the half way point in the velocity (Δv) dispersion to occur at a $(T_C - T)$ proportional to the frequency at the half way point. Fig. V 2 supports this view so we extract the relaxation rate $\tau^{-1} = (3.4 \pm 10\%) \times 10^{10} (T_C - T) \text{ sec.}^{-1}$ with ΔT in $^\circ\text{C}$. The data for Fig. V 2 are given in Table V 2.

We have been able to fit the observed velocity dispersion $v(T)$ for each of the four cases studied to the single relaxation formula over most of the dispersion. This was done by reducing the shifts Δv for each mode and scattering angle to the quantity

$$D = [(\Delta v_\infty)^2 - (\Delta v)^2] / (\Delta v_\infty)^2$$

with Δv_∞ the limiting shift at $T \geq T_C$. Taking $\omega\tau = B/(\Delta T)$ and a

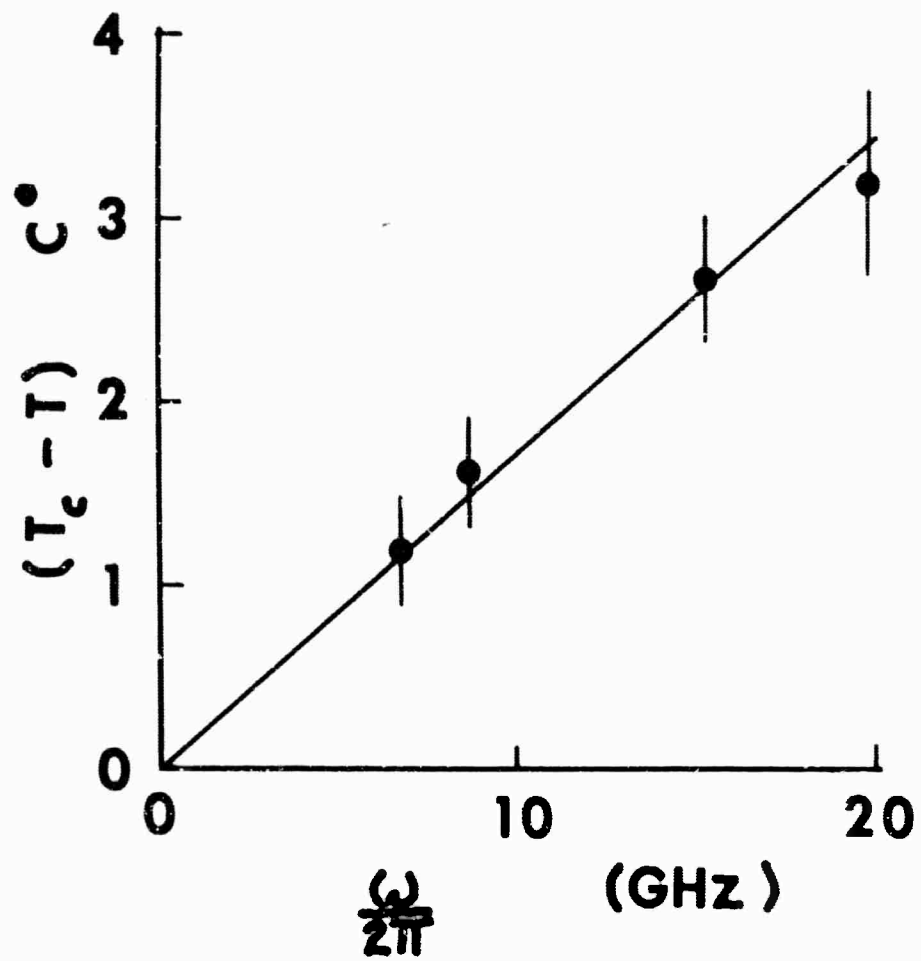


Fig. V 2 ΔT versus the mode frequency.

113
TABLE V2

RELAXATION TIMES IN TGS

$T_c - T$ (C°)	$\omega/2\pi$ (GHz)	ω (10 ⁹ rad. / sec.)	τ (10 ⁻¹¹ sec.)
1.2±.3	6.64	41.7	2.4
1.6±.3	8.70	54.6	1.8
2.7±.5	15.20	95.4	1.0
3.2±.5	19.80	124.3	.8

normalization $D_0 = [(\Delta v_\infty)^2 - (\Delta v_0)^2] / (\Delta v_\infty)^2$ we fit D/D_0 to the function $1 - 1/(1 + (\omega\tau)^2) = \omega\tau / (1 + (\omega\tau)^2)$ with B and D_0 as adjustable parameters. This function comes from the v^2 single relaxation dispersion formula by calculating $(v^2 - v_0^2)/(v_\infty^2 - v_0^2)$. The T1 data is more complicated because of the background temperature dependence. For this data we subtracted a linear (with temperature) decrease in D/D_0 of $2.5\%/C^\circ$. Fig. V 3 shows the normalized data and curves plotted against $\log \Delta T$. (The $\theta = 90^\circ$, L mode data which showed the largest scatter is omitted for clarity.) Table V 3 gives the parameters of the curve fitting. The parameters are consistent with the value of τ determined from the raw Δv versus T data.

As confirming evidence for the interpretation of the dispersion as due to a single relaxation time mechanism we have studied the linewidth of the 90° scattering Brillouin components in the region of the dispersion.⁽⁵³⁾ The raw linewidths of the components in the spectra, made up of the convolution of the laser, phonon, collection, and instrumental linewidths, are shown in Fig. V 4 for the T1 mode at $\phi(q) = -45^\circ$ and the L mode at $\phi(q) = -16^\circ$. We see that the L and T1 modes go through a maximum approximately at the ΔT of the dispersion half way point (equivalent to $\omega\tau = 1$) and drop to a low value (in fact the instrumental value) as T reaches T_C . Figure V 5 shows superimposed experimental traces of the minimum and maximum linewidths for the T1 component.

The frequency dependent velocity dispersion implies via a Kramers-Kronig analysis that there is an imaginary part of the phonon frequency $\omega = \omega(q)$ which describes the damping of the modes.⁽⁵⁴⁾

Introducing for the complex ω $\omega = \omega(q) = \omega' + i\omega''$ we find that if

Fig. V 3 Normalized change in v^2 versus $\log \Delta T$ (From same data as Fig. V1.) Labeled by mode and scattering angle. 50% intercept ΔT corresponds to $\omega\tau = 1$. (The L, $\theta = 90^\circ$ data points are omitted for clarity.) Typical error bars for the L and T1 modes are indicated.

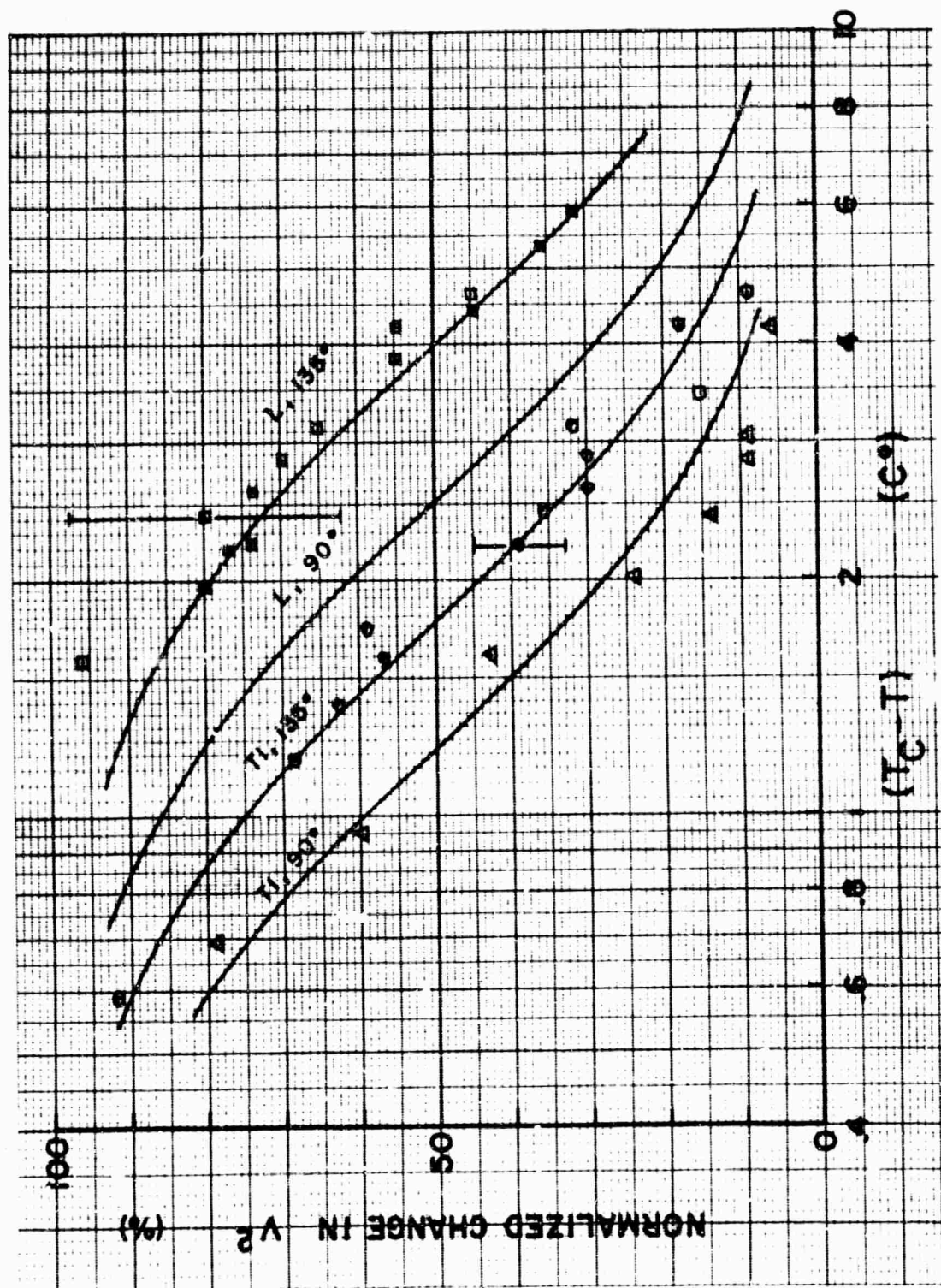


TABLE V 3

SUMMARY OF PARAMETERS FOR TEMPERATURE DISPERSION FIT
OF $(\Delta\nu)^2$ TO SINGLE RELAXATION FORMULA ^a

Mode	q (10^5 cm^{-1})	ω ($10^{10} \text{ rad./sec.}$)	$(\omega \tau) \Delta T$ ($^\circ\text{C}$)	$D_o^{(b)}$ (%)
L	2.72	12.43	$4.0 \pm .4$	2.1
L	2.07	9.54	$2.5 \pm .6$	2.1
Tl ^(c)	2.72	5.46	$1.8 \pm .3$	19.2
Tl ^(c)	2.07	4.17	$1.2 \pm .3$	19.2

^a \hat{q} at $\phi(q) = -45^\circ$.

^b D_o chosen for best fit. $D_o \equiv [v_\infty^2 - v_o^2] / v_\infty$.

^c Background slope of $-2.5\%/^\circ\text{C}$ subtracted before fitting.

Fig. V 4 Brillouin component linewidths versus temperature.
(Linewidths include the instrumental linewidth.)

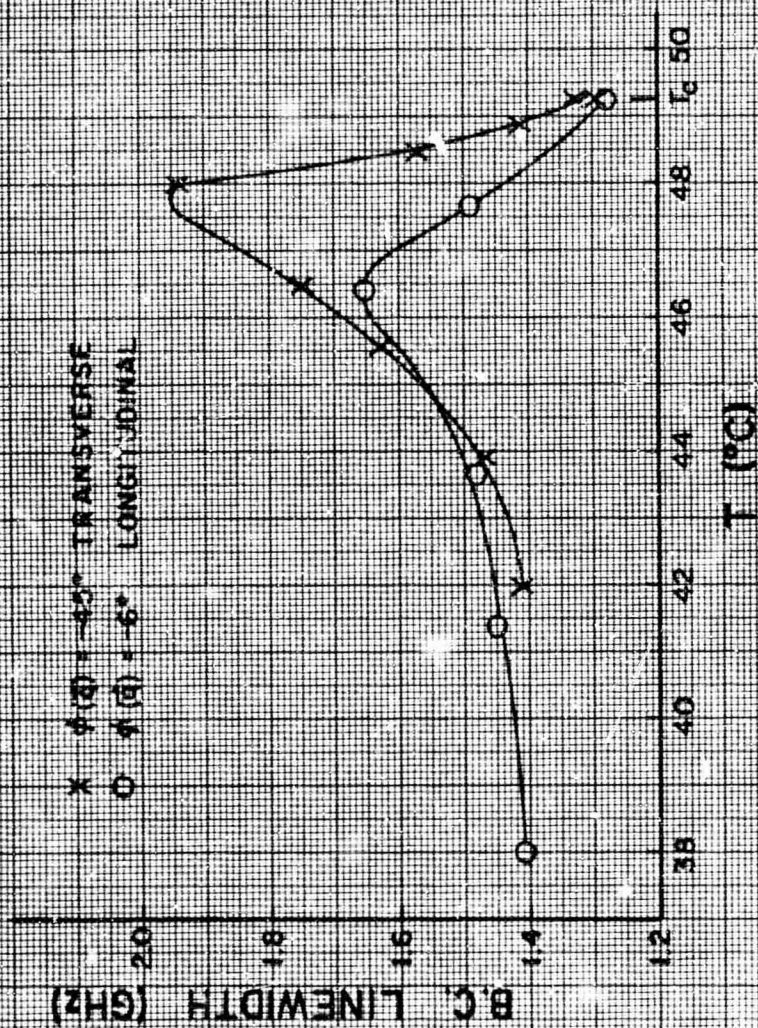
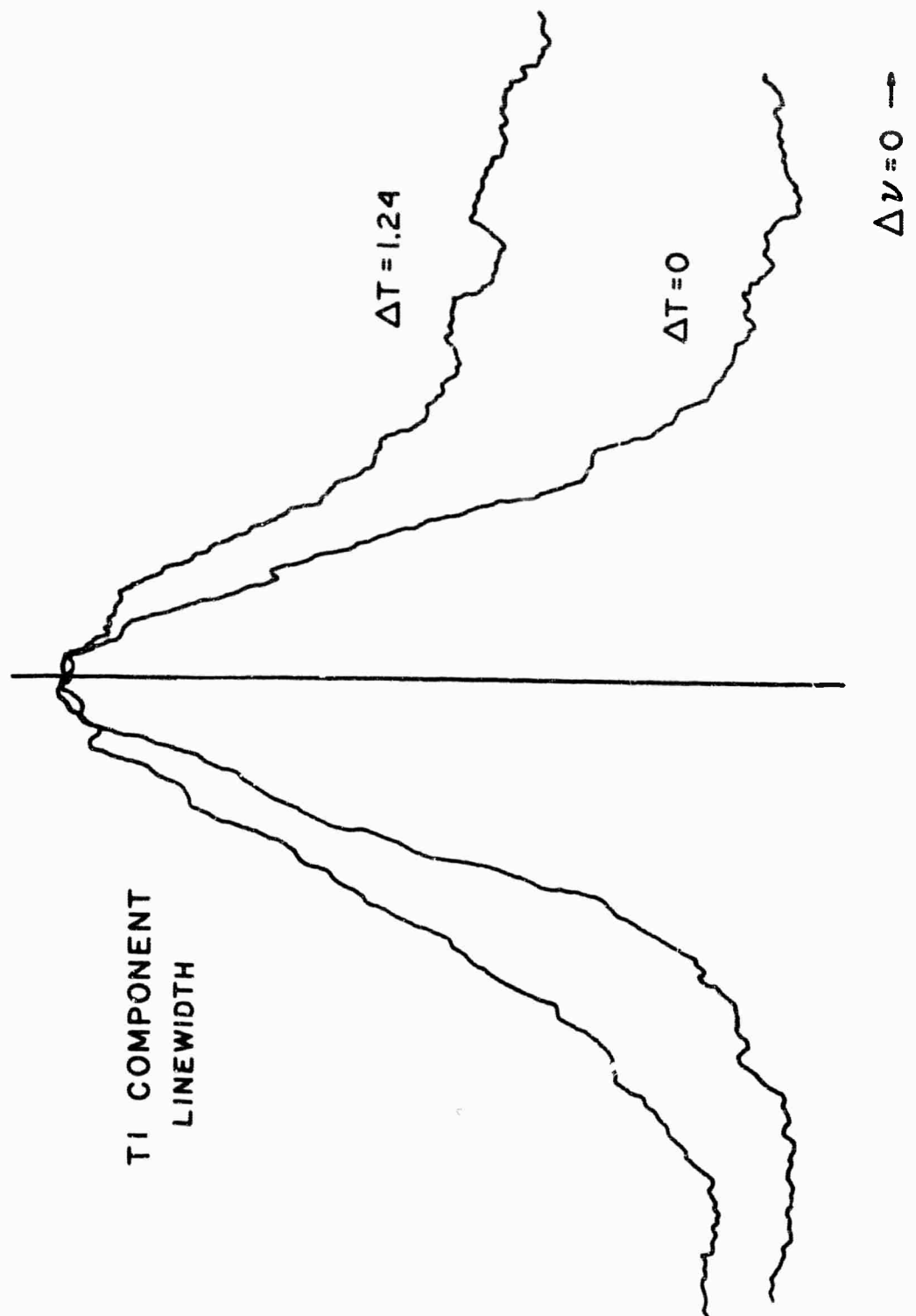


Fig. V 5 Superimposed T1 Brillouin component traces. $\Delta T = 0$ shows instrumental linewidth. $\Delta T = 1.24 \text{ C}^0$ shows maximum broadening. (In the superposition the peaks have been centered on the same line and made to coincide at the peak.)



$$\omega^2 = \omega_\infty^2 - (\omega_\infty^2 - \omega_0^2) / [1 + i\omega\tau]$$

then

$$\omega'^2 = \omega_\infty^2 - (\omega_\infty^2 - \omega_0^2) / [1 + (\omega'\tau)^2]$$

and

$$\omega'' = \frac{1}{2} (\omega_\infty^2 - \omega_0^2) \tau / [1 + (\omega'\tau)^2] ,$$

assuming that $(\omega_\infty^2 - \omega_0^2) \ll \omega_\infty^2$ so that $\omega'' \ll \omega'$. We see that in this approximation we have the expression used previously to fit the velocity dispersion and we have the phonon relaxation rate ω'' due to the single relaxation mechanism. ω'' is maximum at $\omega'\tau = 1$, where it has the value

$$(\omega'')_{\text{MAX}} = \frac{1}{2} (\omega_\infty^2 - \omega_0^2) / 2\omega' \approx \frac{1}{2} (\omega_\infty - \omega_0) .$$

The Brillouin component linewidth is just $2\omega''$ so we have the prediction that the maximum broadening of the Brillouin component is just equal to $(\omega_\infty - \omega_0)$, the total frequency dispersion.

The convolution which gives the linewidth of the experimental spectral trace is very complicated. We will make the gross simplification that we can take the maximum difference in observed linewidth and instrumental linewidth (1.2 GHz) as giving the maximum Brillouin component broadening. Doing this we find the maximum change in the T1 linewidth was .63 GHz and the maximum change in the L linewidth was .37 GHz. For comparison the total dispersion was .60 GHz for the T1 mode and .45 GHz for the L mode for the

respective \hat{q} directions. The agreement is satisfactory.

The detailed shape of the curves of excess linewidth versus ΔT does not fit the prediction but this is believed to be due to the convolution problem. The maximum occurs at the expected ΔT and the magnitude of the maximum linewidth increase agrees with the total dispersion. Thus we feel quite confident in our interpretation.

From the temperature dependence of the Brillouin shifts away from the regions of relaxational dispersion we have extracted velocity temperature coefficients. These are given in Table V 4 for the L and T1 modes. In some cases especially for the T1 mode the coefficients seem to change near T_C , so we have given values for the region above and below T_C .

The slopes and their difference above and below T_C are not explained by the theory to be given in this thesis. The observed velocity changes are equivalent to changes in elastic constants of from < 200 to 2000 ppm/C° . These values are typical of most crystalline solids.

The crystals used in this study were conditioned in the polar phase by "poling" with a 5 kV/cm dc electric field applied along the ferroelectric axis (b). This was applied in the $-\hat{b}$ direction. (We take the convention of calling $+\hat{b}$ the direction for which \hat{a} , \hat{b} and \hat{c} form a right handed triad.) Call this a left handed sample. A right handed sample (an electrical twin) can be made by poling the crystal with the field parallel to \hat{b} . A left handed sample has opposite signs of its piezoelectric coefficients from a right handed sample but its elastic stiffness coefficients are the same. We checked in a few cases and found the Brillouin shifts not to depend on the sample

123
TABLE V 4

(010) PLANE VELOCITY TEMPERATURE COEFFICIENTS

$\theta(q)$	Temperature Coefficients (m/зec. C ⁰)			
	L		L	
	$T > T_C$	$T < T_C$	$T > T_C$	$T < T_C$
-77	.4	.4	--	--
-30	.6	0.	3.0	5.1
-20	0.	0.	2.3	2.7
0	0.	0.	5.3	2.6
15	0.	0.	0.	6.8
55	3.8	3.8	2.4	6.5
50	2.9	2.9	3.2	3.2
65	--	5.6	--	3.0

handedness but for consistency all work reported here was on left handed samples. The poling was done at the initial lowest temperature of each temperature run. The crystal electrodes were then shorted and remained so as long as the temperature was being increased. The crystal was repoled after each temperature decrease.

We went to this care in poling the samples to make sure that they were single domain during our measurements. In some later work we found that the domain walls could sometimes be visible in the laser beam.⁽⁵⁵⁾ This allowed us to check our poling procedure. We found that unless the sample had been cooled from T greater than T_C with a field applied, poling at T less than T_C did not give a permanent single domain. We then prepared a permanent single domain sample by cooling with field applied and ran spectra at $\phi(q) = -45^\circ$ versus T . Complete agreement with earlier work was obtained.

Field Dependence of the Brillouin Shifts⁽⁵⁶⁾

We studied the effect of dc electric fields applied parallel to the ferroelectric (b) axis of TGS.

The crude test for an effect was to hold the sample at T_C and run spectra with the electrodes shorted and then with 3 to 4 kV applied. The samples were all about .7 cm thick so this gave fields of about 5 kV/cm. We observed that for the directions in which temperature dependent $\Delta\nu$ had been observed, the L and T1 mode component shifts decreased with applied field. Moreover the magnitude of the maximum change with field observed was the same as the total change observed when the temperature was varied. The field gave no effect for directions in which there was no temperature effect and the

T2 mode (HV scattering) showed no field effect.

Before we could interpret this as a field dependent relaxation effect we had to look for a field dependence of the refractive indices. This was done by looking for a change in deflection of a laser beam traversing a prism of TGS. We found no detectable effect for fields up to 9 kV/cm. We could have detected changes of .05%. Since the refractive indices are independent of field, \hat{q} was independent of field and we may interpret the changes in Brillouin shifts as changes in the L and T1 mode velocities.

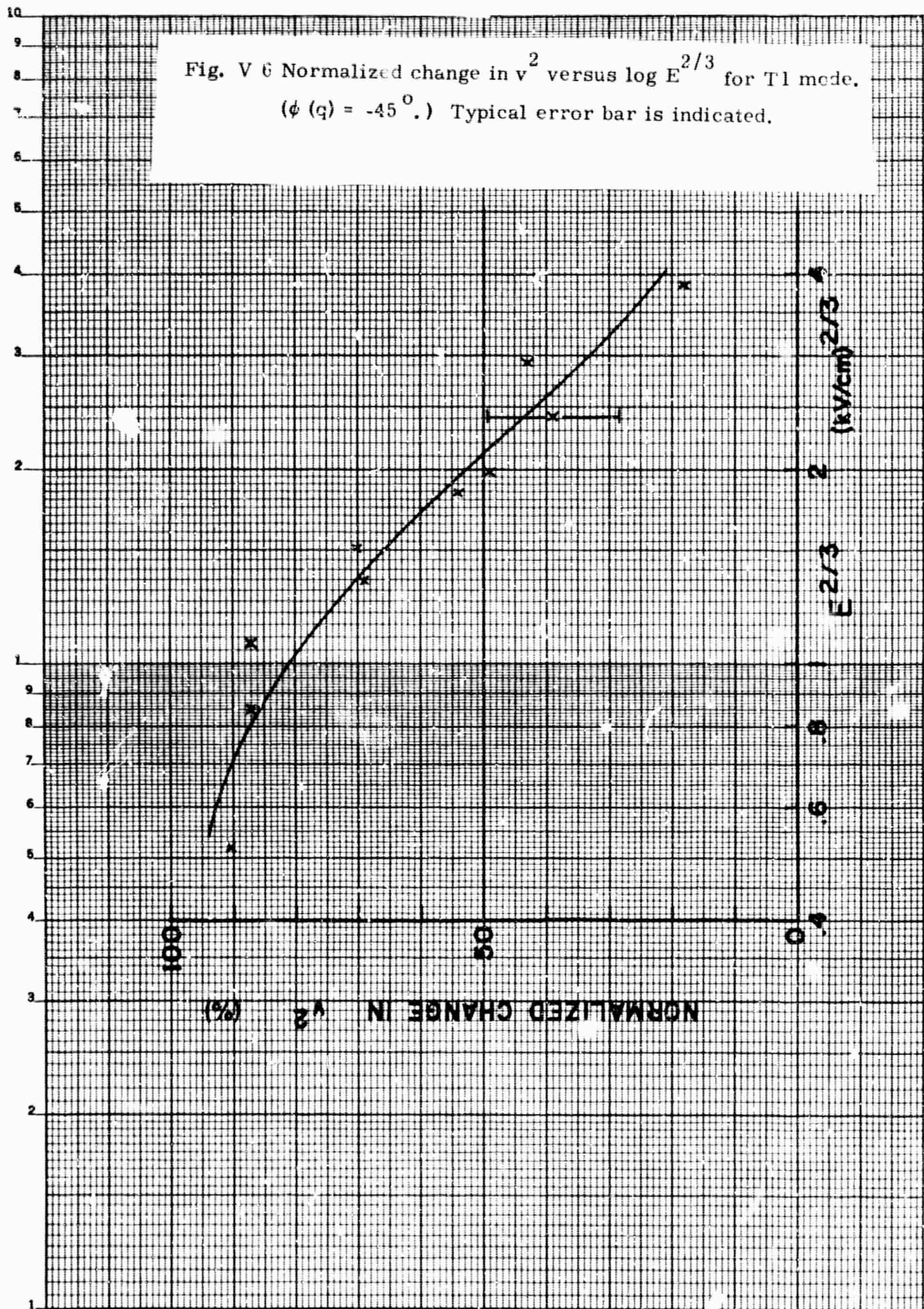
We studied the field dependence in detail for $\phi(q) = -45^\circ$. We limited the fields to 7.5 kV/cm because of trouble with electrical breakdown at 9 kV/cm. With these fields we could change the T1 mode shift almost back to the minimum value that it has for T less than T_C and to reduce the L mode shift about half way to its low temperature value.

The theory to be presented in Section VI predicts a field dependent relaxation rate at T_C proportional to $E^{2/3}$. Figure V 6 shows the normalized change in $(\Delta v)^2$ for the T1 mode plotted against $\log E^{2/3}$. The data in this form is fit very well by the single relaxation time (predicted) function $\omega\tau / (1 + (\omega\tau)^2)$ with $(\tau)^{-1} = 2.0 \times 10^{10} E^{2/3} \text{ sec.}^{-1}$, E in kV/cm, and $(v_\infty^2 - v_0^2)/v_\infty^2 = 15\%$.

Using this relaxation rate we predict that the $\omega\tau = 1$ occurs for the L mode at $E = 10 \text{ kV/cm}$ well above the fields applied. This is consistent with the small change in the L shift which began to appear for $E^{2/3} > 2(\text{kV/cm})^{2/3}$.

We also observed the T1 Brillouin component linewidth broadening near the field giving $\omega\tau = 1$. As in the case when

Fig. V 6 Normalized change in v^2 versus $\log E^{2/3}$ for T1 mode.
 ($\phi(q) = -45^\circ$.) Typical error bar is indicated.



temperature was varied the maximum increase in linewidth of .6 GHz was consistent with the total frequency dispersion. Thus the single relaxation description of the field effect is firmly established.

Other Observations

We made a study of the temperature and field dependence of the Brillouin shifts for various directions of \hat{q} in the (010) plane in addition to $\phi(q) = -45^\circ$. Using $(v_\infty - v_c)$ as a measure of the coupling we found the coupling to be very anisotropic but the temperature dependent relaxation time was independent of \hat{q} within our experimental uncertainty of $\pm 10\%$. This anisotropy is shown in Fig. V 7. The range of directions over which the T1 mode could be studied was limited by the intensity variation for this component. A more careful study with polarized spectra to select just the T1 mode (VV) could extend the range of angles somewhat. (Re Section IV) The curves drawn through the data points are just guesses of the shape. Calculations performed with the theory of Section VI have shown that the velocity difference versus \hat{q} has no simple closed expression and is very sensitive to the values chosen for the electrostriction coefficients. We do find an interesting correspondence between the coupling anisotropy pattern for the L mode and the thermal expansion measured by Izhkova et al.⁽⁵⁷⁾ The thermal expansion pattern in (010) plane showed maxima near the $\pm \hat{c}$ directions. In Section VI we will see that this pattern of expansion and the coupling anisotropy are related through the same coefficients to the electric polarization.

The decrease in velocity for the L and T1 modes for a 5 kV/cm field applied parallel to \vec{b} and the sample at T_C was determined as a

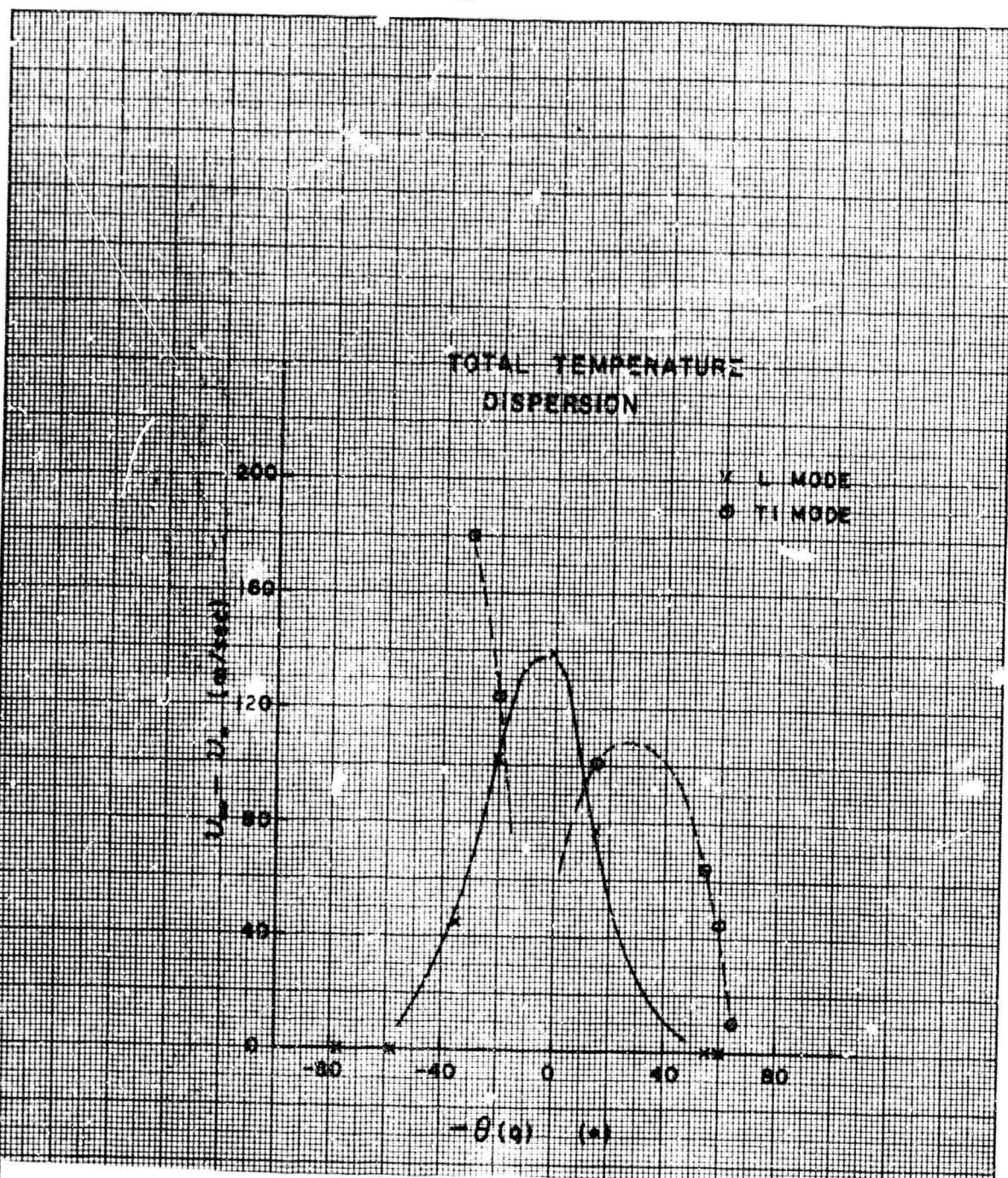


Fig. V 7 Total temperature dispersion, $v_\infty - v_0$, versus $\theta(q)$.
 ($v_\infty - v_0$ is a measure of the coupling anisotropy.)

function of the \hat{q} direction in the (010) plane. The results were consistent with the above temperature scan work in giving the relative coupling versus \hat{q} but the magnitudes of the velocity changes were all smaller. We believe this to be due to using too small a field to depress the velocity to the $\omega\tau \ll 1$ limit. Using the field dependent relaxation time previously observed we can calculate that a field of 68 kV/cm would be required to take the L mode 90° scattering angle frequency through at least 90% of its dispersion at any \hat{q} in the (010) plane. Similarly it would take 23 kV/cm for the T1 mode.

We studied the temperature and field dependence of the T2 mode (\hat{q} in (010) plane and displacement parallel to \hat{b} --a pure shear mode) in HV spectra. No relaxation effects near T_C were detectable. The Brillouin shifts and hence the velocities were essentially independent of T and field. For example at $\phi(q) = -45^\circ$ we observed the velocity to show only a slow decrease with temperature (2 m/sec./ $^\circ\text{C}$) and a small increase with applied field at T_C . Thus it appears that the T2 mode is not coupled to the relaxing entity which effects the L and T1 modes.

Finally we studied the temperature dependence of the longitudinal mode Brillouin component with \hat{q} parallel to \hat{b} . The Brillouin shift and hence longitudinal velocity was found to be essentially temperature independent showing only a slow decrease with temperature of 1.8 m/sec./ $^\circ\text{C}$. This is surprising since the low frequency work ⁽⁵⁸⁾ showed an anomaly in s_{22} . This shows that the coupling is non-zero but our observation agrees with that of O'Brian and Litovitz. ⁽⁵⁹⁾ We will show in Section VI that this discrepancy has an especially interesting explanation.

Critical Opalescence

As T approaches T_C the observed pole in the dielectric constant ϵ_2 shows that the thermal fluctuations in the y component of the electric polarization P_2 occur easily and so get large. Just as in liquid-vapor critical phenomena one might expect that if the optical polarizability of the crystal was modulated by ΔP_2 a large increase in light scattering would occur as the fluctuations in P_2 get large near T_C . A more detailed argument appropriate to TGS, which is non-piezoelectric in the non-polar phase, indicates that the total scattering intensity due to polarization fluctuations will be constant through $T_C^{(60)}$ but that its spectrum centered at the incident frequency will become very narrow near T_C .

We looked for critical opalescence of this latter type after most of our Brillouin scattering work was completed when very high quality samples became available. Fig. V 8 shows the scattering spectrum of a good, freshly polished sample of TGS at T_C . The relatively low amount of elastic scattering shown in the central component showed no temperature dependence as T moved away from T_C so is believed due to crystal imperfections. We conclude that the optical dielectric constant gives an integrated VV scattering cross section small compared to that for Brillouin scattering in TGS.

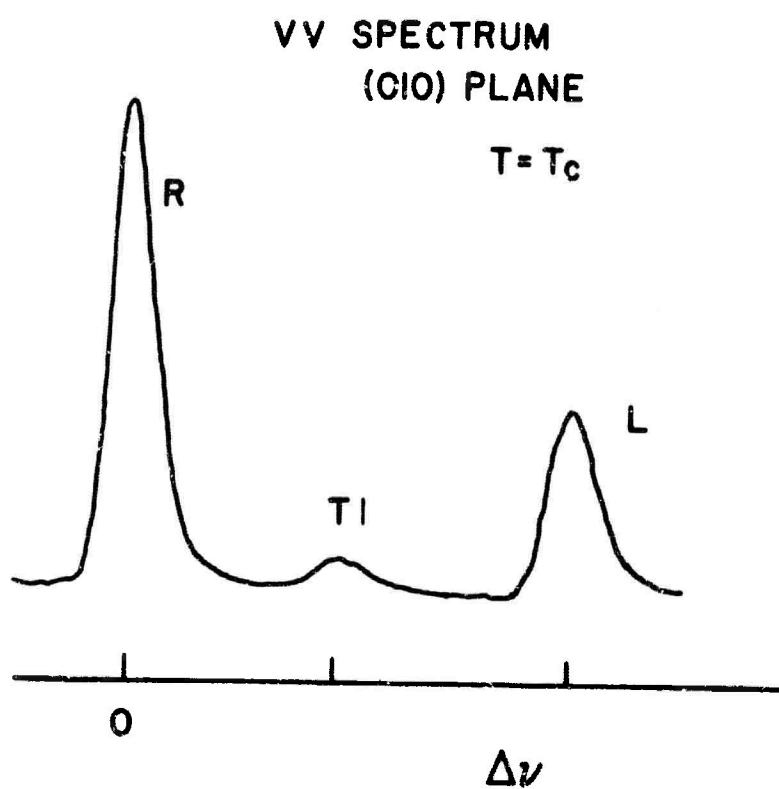


Fig. V 8 VV spectrum, $\phi(q) = -45^\circ$, showing Rayleigh component (R), T1 component, and L component at T_C .

SECTION VI

A THERMODYNAMIC POTENTIAL THEORY FOR THE STRAIN AND POLARIZATION FLUCTUATION DYNAMICS IN TGS NEAR ITS FERROELECTRIC PHASE TRANSITION

In Section V we gave the experimental evidence that showed that the L and T1 acoustic modes of the (010) plane in TGS are coupled to a single relaxing quantity (i. e. , are coupled to a quantity having an exponentially damped autocorrelation function). The degree of coupling indicated by the total dispersion is different for the two modes and for different \vec{q} directions but the temperature-frequency dependence was always the same indicating that there is only a single temperature dependent relaxation rate for all \vec{q} in the (010) plane.

In this section we will give a phenomenological theory of the phase transition in TGS based on a model free energy expansion with electrostrictive terms and a simple application of the ideas of irreversible thermodynamics. With this theory we show that relaxing thermal fluctuations of the spontaneous polarization of ferroelectric TGS can account for all of our velocity dispersion observations near T_C . This includes the selection rule that the T2 mode is not coupled to the polarization fluctuations, quantitatively relating the temperature and field dependent relaxation rates, and qualitative agreement on the anisotropy of the total dispersion in the (010) plane.

We begin with a discussion of the general behavior of ferroelectrics near the Curie temperature. We show how the dielectric behavior can be given a unified description using an appropriate

thermodynamic potential. With this as background we give a thermodynamic potential for TGS expanded in the variables strain and polarization along the ferroelectric axis. From this potential we deduce the equilibrium polarization and strain as functions of temperature. We then derive equations relating the spatial Fourier components of the fluctuations from their equilibrium values of polarization and strain. Assuming that fluctuations of polarization decay exponentially we derive the temperature dependent relaxation rate and the frequency dependent elastic stiffness constants which predict a single relaxation time dispersion in the acoustic mode frequencies for a given wave vector \vec{q} . From the measured relaxation rate we can extract the kinetic coefficient of the polarization fluctuations.

Using dielectric and electrostriction parameters from the literature we evaluate our derived expressions and give the calculated coupling anisotropy for (010) plane acoustic modes in TGS.

Next we derive the effect of an applied electric field on the fluctuation dynamics and find a field dependent relaxation of the polarization and an associated velocity dispersion.

Finally we derive the fluctuation dynamics for the case of \vec{q} parallel to the ferroelectric axis. Here we must add a term to the free energy to account for the electrostatic energy of the polarization fluctuations. This leads to a fast and essentially temperature independent relaxation rate so that no temperature dependent relaxation should occur in agreement with experiment.

Ferroelectric Phase Transitions

As was stated in Section 7 a ferroelectric crystal is a polar class crystal exhibiting a pyroelectric polarization which can be

reversed by an applied electric field. Our interest in ferroelectrics centers around the phase transitions that they exhibit. We shall see that the crucial property of these crystals near the ferroelectric phase transition (polar to non-polar) is their large, temperature dependent dielectric constant which increases like $|T - T_C|^{-1}$ near T_C . A crystal showing this behavior is said to obey the Curie law, in analogy with ferromagnetic transitions which exhibit a like behavior in the susceptibility. Ferroelectrics exhibiting simple second order transitions in which their thermodynamic variables are continuous have their spontaneous polarization P_s go continuously to zero as T approaches T_C in the polar phase with P_s^2 proportional to ΔT . Such behavior is expected of the ordering of any system in which the long range forces predominate. It is the analog of the behavior predicted at the critical point of a van der Waals gas with P_s replacing the liquid-gas density difference and the dielectric constant replacing the isothermal compressibility.

The recent dielectric measurements of Craig⁽⁶¹⁾ and Gonzalo⁽⁶²⁾ on TGS were carried to great precision in order to look for any deviation from the behavior

$$\epsilon^{-1} = \text{const} \times (\Delta T)^\gamma$$

with $\gamma = 1$. Gonzalo found $\gamma = 1.00 \pm .05$ carrying the measurements in to within $50 \times 10^{-3} \text{ } ^\circ\text{C}$ of T_C before being limited by the sample quality. Gonzalo also found

$$P_s^2 = \text{const} \times (T_C - T)^{1.0 \pm .1}$$

near T_C . Thus TGS seems to be an outstanding example of a system

exhibiting classical behavior in the region of a second order phase transition. This is perhaps not surprising since the predominant forces in ferroelectrics are believed to be electrostatic and therefore long range.

The general features of ferroelectric crystal properties and their phase transitions have been very successfully described in a unified manner through the use of thermodynamic potentials. We will review a simple illustration of this by showing how the dielectric properties of a ferroelectric having a second order transition can be deduced from a model thermodynamic potential.

We use the Gibbs function $G(T, X_1, P)$, a function of temperature, stress and the polarization component along the ferroelectric axis. We expand this as

$$G(T, 0, P) = \frac{1}{2} \chi P^2 + \frac{1}{4} \xi P^4 + \dots$$

and assume that this expansion holds with the same coefficients throughout the transition region. We take only even powers of P to conform to centrosymmetric symmetry. We assume that ξ is greater than zero and independent of temperature and that $\chi = (4\pi/C)(T - T_C)$ with $C > 0$. We assume the expansion converges rapidly enough to neglect the 6th and higher order terms. We now find that the system will undergo a second order phase transition at T_C . First we compute the equilibrium polarization for the condition that the electric field (generalized force) conjugate to P is zero. We calculate E in the standard way as a partial derivative of G giving

$$E = \frac{\partial G}{\partial P} = \chi P + \xi P^3.$$

Setting $E_2 = 0$ we find that G is minimum if

$$P_2 = 0 \quad \text{for } T > T_C$$

and

$$P_2^2 = -\chi / \xi \pm P_s^2 \quad \text{for } T < T_C .$$

Thus we find that there is no spontaneous polarization above T_C but that below T_C , P_2 has two (\pm) stable non-zero values and the square is proportional to ΔT .

Next we derive the reciprocal dielectric susceptibility

$$\kappa_2^{-1} = \left. \frac{\partial^2 G}{\partial P^2} \right|_{\text{equi.}} = \left. \frac{\partial E}{\partial P} \right|_{\text{equi.}} .$$

With ΔP the deviation of P_2 from equilibrium, above T_C

$$E = \chi \Delta P + \xi (\Delta P)^3$$

so that the reciprocal susceptibility is

$$\left. \frac{\partial E}{\partial P} \right|_{\Delta P=0} = \chi .$$

Below T_C

$$E = \chi \Delta P + 3\xi P_s^2 \Delta P = -2\chi \Delta P$$

so that the reciprocal susceptibility is

$$\left. \frac{\partial E}{\partial P} \right|_{\Delta P=0} = -2\chi .$$

Now $4\pi\chi'_2 \approx \epsilon_2$ so that above T_C $\epsilon_2 \approx 4\pi/\chi = C/(T - T_C)$ and below T_C $\epsilon_2 \approx -4\pi/2\chi = (C/2)/(T_C - T)$.

Thus we have reproduced the behavior described earlier for ferroelectrics near T_C with P continuous throughout the transition which is therefore of second order.

Further discussion of thermodynamic potentials (free energies) in ferroelectrics can be found in the review by Jona and Shirane.⁽⁶³⁾ They have based their presentation on the work of Mueller, Cady and Devonshire. They give a very useful bibliography of earlier reviews on ferroelectric crystals at the end of their first chapter.

The idea of producing second order transition behavior from a free energy expansion goes back to L. D. Landau who gave a theory of second order transitions in 1937.⁽⁶⁴⁾ The basic idea is to identify a variable η labeled the order parameter in terms of which the free energy expansion has the form

$$F = \frac{1}{2}a(T - T_C)\eta^2 + \frac{1}{4}\xi\eta^4 + \dots$$

We know from the previous discussion that this model free energy will yield a thermodynamic second order transition if $\xi > 0$.

In a ferroelectric we see that the spontaneous polarization corresponds to the order parameter. In TGS the equilibrium P_2 measures the average degree to which the unit cells of the microscopic structure have the same handedness.

We wish to emphasize that the phenomenological theories of ferroelectrics really represent particular cases of the general approach of free energy power series expansions. This more

general viewpoint is well documented in the Russian literature. A good introduction is found in Statistical Physics by Landau and Lifshitz.

Because the spontaneous and induced polarizations can be large in ferroelectrics the coupling of strain (or stress) with electric polarization (or field) is important in understanding the behavior near T_C . TGS is centrosymmetric in the non-polar phase so the coupling between polarization and strain is expected to be electrostrictive, that is with the strain proportional to P^2 . It is crucial in developing a phenomenological theory for TGS to include electrostrictive terms in the thermodynamic potential to account for the (morphic) piezoelectricity of polar TGS and the coupling of strain waves to polarization fluctuations.

Having calculated the temperature dependence of the equilibrium dielectric properties we could now go on to calculate the mean square fluctuations as well as the time dependence of the fluctuations of P . These fluctuations become very large and slow as χ gets small near T_C . They are an example of critical point fluctuations. Actually since the fluctuations of interest are inhomogeneous, we can not consider polarization fluctuations separately from the inhomogeneous strain fluctuations which can not be eliminated (clamped). Therefore we will turn to the detailed analysis of the equilibrium properties and fluctuations derived from a model thermodynamic potential for TGS which includes elastic and electrostrictive terms. The derivation is a general one for a ferroelectric which is centrosymmetric in the non-polar phase and has a unique ferroelectric axis direction.

Thermodynamic Potential Derivation of the Equilibrium Properties of TGS

O'Brian and Litovitz⁽⁶⁵⁾ were the first to combine the Landau-Khalatnikov derivation of the relaxation time for order parameter fluctuations⁽⁶⁶⁾ with the Devonshire theory of ferroelectricity⁽⁶⁷⁾ in a detailed calculation of the elastic properties of TGS near T_C . We will follow them in using the same model thermodynamic potential expansion.

Our analysis will lead to more detailed predictions of relaxation effects in the elastic constants but qualitatively they are the same as the results derived by O'Brian and Litovitz.

We will use the Helmholtz free energy $A(T, x_1, P_2)$, a function of temperature T , strains x_1 , and the y (b) component of polarization P_2 . (The ferroelectric axis is the C_2 axis as is required by symmetry in a monoclinic crystal.) In the derivations using this free energy we will ignore the difference between isothermal and adiabatic fluctuations. The fluctuations observed in light scattering are approximately adiabatic while the fluctuations calculated with the Helmholtz free energy are isothermal. From the expression given by Cady for the difference between isothermal and adiabatic elastic compliance coefficients we have calculated the conservative estimate of 30 ppm for this difference. This is based on the background thermal expansions observed by Ezhkova, et al.⁽⁶⁸⁾ of 10 ppm/ $^{\circ}\text{C}$ and a heat capacity $\geq 2 \times 10^7$ ergs/cc $^{\circ}\text{C}$ near T_C .⁽⁶⁹⁾

Our model for the free energy is⁽⁷⁰⁾

$$A - A_0 = \frac{1}{2} c_{jk} x_j x_k + g_{2j} x_j P_2^2 + \frac{1}{2} \chi P_2^2 + \frac{1}{4} \xi P_2^4$$

where A_0 is the free energy at temperature T and zero strain and polarization. The coefficients are the elastic stiffness constants c_{jk} , the stress electrostriction constants g_{2j} , the inverse susceptibility χ and a dielectric nonlinearity parameter ξ . They are in general temperature dependent but we assume that they vary smoothly through the transition. Specifically our model will be that

$$\chi = \frac{4\pi}{C}(T - T_C)$$

with $C > 0$, $\xi > 0$, and that the coefficients other than χ have negligible temperature dependence.

The coupling between P_2 and strain is through an electrostriction constant rather than directly through a piezoelectric coefficient. This avoids assuming temperature dependent piezoelectric coefficients which go to zero as $(T_C - T) > 0$ goes to zero. This is an essential element of Devonshire's approach to a theory of ferroelectricity. The polar (piezoelectric) phase is to arise from the spontaneous polarization and strain of an initially centrosymmetric crystal form. (TGS goes from monoclinic C_2 to monoclinic C_2/m as T increases through T_C .)

Below T_C , P_2 will have a spontaneously non-zero value. Due to the coupling between P_2 and strains there will also be spontaneous strain.

We calculate these in the standard way by minimizing the free energy thereby requiring that the electric field E_2 and the stresses X_j be zero for equilibrium at temperature T_C .

$$X_j = \frac{\partial A}{\partial x_j} = c_{jk}^P x_k + g_{2j} P_2^2$$

$$E_2 = \frac{\partial A}{\partial P_2} = \chi P_2 + \xi P_2^3 + 2g_{2j} P_2 x_j$$

Setting X_j and E_2 equal to zero and looking for minima in A we find

$$(P_2)_0^2 = P_s^2 = -\frac{\chi}{(\xi - 2gsg)}$$

and

$$(x_k)_0 = -s_{jk} g_{2j} P_s^2$$

where we are denoting the spontaneous polarization as P_s , s_{jk} is the matrix of elastic compliance coefficients (inverse to the elastic stiffness matrix) and the scalar constant gsg is $g_{2j} s_{jk} g_{2k}$. By assumption χ is proportional to $(T - T_C)$ so that P_s^2 and also $(x_k)_0$ must go to zero as $(T_C - T)$.

Above T_C only $P_2 = 0$ and $x_k = 0$ give zero field and stress so the average polarization and strain are zero.

The temperature dependence of P_s^2 has been checked by Gonzalo.⁽⁴⁸⁾ The spontaneous strain prediction has not been critically tested near T_C but the x-ray measurements of Ezhkova, Zhdanov and Umanski⁽⁵⁷⁾ showed that the thermal expansion in various directions has a change in slope at T_C in TGS.

Thermodynamic Fluctuations in TGS

We now consider fluctuations. We wish to derive the equations giving the fluctuations in stress and field from their equilibrium values in terms of the fluctuations in strain and polarization from their equilibrium values. We do this by linearizing the equations for stress and field to give

$$X_j = c_{jk}^P(\Delta x_k) + 2g_{2j}P_2(\Delta P_2)$$

$$E_2 = 2g_{2j}P_2(\Delta x_j) + (\chi + 3\xi P_2^2 + 2g_{2j}x_j)(\Delta P_2)$$

where Δx_k and ΔP_2 are the fluctuations about X_k and P_2 and $X_j = \Delta X_j$ and $E_2 = \Delta E_2$ in the absence of applied stress or field.

Above T_C substitution of the zero equilibrium values of strain and polarization into the linearized equations gives

$$X_j = c_{jk}^P(\Delta x_k)$$

$$E_2 = \chi(\Delta P_2).$$

This shows that the strain and polarization fluctuations are uncoupled above T_C . For this case the dynamics of the fluctuations can be treated separately. We will return to this below.

Below T_C substitution of the spontaneous strains and polarization into the linearized equations gives

$$X_j = c_{jk}^I(\Delta x_k) + 2g_{2j}P_s(\Delta F_2)$$

$$E_2 = 2g_{2j}P_s(\Delta x_j) + 2\xi P_s^2(\Delta P_2).$$

Light scattering experiments probe particular Fourier components of inhomogeneous fluctuations in the scattering volume. Hence it is convenient to treat the fluctuations in terms of spatial Fourier components. As in Section I we define spatial components as

$$y(\hat{q}) = \frac{1}{V} \int_V y(\hat{r}) e^{-i\hat{q} \cdot \hat{r}} d^3r$$

for any variable $y(\hat{r})$ with V the scattering volume. We will simplify the notation by labeling the components with the letter q rather than \hat{q} but we will need to remember that there is a directional dependence. In terms of spatial Fourier components we find for T below T_C

$$X_j(q) = c_{jk}^P x_k(q) + 2g_{2j}^P P_s P_2(q)$$

$$E_2(q) = 2g_{2j}^P P_s x_j(q) + 2\xi_s^2 P_s^2 P_2(q) .$$

Polarization Fluctuation Dynamics

The polarization fluctuations are assumed to be thermodynamic fluctuations which decay exponentially or more precisely the fluctuations show an exponential time correlation. We follow the general treatment of the non-equilibrium thermodynamics of order fluctuations near a second order transition given by Landau and Khalatnikov ⁽⁷¹⁾ in calculating relaxation rates.

Treating the polarization fluctuations as being non-propagating damped modes represents a particular limit of the microscopic viewpoint of ferroelectrics put forth by Ginzberg ⁽⁷²⁾ and Cochran. ⁽⁷³⁾ In this view the dielectric anomaly is due to the presence of a temperature dependent, low frequency, infrared active, optical lattice vibration. First approximations have taken this mode to be harmonic and therefore lossless. Experiments seeking to find this type of behavior have been unsuccessful except in SrTiO_3 ⁽⁷⁴⁾ and even there the losses were large near T_C . In the other cases the damping is very large so that the mode appears to have a complex frequency with no real part. In these cases the thermodynamic

treatment may come closer to the true behavior.

We start with the kinetic assumption of non-equilibrium thermodynamics that the rate of change of a fluctuating variable is proportional to the thermodynamic "force," where this "force" is the partial derivative of the free energy with respect to the variable, evaluated at the instantaneous values of the fluctuating variables. In our problem this is written as

$$\frac{\partial P_2(q)}{\partial t} = -\gamma \frac{\partial A}{\partial P_2(q)} = -\gamma E_2(q) .$$

γ is called the kinetic coefficient. Note that we are applying the idea of relating variables and forces to the Fourier components of inhomogeneous fluctuations in P_2 . We assume γ to be a constant but it is not inconceivable that there are cases where it depends on \vec{q} . One might expect shorter wavelength polarization fluctuations to decay more rapidly for a given $E_2(q)$, i. e. that γ increases with q .

We can apply the kinetic equation directly in deriving the dynamics above T_C . Here we find

$$\dot{P}_2(q) = -\gamma \chi P_2(q)$$

so that the relaxation rate is

$$\tau^{-1} = \gamma \chi ,$$

which is proportional to $(T - T_C)$ because of the assumed temperature dependence of χ .

Since the polarization and strain fluctuations are uncoupled above T_C we do not expect the Brillouin components to be effected by the temperature dependent polarization dynamics. The spectrum

of the polarization fluctuations is a Lorentzian about $\Delta\omega = 0$ with full width at half maximum of $2/\tau_p$. This spectrum could show up in light scattering spectra but as discussed at the end of Section V it did not appear for TGS.

Dynamics of Coupled Fluctuations Below T_C

We now wish to determine the dynamics of individual Fourier components of the coupled strain and polarization fluctuation below T_C . Even in the phenomenological theory being presented here this is a difficult problem to solve exactly. For a given q we must reduce the 7×7 matrix relating the six strains and the polarization to the six stresses and the field to a 4×4 eigenfrequency problem. The (complex) secular equation would have four complex roots.

Rather than attack the problem directly in complete generality we will use the approximation of separating the coupled fluctuations by their dynamics. In general we expect to find one pure damped solution and three solutions with non-zero real parts of their frequencies. We will separately look for pure damped solutions and damped oscillatory solutions.

For example sufficiently near T_C the pure damped (coupled) fluctuation relaxation rate can be calculated very simply from the kinetic equation by assuming the polarization fluctuations to occur so slowly that the strain follows them easily giving fluctuations at constant (zero) stress. For this case we find

$$\dot{P}_2(q) = -\gamma E_2(q) = -\gamma 2(\xi - 2gsg)P_s^2 P_2(q)$$

so that P_2 relaxes with the rate

$$\tau_X^{-1} = \gamma 2(\xi - 2gsg)P_s^2$$

which is proportional to $(T_C - T)$ due to the factor P_s^2 . gsg is the scalar constant $g_{2j} s_{jk} g_{2k}$. Substituting the derived expression for the spontaneous polarization into this relaxation rate gives

$$\tau_X^{-1} = 2\gamma\chi.$$

This shows that for a given ΔT the relaxation rate is twice as large for T less than T_C than for T greater than T_C which is similar to the results for the dielectric constant of a ferroelectric near T_C .

The condition that these fluctuations occur at constant stress implies that

$$x_k(q) = -2s_{kj}g_{2j}P_sP_2(q).$$

Therefore associated with the (critical) fluctuations in polarization there is a strain fluctuation. Even if the polarization fluctuations are not coupled to the optical dielectric tensor the strains are and they should give a central component to the light scattering spectrum whose width is proportional to the relaxation rate for the fluctuations. For later reference we calculate the mean square fluctuation in the strain due to these damped fluctuations. From the constant stress condition we have, taking thermal averages

$$\langle |x_k(q)|^2 \rangle = 4(s_{kj}g_{2j})^2 P_s^2 \langle |P_2(q)|^2 \rangle.$$

The mean square fluctuation in polarization is easily calculated to

be

$$\langle |P_2(q)|^2 \rangle = \frac{kT}{V} \frac{1}{2(\xi - 2g_s g) P_s^2} .$$

Therefore

$$\langle |x_k(q)|^2 \rangle = \frac{4(s_{kj} g_{2j})^2}{2(\xi - 2g_s g)} \frac{kT}{V} .$$

Later we will compare this to the mean strain for an acoustic mode

$$\langle |x|^2 \rangle = \frac{kT}{V} \frac{1}{\rho v^2} .$$

For the strain fluctuations corresponding to the acoustic modes we seek oscillating solutions of the form $\exp(-i\omega t)$ with $\omega = \omega(q)$ to be determined. We are interested in that part of the polarization fluctuations which is oscillating at the same frequency as the strain waves so that $\dot{P}_2(q) = -i\omega P_2(q)$. If we substitute this into the kinetic equation we find

$$-i \frac{\omega(q)}{V} P_2(q) = 2\xi P_s^2 P_2(q) + 2g_{2j} P_s x_j(q)$$

so that

$$\frac{\partial P_2(q)}{\partial x_j(q)} = - \frac{2g_{2j} P_s}{2\xi P_s^2 + i \frac{\omega(q)}{V}}$$

where $\omega(q)$ is the frequency of the strain wave of interest.

In order to apply the equations of motion for the strain waves that we derived in Section II we must calculate the effective elastic

constant

$$c_{jk}(q) = \frac{\partial X_j(q)}{\partial x_k(q)} .$$

From the equation relating the Fourier components of stress, strain and polarization we have

$$\frac{\partial X_j(q)}{\partial x_k(q)} = c_{jk}^P + 2g_{2j} P_s \frac{\partial P_2(q)}{\partial x_k(q)}$$

If we now substitute the expression that we derived for the derivative of P_2 with respect to strain we find that the effective elastic constant is given by

$$c_{jk}(q) = c_{jk}^P - 4 g_{2j} g_{2k} P_s^2 / 2\xi P_s^2 + \frac{i\omega(q)}{\gamma}$$

which we rewrite as

$$c_{jk}(q) = c_{jk}^P - \frac{2g_{2j}g_{2k}}{\xi} / [1 + i\omega(q)\tau]$$

with

$$\tau^{-1} = \gamma 2\xi P_s^2 .$$

$\omega(q)$ is still not determined. To complete the calculation we must solve the acoustic mode eigenvalue problem with the (complex) effective elastic constants that we have derived. This will yield an equation for $\omega(q)^2$ in terms of the complex elastic constants. Self consistent real and imaginary parts of $\omega(q)$ must be found which satisfy this equation .

The calculation as outlined is formidable. Nevertheless practical solutions are possible for TGS because the coupling is weak, that is

$$\frac{2g_{2j}g_{2k}}{\xi} \ll c_{jk}^P.$$

This allows us to write for each mode a dispersion relation of the form

$$\frac{[\omega(q)]^2}{q^2} = v_{\infty}^2 - (v_{\infty}^2 - v_0^2) / [1 + i\omega(q)\tau].$$

Here the velocities are (real) roots of acoustic eigenvalue problems and hence depend on the direction of \vec{q} . v^2 comes from the eigenvalue problem using the elastic constants c_{ij}^P and v_0^2 comes from the eigenvalue problem using the elastic constants $c_{ij}^E = c_{ij}^P - 2g_{2i}g_{2j}/\xi$.

By our previous assumption $(v_{\infty}^2 - v_0^2) \ll v_{\infty}^2$ so that the imaginary part of the complex frequency $\omega(q)$ is much smaller than the real part $\omega'(q)$ then we can write

$$v^2 = \frac{\omega'(q)^2}{q^2} = v_{\infty}^2 - (v_{\infty}^2 - v_0^2) / [1 + (\omega'(q)\tau)^2]$$

$$\omega''(q) = 1/2 (\omega_{\infty}^2 - \omega_0^2) \tau / [1 + (\omega'(q)\tau)^2]$$

Equations of this form with τ^{-1} proportional to ΔT were predicted by Landau and Khalatnikov in their treatment of the relaxation of the order parameter. ⁽⁷⁵⁾

The physics of the velocity dispersion is as follows. For

For sufficiently short wavelengths the strain fluctuations have very high frequencies. If the fluctuations in P_2 are considered to decay exponentially then for sufficiently high frequencies (or low relaxation rates) they will not be able to follow the oscillating strain fluctuations. Thus these strains will take place at constant $P_2(q)$ and so will be described by c_{jk}^P . On the other hand, for low frequencies (or fast relaxation rates) $P_2(q)$ has no difficulty in following the strain oscillations. $P_2(q)$ adjusts to keep E_2 small so that the strain fluctuations occur at constant (zero) field and are described by the constants $c_{jk}^E = c_{jk}^P - 2g_{2j}g_{2k}/\xi$. These intuitive ideas are given explicit expression in the equation of velocity dispersion.

The relaxation rate in the derived expressions of velocity dispersion is

$$\tau^{-1} = \gamma 2\xi P_s^2.$$

The derivation assumed that the polarization fluctuations were isothermal. Actually they are adiabatic. This difference is more important for the polarization fluctuation dynamics than for the strain fluctuation dynamics because temperature fluctuations are strongly coupled to the polarization through $2\xi P_s^2$. Jona and Shirane have worked out the difference between the adiabatic and isothermal inverse susceptibility in TGS.⁽⁷⁶⁾ The correction applies equally well to the relaxation rate. Above T_C the correction is negligible while below T_C the inverse susceptibility and therefore the relaxation rate for adiabatic processes is increased by 20%. We have not applied this correction in comparing theory with our results.

Comparison with Experiment

We now have enough of the theory worked out to begin comparing

it to the observations in TGS. The basic result from the velocity dispersion with temperature measurements reported in Section V is that they fit a single relaxation equation of the form derived here. Moreover the relaxation rate was proportional to $(T_C - T)$ as the theory predicts and independent of \vec{q} . The magnitude of the relaxation rate can not be calculated from the phenomenological theory here since γ is an unknown parameter. Therefore we must turn to predictions about the coupling to find additional confirmation of the theory.

From the monoclinic macroscopic symmetry of TGS we know that the matrices for c_{ij} and g_{kl} have non-zero components as indicated in the following diagram: ⁽¹⁷⁾

$$\begin{bmatrix} \bullet & \bullet & \bullet & \cdot & \bullet & \cdot \\ \bullet & \bullet & \bullet & \cdot & \bullet & \cdot \\ \bullet & \bullet & \bullet & \cdot & \bullet & \cdot \\ \cdot & \cdot & \cdot & \bullet & \cdot & \bullet \\ \bullet & \bullet & \bullet & \cdot & \bullet & \cdot \\ \cdot & \cdot & \cdot & \bullet & \cdot & \bullet \end{bmatrix}$$

In particular g_{2j} has non-zero components only for $j = 1, 2, 3$, and 5. Therefore the matrix $g_{2j}g_{2k}/\xi$ which gives the differences between the c^P and c^E stiffness constants has the following non-zero components:

$$\begin{bmatrix} \bullet & \bullet & \bullet & \cdot & \bullet & \cdot \\ \bullet & \bullet & \bullet & \cdot & \bullet & \cdot \\ \bullet & \bullet & \bullet & \cdot & \bullet & \cdot \\ \cdot & \cdot & \cdot & \cdot & \cdot & \cdot \\ \bullet & \bullet & \bullet & \cdot & \bullet & \cdot \\ \cdot & \cdot & \cdot & \cdot & \cdot & \cdot \end{bmatrix}$$

For \vec{q} in the (010) plane of TGS we showed in Section II that the pure shear mode labeled T2 involves only the constants c_{66} , c_{44} , and c_{46} . We see that these constants are not coupled to the spontaneous polarization and therefore should show no relaxation. In the experiment we found only a linear decrease with temperature in the T2 velocities and no relaxation dispersion near T_C in agreement with this prediction.

The quasi-longitudinal and quasi-transverse modes labeled L and T1 for the (010) plane involve the six constants c_{11} , c_{33} , c_{55} , c_{13} , c_{15} , and c_{35} all of which are coupled to the polarization. It is for these modes that we observed single relaxation time velocity dispersion with temperature. Using the velocity difference $(v_\infty - v_0) = (v^P - v^E)$ as a measure of the coupling of these modes to the polarization we see that the coupling can be very anisotropic since it comes from differences in velocities calculated from two sets of elastic constants each of which give an anisotropic velocity pattern having no symmetry except a center of inversion. We believe that this is the explanation of the anisotropy observed in the experiment and shown on Fig. V 7.

We do find qualitative agreement for the relationship predicted by the theory between the thermal expansion measurements⁽⁷⁸⁾ and the L mode coupling anisotropy. The calculation of the spontaneous strain with our model free energy showed that

$$(x_k)_0 = -s_{jk} g_{2j} P_s^2.$$

Thus if a particular component of g_{2j} is large then the pattern of expansion might be expected to show a maximum in the j direction.

Light scattering and ultrasonics agree that s_{33} is large (L mode velocity is minimum near c). The thermal expansion is observed to be large and positive near the c direction. Therefore it seems that g_{23} is large and negative. If this is true then we expect that c_{33} will show a large positive dispersion with temperature. This agrees with our observations of maximum total dispersion for the L mode near the \hat{c} direction.

We have made an attempt to make a quantitative comparison of the observed anisotropy and measured properties of TGS. Schmidt and Pfannschmidt⁽⁷⁹⁾ and Ikeda et al.⁽⁸⁰⁾ have reported measurements of the strain electrostriction constants Q_{2j} . These measurements agree within their precision of $\pm 10\%$ except for Q_{25} for which Schmidt and Pfannschmidt argue for their smaller value. These measurements are reported in the $x'y'z' = abc^*axc^*$. We compute them for the rotated axes $-a^*-bc$. We want the stress constants g_{2j} which we can compute from the equation

$$-g_{2j} = c_{jk}^P Q_{2k}.$$

Using the elastic stiffness constants of Konstantinova et al. listed in the appendix which are the constants c_{ij}^E (subject to correction because they did not give agreement with the velocities that we observed) as approximately equal to the constants c_{ij}^P we found

$$-g_{2j} = [2.7 \quad 1.7 \quad -1.9 \quad 0 \quad -2.0 \quad 0] \pm 10\% \text{ (dimensionless)}$$

Using these and $\xi = (6.9 \pm 10\%) \times 10^{-10} \text{ cm}^2/\text{dyne}$ we calculated that $c_{ij}^P - c_{ij}^E = 2g_{2i}g_{2j}/\xi$ was

$$\begin{bmatrix}
 21. & 13. & -15. & . & -16. & . \\
 13. & 8.4 & -9.3 & . & -10. & . \\
 -15. & -9.3 & 11. & . & 11. & . \\
 . & . & . & . & . & . \\
 -16. & -10. & 11. & . & 14. & . \\
 . & . & . & . & . & .
 \end{bmatrix} \pm 30\% \times 10^9 \text{ dynes/cm}^2$$

With this matrix we calculated c_{ij}^P from Konstantinova's c_{ij}^E . Using these c^P we calculated the velocities as a function of \hat{q} in the (010) plane. The results are given in Fig. VI 1 in the form of a plot of $(v^P - v^E)$ versus $\Theta(q)$, the angle between \hat{q} and \vec{c} . Comparing this plot with Fig. V 7 we see that the agreement in magnitude and pattern is poor.

An improved calculation of the coupling anisotropy could be done using c_{ij}^P determined from the light scattering velocity measurements. These elastic constants should be better because they are determined from more detailed velocity measurements and because they are determined at T_C where we wish to test the theory.

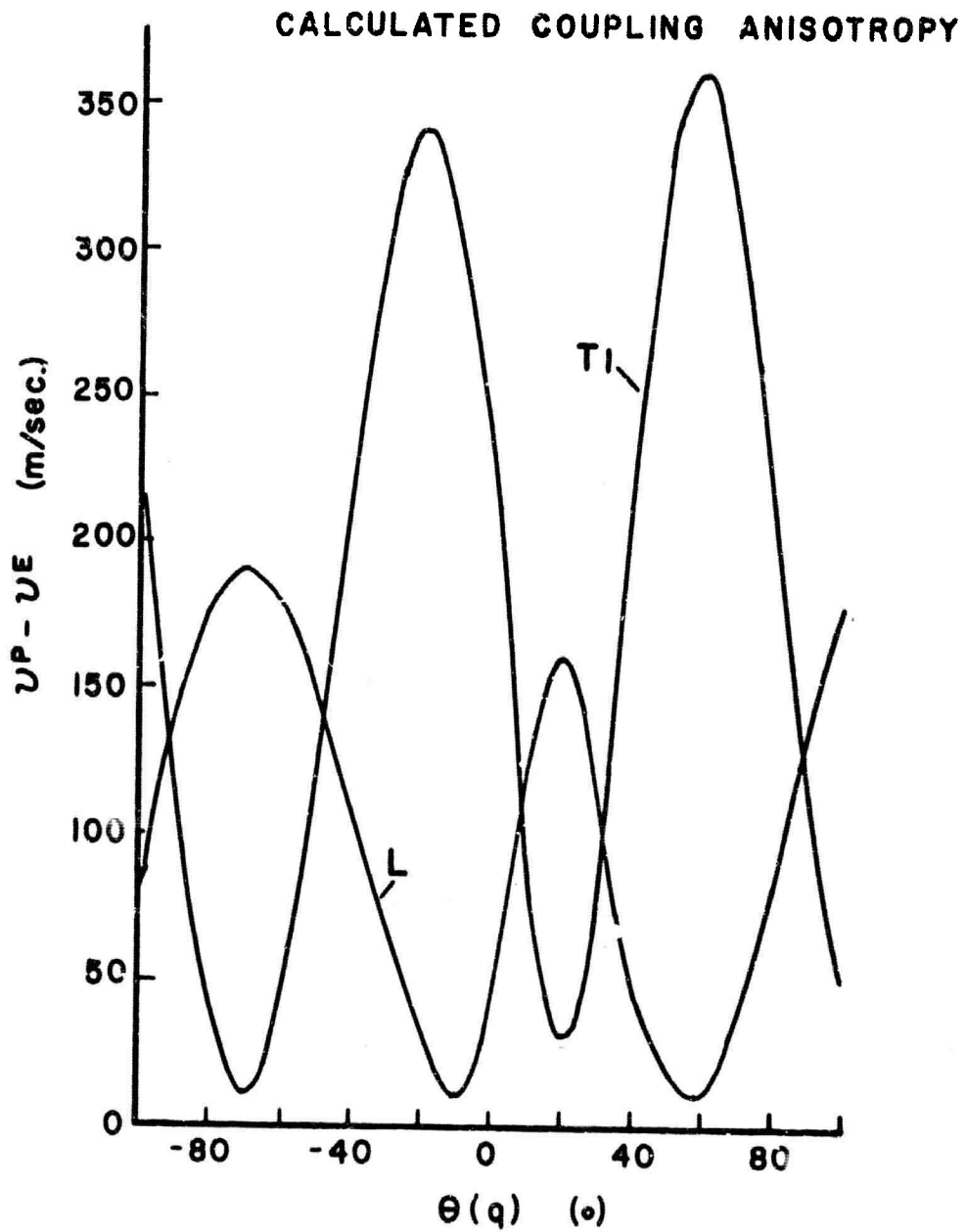


Fig. IV 1 Calculated coupling anisotropy, $v^P - v^E = v_{\infty} - v_0$
for L and T1 modes, (010) plane.

Opalescence Below T_C

Earlier we showed that part of the strain fluctuation followed the polarization fluctuations and were exponentially decaying. With the electrostriction constants used above we can now evaluate the mean square strain due to this mode and compare it to the mean square strain in an acoustical mode. The result of this calculation is that the damped strain fluctuations should scatter about 1% as much light as a typical longitudinal mode. This amount of scattering in the central component is completely negligible compared to the extraneous elastic scattering in the crystal and so was not detectable.

Kinetic Coefficient Evaluation

Accepting the theory as confirmed by the comparisons with experiment presented so far we can relate the measured relaxation rate to the known spontaneous polarization and the unknown kinetic coefficient and thus extract a value for the kinetic coefficient.

From the dielectric properties listed in the Appendix we have $2\xi P_s^2 = 8.3 \times 10^{-3} (T_C - T)$ (dimensionless). The measured relaxation rate was $(\tau)^{-1} = (3.4 \pm 10\%) \times 10^{10} (T_C - T) \text{ sec.}^{-1}$. The theory gives the relaxation rate below T_C as $(\tau)^{-1} = \gamma 2\xi P_s^2$. Therefore $\gamma = (4.1 \pm 10\%) \times 10^{12} \text{ sec.}^{-1}$. This is a reasonable value for the

kinetic coefficient because the maximum relaxation rate for very short wavelength components of the polarization fluctuations is $4\pi\gamma = 52. \times 10^{12} \text{ sec.}^{-1}$. This is comparable to typical lattice vibration frequencies in molecular crystals as it must be since the vibration frequencies ultimately determine how fast microscopic changes can take place in the structure.

Field Dependent Relaxation Rates

We return to the development of the theory now to show how it yields predictions of a field dependent relaxation rate.

We treat the case of an applied dc field parallel to the ferroelectric axis and zero stress at T_C . For this case our model thermodynamic potential gives the equilibrium conditions

$$X_j + c_{jk}^P x_k + g_{2j} P_2^2 = 0$$

$$E = \xi P_2^3 + 2g_{2j} x_j P_2.$$

We solve these for the induced strain and polarization. We find

$$(x_k)_e = -s_{kj} g_{2j} P_e^2$$

$$P_e^3 = \frac{E}{(\xi - 2gsg)}.$$

Expressed in terms of Fourier components the fluctuations about the equilibrium values of the thermodynamic variables satisfy the linearized equations

$$X_j(q) = c_{jk}^P x_k(q) + 2g_{2j} P_e P_2(q)$$

$$E_2(q) = 2g_{2k} P_e x_k(q) + (3\xi - 2gsg) P_e^2 P_2(q)$$

We again assume that

$$\dot{P}_2(q) = -\gamma \frac{\partial A}{\partial P_2} = -\gamma E_2(q)$$

and that the kinetic coefficient is the same as in the zero field case.

To study the strain dynamics we look for solutions of the form $\exp(-i\omega t)$ in all fluctuations. This gives

$$\frac{\partial P_2(q)}{\partial x_k(q)} = - \frac{2g_{2k} P_e}{(3\xi - 2gsg) P_e^2 + \frac{i\omega(q)}{\gamma}}$$

so that the effective elastic constant is given by

$$c_{jk}(q) = \frac{\partial X_j(q)}{\partial x_k(q)} = c_{jk}^P - \frac{4g_{2j}g_{2k}}{(3\xi - 2gsg)} [1 + i\omega(q)\tau]$$

with

$$\tau^{-1} = \gamma (3\xi - 2gsg) P_e^2.$$

We rewrite τ^{-1} by substituting the value of induced field that we derived and find

$$\tau^{-1} = \gamma \frac{(3\xi - 2gsg)}{(\xi - 2gsg)^{2/3}} E^{2/3}.$$

The structure and solutions of these equations are quite similar to those for the temperature dependent relaxation. Since the coupling

matrix is essentially the same and has exactly the same symmetry we expect to see the Brillouin components which showed temperature dependent relaxation to show a relaxational dispersion with field with a relaxation time proportional to $E^{2/3}$.

In the experiments with TGS this is exactly what was observed. We were even able to get reasonable agreement between the observed relaxation rate and the calculated rate based on the dielectric parameters and the kinetic coefficient determined in the temperature experiments.

Using the g_{2j} components discussed earlier and s_{ij} calculated by Ballato⁽⁸⁾ from the measurements of c_{ij} by Konstantinova et al. we find that $gsg = g_{2j}s_{jk}g_{2k} = (2.3 \pm 20\%) \times 10^{-10} \text{ cm}^2/\text{dyne}$. Taking $\xi = (6.9 \pm 10\%) \times 10^{-10} \text{ cm}^2/\text{dyne}$, and converting from stat volts/cm to kV/cm we predict $\tau^{-1} = (4.1 \pm 50\%) \times 10^{10} (E \text{ kV/cm})^{2/3} \text{ sec.}^{-1}$. We observed that the relaxation rate was $(2.0 \pm 10\%) \times 10^{10} E^{2/3} (\text{kV/cm})^{2/3}$. The agreement is satisfactory because the term $(\xi - 2gsg)$ which appears in the denominator in the calculated rate almost shows a cancellation whereas the temperature dependence study shows that the g_{2j} are probably smaller than those used in the calculation. This causes the calculated rate to be high. Also experimentally if the applied field across the sample electrodes does not all go into inducing polarization of the crystal then the measured rate would appear to be smaller for a given field.

Using the theory we can also calculate that the matrix giving the total change in elastic constants for the field effect is 16% smaller than that for the temperature effect, since $4/(3\xi - 2gsg)$ is calculated

to be 16% smaller than $2/\xi$. In the experiment we observed that the coupling in terms of elastic constants was 25% less than for the temperature effect.

\vec{q} Parallel to the Ferroelectric Axis

So far the theory seems well confirmed. But we notice that our calculation explicitly shows that c_{22} is coupled to the polarization. Therefore we would predict that the longitudinal mode with \vec{q} parallel to \vec{b} should show a 3% change in v^2 as T approaches T_C . The experiment does not agree. We saw no temperature dependent relaxation for \vec{q} parallel to \vec{b} . This observation shows that we have left something out of our treatment.

The difficulty arises because we have ignored the electrostatic energy associated with a Fourier component of the polarization fluctuation. We find that we must modify the model free energy in order to satisfy Maxwell's equations. The problem is quite analogous to the lattice dynamics problem in ionic lattices in which the electrostatic energy lifts the degeneracy of the longitudinal and transverse optical modes by increasing the frequency of the longitudinal mode. ⁽⁸²⁾

TGS is an insulator so we must satisfy the equation

$$\vec{\nabla} \cdot \vec{D} = \vec{\nabla} \cdot (\vec{E} + 4\pi \vec{P}) = \vec{q} \cdot (\vec{E}(q) + 4\pi \vec{P}(q)) = 0$$

Moreover the mode frequencies are small compared with the frequencies of photons having the same q (IR radiation) hence $\vec{B}(q)$ is small. Therefore

$$\vec{\nabla} \times \vec{E}(q) \approx 0$$

The polarization is essentially along the ferroelectric (b) axis.

The curl equation shows that $E(q)$ is longitudinal, that is parallel to \vec{q} . All together this shows that the field component parallel to the b axis associated with $P_2(q)$ is

$$E_2'(q) = -4\pi P_2(q) m^2$$

with m the cosine of the angle between \vec{q} and the b axis. This field is a vacuum field. The thermodynamic calculation gives the local field. The total "force" on $P_2(2)$ is the difference between the local field and the vacuum field

$$E_2(q) = \frac{\partial A(q)}{\partial P_2(q)} - E_2'(q) .$$

The effect of this modification is the same as if new terms of the form

$$(1/2)4\pi m^2 P_2(q)^2$$

were added to the fluctuation in the free energy. Then we must repeat our derivation of the strain fluctuation dynamics using the modified equation

$$E_2(q) = 2 g_{2j} P_s x_j(q) + (4\pi m^2 + 2\xi P_s^2) P_2(q) .$$

Near T_C $4\pi m^2$ is greater than $2\xi P_s^2$ since $2\xi P_s^2$ approaches zero.

The kinetic assumption now gives

$$\frac{\partial P_2(q)}{\partial x_j(q)} = -2 g_{2j} P_s / (4\pi m^2 + 2\xi P_s^2 + 1 \frac{\omega}{\gamma})$$

so that the effective elastic constants are

$$c_{jk}^{(q)} = \frac{\partial X_j(q)}{\partial x_k(q)} = c_{jk}^P - \frac{4 g_{2j} g_{2k} P_s^2}{(4\pi m^2 + 2\xi P_s^2)} \frac{1}{(1 + i \omega(q) \tau)}$$

with

$$\tau^{-1} = \gamma (4\pi m^2 + 2\xi P_s^2)$$

If $4\pi m^2$ is small compared with $\omega(q)$ then we recover the dispersion previously derived without considering electrostatics. In the present experiment this limit would require m less than $\pm .03$ or the \hat{q} direction within $\pm 15^\circ$ of the (010) plane. This was satisfied during the (010) plane experiment.

For \hat{q} parallel to \vec{b} we have $m^2 = 1$. In this case we rewrite the expression for the elastic constant as follows:

$$c_{jk}(\vec{q} \parallel \vec{b}) = c_{jk}^P - \frac{2 g_{2j} g_{2k}}{\xi} \frac{\xi P_s^2 / \pi}{(1 + \xi P_s^2 / 2\pi)} \frac{1}{(1 + i \omega(q) \tau)}$$

with

$$\tau^{-1} = 4\pi\gamma \left(1 + \frac{\xi P_s^2}{2\pi}\right)$$

Now we see that at low frequencies which includes all light scattering frequencies in TGS, $(c_{jk}^p - c_{jk})$ is temperature dependent going continuously to zero as T goes to T_C from below. The relaxation rate is much faster and is essentially temperature independent near T_C .

We have written the equation in a form which allows easy comparison with the equations of the elastic constants for \vec{q} in the (010) plane. We see that the leading term of the amplitude of the dispersion is the same namely $2g_{2j}g_{2k}/\xi$. But in TGS the extra factor

$$\frac{(\xi P_s^2/\pi)}{(1 + \xi P_s^2/2\pi)} \approx (\xi P_s^2/\pi)$$

is much less than 1 for all T between room temperature and T_C . Thus the change in velocity for the longitudinal mode propagating down the b axis was too small to be seen in our experiment. Notice that even if the change in velocity had been detectable in this case, it would not have involved q dependent relaxation and would not have given broadening of the Brillouin component.

The anisotropic relaxation rate that we have derived implies that there are directions of \vec{q} between \vec{b} and the (010) plane for which particular acoustic modes would show large, temperature independent acoustic single relaxation time absorption. This would be interesting to actually observe as a check on the theory since in the case of \vec{q} parallel to \vec{b} we used the theory in a negative way by explaining why temperature dispersion was not seen. With T at T_C , the relaxation times found in scanning the direction of \vec{q} between \vec{b} and the (010) plane could be used to determine a value of γ independent of dielectric measurements.

Conclusions

We conclude from the agreement between the theory presented in this section and the observations presented in Section V that combining the Landau-Khalatnikov picture of the polarization fluctuation dynamics with the Devonshire free energy expansion applied to inhomogenous fluctuations yields a good description of the behavior of TGS in the region of the phase transition.

APPENDIXProperties of TGSChemical

Formula ⁽³¹⁾	$(\text{NH}_2\text{CH}_2\text{COOH})_3\text{H}_2\text{SO}_4$
Formula weight	323 gm/mole
Density ⁽³¹⁾	1.69 gm/cc

Crystallography

Symmetry above T_C	(average) ⁽⁴¹⁾
	space group $P2_1/m$
	(point group $2/m$)

Symmetry below T_C	⁽⁴¹⁾
	space group $P2_1$
	(point group 2)

Lattice constants⁽³¹⁾

$$a_o = 9.15, b_o = 12.69, c_o = 5.73 \pm 0.03 \text{ \AA}$$

$$\beta = 105^\circ 40' \pm 20'$$

Coordinate Systems

Coordinate systems and reference directions used in this work are shown in Fig. A 1. \vec{a}^* and \vec{c}^* refer to reciprocal lattice directions. The choice of \vec{a} and \vec{c} is that of Wood and Holden. The direction of $\vec{b} = \vec{b}^*$ taken to give right handed triads of directions in the direct and reciprocal lattices.

The most convenient right handed, orthogonal coordinate system for this work is that of $x' y' z' = abc^*$. Another natural choice of right handed orthogonal coordinates would be $x'' y'' z'' = a^* bc$. This set of axes would be rotated by $15^\circ 40'$ about \vec{b} from the $x' y' z'$ axes. Instead of this choice the ultrasonic study of the elastic constants⁽⁸⁵⁾ was done in terms of the $xyz = -a^* -b c$ right handed, orthogonal coordinates obtained by a rotation about \vec{b} of 195° . When comparing our results to the ultrasonic velocity measurements we will use the xyz coordinates.

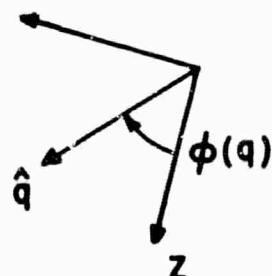
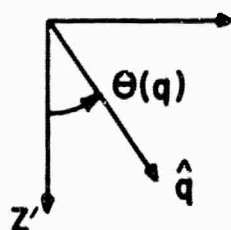
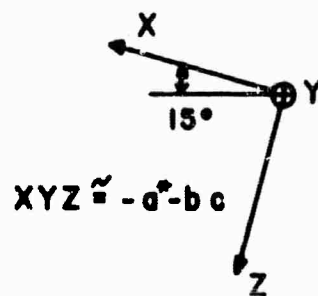
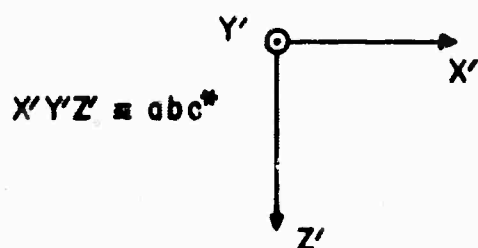
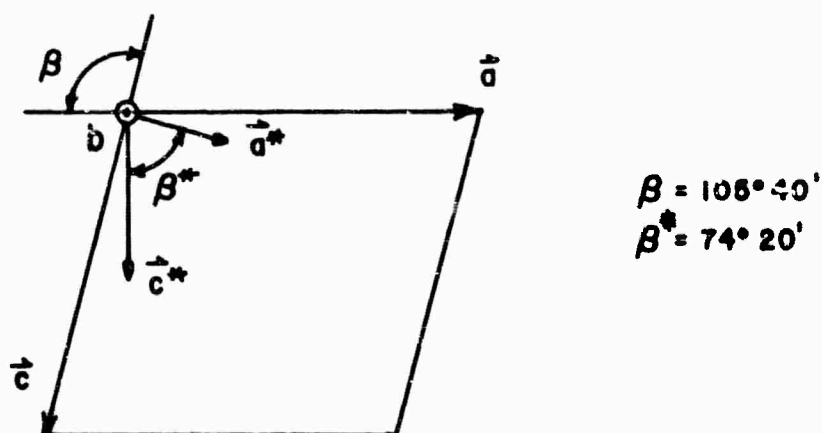
Directions are labeled in the (010) plane by the angles between them and either the \vec{c} or \vec{c}^* directions. The sense of these angles is important and is indicated in the figure.

Optical Parameters

The b axis coincides with the acute bisectrix (lowest index of refraction). The other two principle axes of the optical dielectric ellipsoid lie in the (010) plane. The obtuse bisectrix (highest index) is 3° from the c axis in the (010) plane. The optic normal axis (intermediate index) is perpendicular to the first named axes.

Fig. A 1

TGS
LATTICE DIRECTIONS AND COORDINATE
SYSTEMS



The refractive indices (room temperature and Na D light) are

$$n_p = 1.484$$

$$n_m = 1.556$$

$$n_g = 1.584$$

The optic angle is

$$(-) 2V = 61^{\circ} 18' 18'' \pm 1^{\circ} 5'$$

Dielectric (48)

$$\epsilon_b = C^{\pm} / |T - T_C|$$

$$T > T_C, \quad C^+ = 3560 \text{ C}^{\circ}$$

$$\frac{C^+}{C^-} = 2.42$$

$$\xi = (6.9 \pm .7) \times 10^{-10} \text{ cm}^4 / (\text{stat. coul})^2 \text{ or cm}^2 / \text{dyne}$$

$$\text{From } 2\xi P_s^2 \approx 4\pi / \epsilon_b, \quad 2\xi P_s^2 = 8.3 \times 10^{-3} (T_C - T) \text{ dimensionless}$$

Elastic Constants

Matrix notation. xyz coordinates of Fig. A 1.

c_{ij} (Konstantinova et al., reference (85):

$$\begin{bmatrix} 4.55 & 1.72 & 1.98 & . & -.30 & . \\ 1.72 & 3.21 & 2.08 & . & -.036 & . \\ 1.98 & 2.08 & 2.63 & . & -.5 & . \\ . & . & . & .95 & . & -.026 \\ -.30 & -.036 & -.5 & . & 1.11 & . \\ . & . & . & -.026 & . & .62 \end{bmatrix} \times 10^{11} \text{ dynes/cm}^2$$

s_{jk} , the inverse matrix to c_{ij} computed by Ballato: (81)

$$\begin{bmatrix} 32.9 & -2.9 & -22.7 & . & -1.5 & . \\ -2.9 & 69.8 & -57.7 & . & -24.5 & . \\ -22.7 & -57.7 & 108.5 & . & 40.9 & . \\ . & . & . & 105.4 & . & 4.4 \\ -1.5 & -24.5 & 40.9 & . & 107.3 & . \\ . & . & . & 4.4 & . & 161.5 \end{bmatrix} \times 10^{-13} \text{ cm}^2/\text{dyne}$$

Electrostriction

Strain electrostriction constants in $x'y'z'$ coordinates measured by Schmidt and Pfannschmidt⁽⁷⁹⁾ :

$$Q_{2j'} = [1.8 \quad 2.7 \quad -5.0 \quad . \quad 0.1 \quad .] \pm 10\% \times 10^{-11} \text{ cm}^2/\text{dyne}$$

Strain electrostriction in xyz coordinates of Fig. A 1 :

$$Q_{2j} = [1.3 \quad 2.7 \quad -4.5 \quad . \quad -3.4 \quad .] \times 10^{-11} \text{ cm}^2/\text{dyne}$$

Using c_{ij} of Konstantinov et al. the electrostriction stress constants are calculated from $-g_{2j} = c_{jk} Q_{2k}$ to be:

$$-g_{2j} = [2.7 \quad 1.7 \quad -1.9 \quad . \quad -2.0 \quad .] \quad \text{dimensionless}$$

Thermal Expansion⁽⁵⁷⁾

At 50° C

$$\alpha_{100} = 38 \text{ ppm/C}$$

$$\alpha_{001} = 14.5 \text{ "}$$

$$\alpha_{101} = 1.4 \text{ "}$$

$$\alpha_{010} = 64 \text{ "}$$

Heat Capacity⁽⁶⁹⁾

$C_P = .35 \text{ to } .36 \text{ cal/g C}^\circ$ from room temperature through T_C .

C_E shows a maximum below T_C . Highest measured value was $.48 \text{ cal/g C}^\circ$.

FOOTNOTES

1. P. Debye and F.W. Sears, Proc. Nat. Acad. Sci., Wash., 18, 409 (1932). See M. Born and E. Wolf, Principles of Optics (Pergamon New York, 1959), Chap. XII.
2. L. Brillouin, Ann. Phys. (Paris) 17, 88 (1922).
3. A. Einstein, Ann. Physik 33, 1275 (191
4. M. Leontovich and S. Mandel'shtam, Phys. Zeit. Sowjet 1, 317 (1931); Z. Physik 75, 350 (1932).
5. S. Bhagavantam, Scattering of Light and the Raman Effect, (Chemical Publishing Co., Brooklyn, 1942).
6. C.I. Carr and B.H. Zimm, J. Chem. Phys. 18, 1616 (1950).
7. I.L. Fabelinski, Sov. Phys. Uspeki 5, 667 (1963).
8. R. Pecora, J. Chem. Phys. 40, 1604 (1964).
9. L.D. Landau and E.M. Lifshitz, Electrodynamics of Continuous Media, (Pergamon, New York, 1958).
10. A.B. Bhatia and K.S. Krishnan, Proc. Roy. Soc. (London) A192, 181 (1948), Sec. 7; M. Lax, Rev. Mod. Phys. 23, 287 (1951), Sec. H.
11. L.D. Landau and E.M. Lifshitz, Statistical Physics, (Pergamon, New York, 1958) Sec. 116.
12. K. Vedam and E. Schmidt, Phys. Rev. 146, 548 (1966).
13. M. Born and K. Huang, Dynamical Theory of Crystal Lattices, (Oxford: Clarendon Press, 1954), p. 379, equation (50.26).

14. L. D. Landau and E. M. Lifshitz, Theory of Elasticity, (Pergamon, New York, 1959).
15. J. F. Nye, Physical Properties of Crystals, (Oxford: Clarendon Press, 1957) p. 113 and p. 134.
16. Reference (15). A summary of the effect of symmetry on tensor properties is also given on pp. (9-15) - (9-20) of reference (17).
17. American Institute of Physics Handbook, (McGraw-Hill Book Co., Inc., 1963), p. (3-82).
18. R. F. S. Hearmon, Adv. in Phys. 5, 323 (1956).
19. This problem has recently been discussed in detail for cubic crystals by G. B. Benedek and K. Fritsch, Phys. Rev. 149, 647 (1966). Extensive calculations of scattering intensity in birefringent crystals were performed by Chandrasekharan: V. Chandrasekharan, Proc. Indian Acad. Sci. 33A, 183 (1951); Proc. Nat. Inst. Sci. (India) 19, 547 (1953).
20. V. Chandrasekharan, reference (19).
21. Nye, reference (15), Sec. 2.6.
22. Nye, " " Table 17, p. 255.
23. Landolt-Bornstein, Group III, Vol. 1, Elastic, Piezoelectric, Piezooptic and Electrooptic Constants of Crystals, (Springer-Verlag New York, 1966).
24. Landau and Lifshitz, reference (11).

25. R. Y. Chiao and B. P. Stoicheff, J. Opt. Soc. Am. 54, 1286 (1964).
26. H. Z. Cummins and R. W. Gammon, J. of Chem. Phys. 44, 2785 (1966).
27. M. Born and E. Wolf, Principles of Optics, (pergamon, New York, 1959), p. 328.
28. P. Jacquinet, Rept. Prog. Phys. 23, 267 (1960).
29. S. M. Shapiro, R. W. Gammon and H. Z. Cummins, Appl. Phys. Letters 9, 157 (1966) .
30. F. Jona and G. Shirane, Ferroelectric Crystals, (Pergamon, New York, 1962), Chap. II.
31. E. A. Wood and A. N. Holden, Acta Cryst. 10, 145 (1957).
32. I. M. Dion Acta Cryst. 12, 259 (1959).
33. The index of the oil was measured with a Abbe' refractometer and found to be typically 1.48 with temperature coefficient of $-.04\%/C^{\circ}$.
34. H. Mueller, Proc. Roy. Soc. (London) A166, 425 (1938).
35. K. Vedam, Phys. Rev. 78, 472 (1950).
36. W. Primak and D. Post, J. Appl. Phys. 30, 779 (1959).
37. J. L. Torgeson, A. T. Horton and C. P. Saylor, J. Res. Natl. Bur. Std. (U.S.) 67C, 25 (1963).

38. R. Nitsche, *Helv. Phys. Acta* 31, 306 (1958); M. F. Koldobskaya and I. V. Garvriлова in Growth of Crystals, Vol. 3, Shubnikov and Sheftal, ed. translation (Consultants Bureau, New York, 1963).
39. B. T. Matthias, C. E. Miller and J. P. Remeika, *Phys. Rev.* 104, 849 (1956).
40. Wood and Holden, reference (31).
41. Hoshino, Okaya and Pepinsky, *Phys. Rev.* 115, 323 (1959).
42. Jona and Shirane, reference (30), p. 30.
43. Hoshino et al., reference(41).
44. J. Gilletta, *Compt. Rend.* 253, 1556 (1961).
45. T. Ikeda, Y. Tanaka and H. Toyoda, *Japan. J. Appl. Phys.* 1, 13 (1962).
46. E. J. O'Brian and T. A. Litovitz, *J. Appl Phys.* 35, 180 (1964).
47. P. P. Craig, *Phys. Letters* 20, 140 (1966).
48. J. A. Gonzalo, *Phys. Rev.* 144, 662 (1966).
49. C. B. Sawyer and C. H. Tower, *Phys. Rev.* 35, 269 (1930).
50. J. Stankowska and J. Stankowski, *Acta Phys. Polon.* 19, 217 (1960).
51. Jona and Shirane, reference (30). pp. 47-50.

52. R. W. Gammon and H. Z. Cummins, Phys. Rev. Letters 17, 193 (1966).
53. The T1 mode linewidths were determined with a 5 mm etalon instead of the 3 mm etalon used in the other parts of the work.
54. Reviews of dispersion relations in treating sound propagation can be found in: K. F. Hertzfeld and T. A. Litovitz, Absorption and Dispersion of Ultrasonic Waves, (Academic Press, New York, 1959); J. J. Markam, R. T. Beyer, and R. B. L. Lindsay, Rev. Mod. Phys. 23, 353 (1951).
55. S. M. Shapiro, R. W. Gammon and H. Z. Cummins, Appl. Phys. Letters, (to be published).
56. The effect of electric fields on the elastic compliances has been studied using resonance techniques. See for example, L. A. Shuvalov and K. A. Pluzhnikov, Soviet Phys. - Cryst. 6, 555 (1962).
57. Z. I. Ezhkova, G. S. Zhdanov and M. M. Umanskii, Soviet Phys. - Cryst. 4, 229 (1960).
58. Gilletta, reference (44) and Ikeda et al., reference (45).
59. O'Brian and Litovitz, reference (46).
60. V. L. Ginzburg, Soviet Phys. - Uspeki 5, 649 (1963).
61. Craig, reference (47).
62. Gonzalo, reference (48).

63. Jona and Shirane, reference (30).
64. L. D. Landau, Phys. Z. Sowjet 11, 26 (1937); 11, 545 (1937).
65. O'Brian and Litovitz, reference (46).
66. L. D. Landau and I. M. Khalatnikov, Dokl. Akad. Nauk SSSR 96, 469 (1954). Available in English in The Johns Hopkins University-Applied Physics Laboratory Library Bulletin (Translation Series), Document No. TG 230-T83.
67. A. F. Devonshire, Phil Mag., Suppl. 3, 85 (1954).
68. Z. I. Ezhkova, et al., reference (57).
69. B. A. Strukov, Soviet Phys. 6, 2278 (1965).
70. We will use the Einstein summation convention of summing repeated indices and omit writing the summation signs throughout this section.
71. Landau and Khalatnikov, reference (66).
72. V. L. Ginzberg, UFN 38, 490 (1949); JETP 19, 36 (1949). See also the review by Ginzberg in Soviet Phys. - Uspeki 5, 649 (1963).
73. W. Cochran, Phys. Rev. Letters 3, 412 (1959); Adv. in Phys. 9, 387 (1960); Adv. in Phys. 10, 401 (1961).
74. R. A. Cowley, Phys. Rev. Letters 9, 159 (1962); Phys. Rev. 134, A981 (1964).

75. Landau and Khalatnikov, reference (66).
76. Jona and Shirane, reference (30), p. 38.
77. Nye, reference (15).
78. Z. I. Ezhkova, et al., reference (57).
79. G. Schmidt and P. Pfannschmidt, Phys. Stat. Sol. 3, 2215 (1963).
80. T. Ikeda, et al., reference (45).
81. A. D. Ballato, Acta Cryst. 14, 78 (1961).
82. Born and Huang, reference (13), Section 7. See also H. Frohlich, Theory of Dielectrics, (Oxford: Clarendon Press, 1949), Section 18 where this problem in ionic lattices is discussed in simple terms.
83. S. Hoshino, T. Mitsui, F. Jona, and R. Pepinsky, Phys. Rev. 107, 1255 (1957).
84. S. Triebwasser, IBM J. Res. 2, 212 (1958).
85. V. P. Konstantinova, I. M. Sil'vestrova and K. S. Aleksandrov, Soviet Phys. - Cryst. 4, 63 (1960).
86. L. A. Shuvalov and K. A. Pluzhnikov, Soviet Phys. - Cryst. 6, 555 (1962).
87. I. M. Sil'vestrova, Soviet Phys. - Cryst. 4, 466 (1962).
88. R. M. Hill and S. K. Ichiki, Phys. Rev. 128, 1140 (1962).